Characterizing the Pyroelectric Effects in Macro-fiber Composites

by

Krystal L. Acosta

A dissertation submitted in partial fulfillment
of the requirements for the degree of
Doctor of Philosophy
(Aerospace Engineering)
in the University of Michigan
2020

Doctoral Committee:

Professor Daniel J. Inman, Chair
Professor Veera Sundararaghavan
Assistant Professor Serife Tol
Dr. William Keats Wilkie, NASA Langley Research Center

Krystal L. Acosta
klacosta@umich.edu
ORCID iD: 0000-0002-1508-1777

This thesis is dedicated to my family who have encouraged and supported me in my academic journey.

ACKNOWLEDGEMENTS

I would like to sincerely thank the multitude of people who have encouraged and helped me to get to this point in my life. This dissertation would not have been possible without many of them. First, I would like to thank my adviser, Dr. Daniel Inman, for his continued support throughout my time at the University of Michigan. He took the time to make sure I was doing well not only in my studies but also in my personal life. I cannot express how much his style of advising has helped me come out of my shell and grow as a person. I am grateful for all the words of wisdom, advice, crazy stories, and happy memories I have made because of him. I would also like to thank my committee members, Dr. Serife Tol and Dr. Veera Sundararaghavan, for their guidance, expertise, and time.

I want to thank everyone at NASA Langley for their support and hospitality over the summers while working on my dissertation. Special thanks to Dr. Keats Wilkie, who was my mentor during my stay and is also on my committee. Many of the experiments conducted in this dissertation would have never seen the light without him and his guidance. I also need to thank Dr. Jay Warren, who helped me extensively with making sure I have everything I need for my experiments and helped me understand the results. I would also like to thank Wayne Matthews for helping me with all my electronic needs and Nigel Schneider for befriending me and brainstorming with me on the possible causes of weird results. I also have much appreciation for Joel Alexa, Harold Claytor, Stewart Walker, Peter Messick, Dr. Robert Bryant, and Dr. Sankara Sankaran for their help in setting up all the equipment and advice in both life and work. I also owe thanks to Dr. Olive Stohlman, Gregory Dean, Martin Annett, Matthew Chamberlain, and all the interns I met in the years I visited for their company and many stories.

I am also eternally grateful for all the friends both here and far that have supported me throughout my journey. They have been a massive help in keeping me sane. Specifically, I want to thank my lab mates Dr. Jared Hobeck, Dr. Alexander Pankonien, Dr. Eun Jung Chae, Dr. Katie Reichl, Dr. Wei Huang, Dr. Lawren Gamble, Dr. Andrew Lee, Dr. Brittany Essink, Lori Groo, Christina Harvey, Kevin Vaughn, and Piper Sigrest who have always been supportive, put a smile on my face, and are the best lab mates anyone can ask for. They have helped me not only in my research but with life advice as well. I am very thankful to have met them. I am immensely thankful to my boyfriend, Siddhartha Srivastava, for helping me prepare for prelims, pushing me to be a better person, and being there for me when I needed it. Thank you for putting up with me now and in the future. I also would like to thank all my friends that I have made along the way. A non-exhaustive list includes Gino Parra, Tony Parra, Monique Shotande, Lisa Worley, Christopher Pijuan, Megan Tienjaroonkul, Lance Petalio, Ishani Jetty, Roysi Bello, Nicole Casanas, Amy Gaitan, Huan Nguyen, Russell Crowe, Matthew Mayes, Mark Barbet, Manuel Angerhofer, Jacob Shapiro, Dr. Adrian Diaz, Joseph Roberts, Ana Vazquez, Dr. Fabian Chacon, Dr. Abhinav Sharma, Nicholas Arnold-Medabalimi, Dr. Samuel Chen, Louis Edelman, Dr. Jacob France, Iris Vipperman, Aaditya Lakshmanan, Shadrach Hepner, Christopher Wentland, Yukiko Shimizu, Iman Javaheri, Yifan Bai, Dr. Daning Huang, Dr. Puneet Singh, Ryan Patterson, and anyone else I may have missed. Thank you for making my schooling experience in high school, undergraduate, and graduate filled with wonderful memories that I will cherish into the ages.

To my parents, thank you for everything that you've done for me. For calming me down to telling me about your day, I love you and would not be here without your support. To my grandparents, thank you for your advice and love, for spoiling me and making sure I'm happy. To my aunts, Tia Maya and Tia Marlene, thank you for always checking up on me and wanting to spend time with me. To Aunt Marlene and Uncle Don, thank you for always asking about me and keeping me in your thoughts. Special thanks go to my cousins, Daniel Martinez, a Michigan alum, for encouraging me to come here, Krono Lescano for being supportive in my times of doubt, and Jorge Ernesto Omar for always asking about me. I would also like to thank my family

cats, Chomper and Saber. They brought me joy and comfort throughout my childhood.

Lastly, I'd like to thank the University of Michigan and NASA for funding this research. This material is based upon work supported by NASA under grant number NNX16AT21H issued through the NASA Education Minority University Research Education Project (MUREP) through the NASA Harriett G. Jenkins Graduate Fellowship activity. This work was also partially funded by the Michigan Space Grant Consortium, NASA grant number NNX15AJ20H.

TABLE OF CONTENTS

LIST OF FIGURES

LIST OF TABLES

LIST OF APPENDICES

LIST OF ABBREVIATIONS

AFC Active Fiber Composite

CTE coefficient of thermal expansion

DAQ data acquisition device

DFT Density Functional Theory

EMI electromagnetic interference

FFT fast fourier transform

FOM figure of merit

PID Proportional Integral Derivative

PZT lead zirconate titanate

MFC Macro-Fiber Composite

NASA National Aeronautics and Space Administration

NO normally open

NC normally closed

RMSD root mean square deviation

RPM rotations per minute

RTD resistive temperature device

SMA shape memory alloy

SHM structural health monitoring

TSC thermally stimulated currents

ABSTRACT

Pyroelectricity occurs in polar materials, which causes an electric potential to be generated when there is a temporal temperature change. This dissertation seeks to investigate this pyroelectric effect in Macro-fiber Composites (MFC)s, a composite material that has mainly been utilized in piezoelectric applications. The pyroelectric coefficient is a parameter for measuring the efficiency of the pyroelectric effect within a material. It has contributions from the piezoelectric effect due to the coefficient of thermal expansion (CTE), any temperature gradients within the material, and any applied external electric field. It is useful in infrared detection and energy harvesting using waste thermal energy.

This work takes strides in understanding the thermal micromechanical interactions that MFCs experience due to this effect and leads to a better understanding of how MFCs behave in thermal environments. The pyroelectric coefficient (total, primary, and secondary) is estimated for P1 and P2 MFCs using micromechanical modeling and experimental techniques. The CTE is estimated using micromechanical theory for both MFC types, which is consequently used in the modeling of the pyroelectric coefficient. Secant-based CTEs and Elastic Modulus are used to approximate the properties of the pyroelectric components of MFCs in the regime of linear elasticity.

The total pyroelectric coefficient was experimentally measured using two separate thermal chambers via the linear temperature ramping and thermal cycling methods. These results were compared with measurements taken with a potential electromagnetic interference and used in a figure of merit to determine how well the material functions as an energy harvester using this effect. Experiments were conducted to measure the pyroelectric coefficient under different boundary conditions and compared to the modeled pyroelectric coefficient.

Applications using the pyroelectric effect were explored. Waste energy harvesting is a method of generating small amounts of energy, usually through vibrations or thermal energy. The energy generated through the pyroelectric effect in MFCs was modeled through numerical temperature data, along with two analytical temperature functions, and compared to experimental tests. The maximum specific power was also estimated analytically, numerically, and experimentally. A resistor sweep was performed using the numerical model to calculate the optimal resistance that would provide the most energy. This was validated with experiments conducted at varying resistances. Depending on the size of the MFC, type, resistor used, and the temperature rate, the amount of energy harvested will change and can be optimized for a specified application.

Two proof of concept applications were considered combining pyroelectric energy harvesting with either piezoelectric energy harvesting or structural health monitoring (SHM) in MFCs. Three experiments were conducted, one with just thermal variations, one with just vibrations, and one with both thermal changes and vibrations. The energy was calculated in each case and compared. The second proof of concept application involved using a relay circuit to switch between SHM, which uses impedance measurements as a damage detector, and pyroelectric energy harvesting.

Because this is energy generated from the ambient environment, pyroelectric harvesting can be used to power devices without cost to the source. This form of harvesting can be used in any place where there is a natural thermal cycle (i.e., due to weather or machine giving off thermal energy). Since MFCs are used in a multitude of piezoelectric applications, they can utilize both effects in places where there is a temperature variation with time. This dissertation furthers understanding the pyroelectric effect with the hopes of advancing potential novel applications using MFCs.

CHAPTER 1

Introduction

Energy harvesting is currently a growing topic of interest as people seek ways to efficiently power devices. New innovative methods are being pursued to utilize these alternatives more efficiently and make them more attractive to the public. Waste energy harvesting is an attempt to harvest energy from objects that are already consuming energy using inherent material characteristics. Most waste energy harvesting uses either the piezoelectric, thermoelectric, or pyroelectric effect. The piezoelectric effect is the phenomenon that occurs when a material generates an electric charge due to mechanical stress or strain and vice versa. For example, there have already been inventions that use the vibrations from walking in shoes to charge a battery [1]. Thermoelectricity is where a spatial temperature gradient causes an electric charge, and pyroelectricity is where a temporal temperature difference causes an electric charge. The difference between thermoelectricity and pyroelectricity can be seen in Table 1.1.

In this dissertation, the pyroelectric effect is explored for energy harvesting applications in Macro-fiber Composites (MFCs). The pyroelectric coefficient is modeled and experimentally verified with different boundary conditions for the MFC. The energy harvested is then modeled using this pyroelectric coefficient with a resistance sweep and experimentally measured. Below is a brief introduction to pyroelectricity and MFCs.

Table 1.1: Pyroelectric vs Thermoelectric

Pyroelectricity	Thermoelectricity
1. Generates electricity due to a temporal temperature difference	**1.** Generates electricity due to a spatial temperature difference
2. The whole material is at one temperature, which changes over time	**2.** Requires a heat sink to maintain a temperature gradient within the material
3. Only some piezoelectric materials are truly pyroelectric	**3.** All materials exhibit this effect to a small degree with others having a larger effect

1.1 Background

This section provides a brief background on the subject matter necessary to understand this dissertation. Since this dissertation focuses on MFCs and their potential application using pyroelectricity, the background will go over pyroelectricity and MFCs. The first subsection begins by giving an overview of the history of pyroelectricity and then transitioning towards the theory and describing the pyroelectric coefficient. The second subsection discusses the MFC, including a short history, the composition, the common types of MFC, and their respective applications.

1.1.1 Pyroelectricity

The pyroelectric effect has been observed by scientists and philosophers alike dating back to the 4th Century B.C.E., where a Greek philosopher named Theophrastus wrote about the possible therapeutic properties of the mineral tourmaline and its powers of attraction [2]. It was not until the 18th Century when Sir Charles Linne (Linnaeus) related the pyroelectric effect of tourmaline to electricity. During the 19th Century, the pyroelectric theory began to develop, and contributions were made to the field by well-known scientists (Lord Kelvin, Jacques and Pierre Curie, Woldemar

Voigt, Kundt, Wilhelm Hankel). With the discovery of ferroelectricity in the 20th Century, interest in pyroelectricity diminished. However, some applications were developed, such as for use in infrared detectors and thermal imaging. Today, further applications are being explored as an energy harvester for low power electronics.

Pyroelectric materials are dielectrics. A dielectric material is an insulator, such as a capacitor. When an electric field is applied to a dielectric, a polarization develops within the material. There are several subgroups of dielectrics, as seen in Figure 1.1. The non-centrosymmetric sub-group has a crystal structure that breaks symmetry as stress or strain is applied to the material (also known as piezoelectricity). This asymmetry causes a dipole to form, which generates electricity.

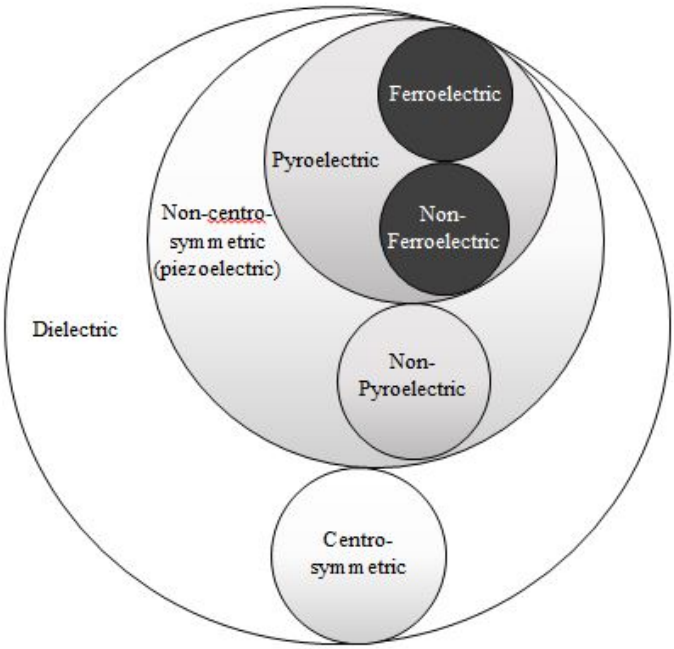

Figure 1.1: Diagram categorizing the subgroups of dielectric materials.

Pyroelectricity is the electrical response of a polar material resulting in a change in temperature over time [3]. The effect occurs because of asymmetry in the material by electrically charged species, which give rise to an electrical dipole moment. If heated, there is a decrease in the sponta-

neous polarization as dipoles lose orientation due to thermal vibrations [4]. This leads to a decrease in the number of free charges bound to the material surface. If cooled, the dipoles regain their orientation leading to an increase in the level of spontaneous polarization, which reverses the electric current flow. The skin on humans is piezoelectric and pyroelectric, and it is what allows the detection of temperature and pressure differences that make up the sense of touch [5]. Ferroelectric materials are pyroelectric and piezoelectric, but not all pyroelectric and piezoelectric materials are ferroelectric. Ferroelectricity is the phenomenon that occurs when the polarization reverses due to a reversed electric field. This reversal forms hysteresis loops commonly seen in polarization vs. electric field figures.

Pyroelectricity is the combined result of a polarized material changing polarization with changing temperature (primary effect, with respect to constant strain) and the coefficient of thermal expansion, causing an induced piezoelectric effect in the material when it changes dimensions (secondary effect) [6]. There is also a tertiary effect (also called the false effect) when there is inhomogeneous heating within the material. The tertiary effect is a function of stress due to thermal strain (with respect to position and time), and the piezoelectric coefficient matrix, however, it is usually considered negligible in comparison to the primary and secondary effects [7]. The tertiary effect will not be explored in this work as the MFC is thin and small compared to the thermal chamber, and the temperature rate of the thermal chamber is slow enough to assume a homogeneous temperature within the MFC. Additionally, there might be an electric field effect if there is an electric field present, and the dielectric permittivity varies with temperature. This effect can significantly change the value of the pyroelectric coefficient. Each of these relationships can be seen in the Heckmann Diagram reproduced in Figure 1.2.

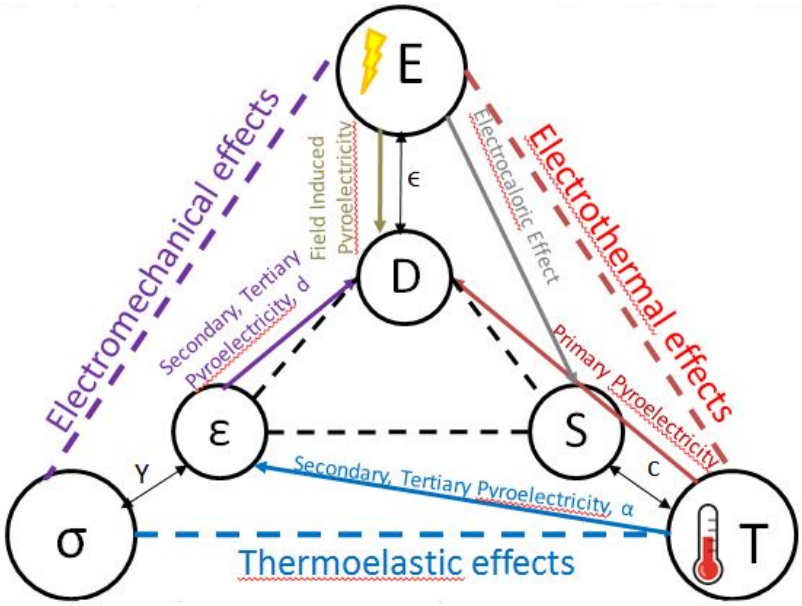

Figure 1.2: Heckmann Diagram illustrating the relationships between mechanical, thermal, and electrical properties and how it connects with pyroelectricity.

The pyroelectric coefficient is a measure of how efficient a material is at converting thermal changes over time into energy. The coefficient can be derived from the electric displacement, *D*:

$$dD_n = \left[\left(\frac{\partial D_n}{\partial \varepsilon_i}\right)^{T,E}\left(\frac{\partial \varepsilon_i}{\partial T}\right)^{\sigma,E} + \left(\frac{\partial D_n}{\partial T}\right)^{\varepsilon,E}\right] dT + \left[\left(\frac{\partial D_n}{\partial \varepsilon_i}\right)^{T,E}\left(\frac{\partial \varepsilon_i}{\partial E_j}\right)^{T,\sigma} + \left(\frac{\partial D_n}{\partial E_j}\right)^{\varepsilon,T}\right] dE_j + \left(\frac{\partial D_n}{\partial \varepsilon_i}\right)^{T,E}\left(\frac{\partial \varepsilon_i}{\partial \sigma_k}\right)^{T,E} d\sigma_k \tag{1.1}$$

where the superscripts σ, ε, E, and T refer to constant stress, strain, electric field, and temperature conditions, respectively with *n, i, j, k, l, m* = 1 – 3 and summation following from the Einstein's indicial notation. Anything that is temperature-dependent in Equation 3.3 will have a contribution to the pyroelectric coefficient. It is useful to look at the constitutive matrix to determine the

measurable quantities described by Equation 3.3:

$$\begin{bmatrix} \varepsilon \\ D \end{bmatrix} = \begin{bmatrix} S & d & \alpha \\ d & \epsilon & p \end{bmatrix} \begin{bmatrix} \sigma \\ E \\ T \end{bmatrix} \tag{1.2}$$

where *S*, *d*, α, ϵ, and *p* are the material's compliance matrix, piezoelectric coefficients, coefficients of thermal expansion, dielectric permittivity, and pyroelectric coefficients. Using Equation 3.3 and Equation 1.2, the full pyroelectric coefficient can be written as:

$$p_n = p_n^{\varepsilon,E} + d_{njk}^{T,E} C_{jklm}^{T,E} \alpha_{lm}^{\sigma,E} + E_r^{\varepsilon} \frac{\partial \epsilon_{rs}}{\partial T}^{\varepsilon} + d_{opq}^{T,E} \sigma(x,t)_{pq}^{E} \tag{1.3}$$

The pyroelectric coefficient at constant strain is defined as the primary coefficient. The primary effect occurs when the spontaneous polarization (P_s) of the material changes with temperature at constant strain. When in constant stress, the piezoelectric coefficient matrix, *d*, the stiffness matrix, *C*, and the coefficients of thermal expansion, α, define the secondary coefficient. If the electric field is not constant, this will also contribute to the pyroelectric effect via the change in dielectric permittivity with respect to temperature. This term is sometimes referred to as the field-induced pyroelectric effect [8]. Lastly, the tertiary coefficient depends on the stress as a function of position, *x*, and time, *t*, induced by a thermal strain.

1.1.2 Macro-fiber Composites

Macro-fiber Composites (MFCs) are a versatile material primarily used in piezoelectric applications. They can be utilized in Structural Health Monitoring (SHM) by calculating the impedance

of the structure and comparing it to a baseline impedance, or actuation primarily used in controlling vibrations, shape-changing in morphing aircraft, energy harvesting, etc. They are composed of Kapton film, epoxy, copper electrodes, and Lead Zirconate Titanate (PZT), a ferroelectric material.

Before the MFC was invented, piezoceramic wafers and thin films were mainly used for these applications. There were several issues with using piezoceramics, namely brittleness and durability. Since the piezoceramic wafers were usually poled along the thickness, it used the weaker d_{31} effect for applications involving actuation. Interdigitated electrodes were developed as a way to utilize the d_{33} effect and used on the piezoceramic wafers to improve their actuation capabilities [9]. Simultaneously, piezoceramic fiber composites were developed where a round piezoceramic fiber was embedded in a matrix and covered with electrodes [10]. This composite allowed for improved flexibility and durability; however, it still used the much weaker d_{31} effect. An improvement was created with the Active Fiber Composite (AFC), invented by Hagood and Bent at the Massachusetts Institute of Technology (MIT) [11]. These used round PZT fibers and combined it with the interdigitated electrodes so that the composite used the stronger d_{33} effect for actuation. There was concern about how well the round fibers were contacting the electrodes, which reduced the performance. Working off of the previous inventions, the National Aeronautics and Space Administration NASA Langley Research Center [12] invented MFCs in 2000 and won the Government Invention of the Year award for 2006 [13]. Instead of using round fibers, the MFC uses rectangular fibers that are from a PZT wafer [14]. These fibers are uniform and have more contact with the electrodes, which improved their actuation performance.

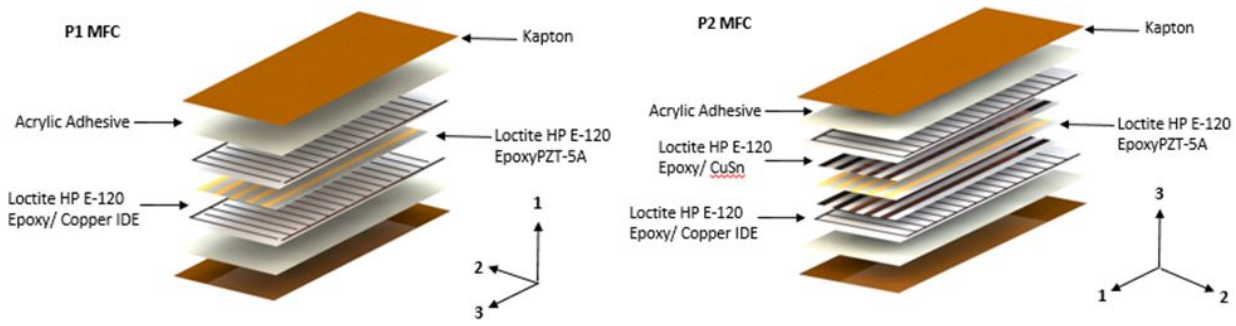

Figure 1.3: The P1 and P2 MFC layers with their respective coordinate systems.

There are two types of commonly commercialized MFCs manufactured by Smart Materials Inc.: P1, where it is primarily utilized in actuation applications and operates via the d_{33} piezoelectric effect, and P2, where it is primarily used in sensing and energy harvesting applications (d_{31} effect). A more detailed explanation of the applications relevant to this dissertation is given in the subsequent subsections. The MFCs are symmetric composites with the layup presented in Figure 1.3. The P1 MFC (poled in the fiber direction) is composed of a PZT/ epoxy layer, an interdigitated copper electrode /epoxy layer, an acrylic adhesive, and a Kapton film. The P2 MFC (poled in the thickness direction) is composed of the same layers, but the electrodes are not interlocking, and there is an extra metal layer on the PZT fibers. For consistency, the poled direction is considered the 3 direction. A 2D schematic of the charge direction is presented in Figure 1.4.

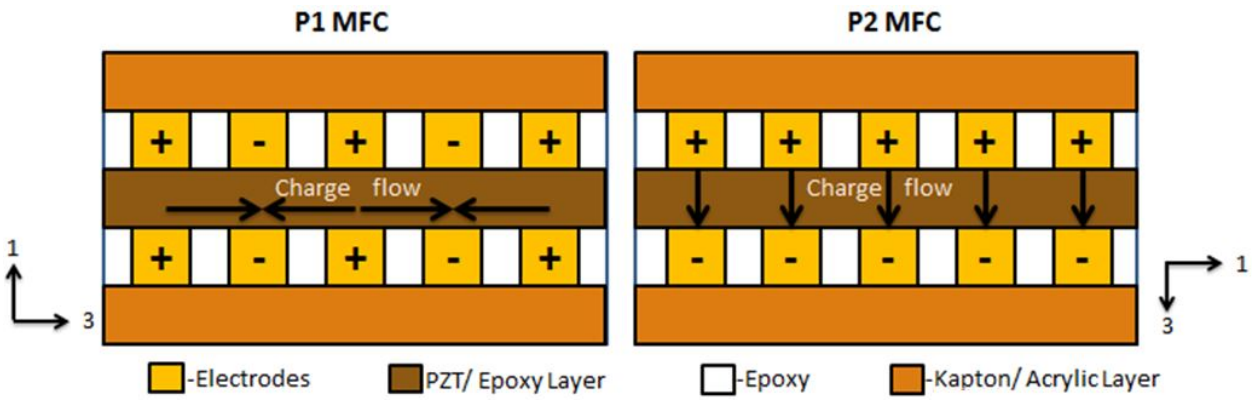

Figure 1.4: The charge flow in the P1 and P2 MFC with their respective coordinate systems.

1.1.2.1 Energy Harvesting

When most people hear the words energy harvesting, they either think of solar panels or wind farms. There are many forms of energy harvesting using different effects as seen in Table 1.2 [15], [16], [17]. Depending on the environment and the application, different effects are more advantageous than others. For instance, even though solar energy tends to be the most efficient energy harvesting method, it is more useful to use another method in places where there is a more abundant energy source such as wind, geothermal, or hydroelectric. The same can be said for low power energy sources, which are typically thought of as human-sourced energy (through thermal gradients, thermal variations, vibrations, etc.). These sources are instrumental in waste energy harvesting for low power applications and can be used in cases where the device is separate from any weather or climate change.

Table 1.2: Types of energy sources and their associated effects

Energy Source	Associated Effect
Solar	Photovotaic
Wind	Mechanical motion via wind to electrical
Geothermal	Mechanical motion via steam to electrical
Thermal	Thermoelectric (Seebeck and Peltier) and Pyroelectric
Deformation	Piezoelectric
Vibrations	Piezoelectric, Electrostatic
Relative Motion	Electromagnetic
Bio-energy	Biological to electrical
Enzymatic	Chemical to electrical
Hydroelectric (Water)	Mechanical motion via falling water to electrical

MFCs can generate energy through both the piezoelectric and pyroelectric effects due to the PZT-5A fiber layer. The PZT crystal structure, as shown in Figure 1.5, is a Perovskite structure where the center atom no longer remains in the center at rest if the material is poled using a strong electric field. This poling aligns the crystal and domains in a certain way, so now it has a remnant polarization. If the material undergoes any deformation or experiences pressure, the crystal structure deforms and gives rise to a dipole. This dipole then generates an electric potential with the continued application of varying pressure or deformation, and is how the piezoelectric effect can harvest energy from vibrations. The pyroelectric effect develops similarly to the piezoelectric effect, where instead of vibrations, it is a homogeneous temperature change with time.

This dissertation explores pyroelectric energy harvesting in MFCs using thermal cycles to vary the temperature. A proof of concept of combining piezoelectric and pyroelectric energy harvesting is also presented.

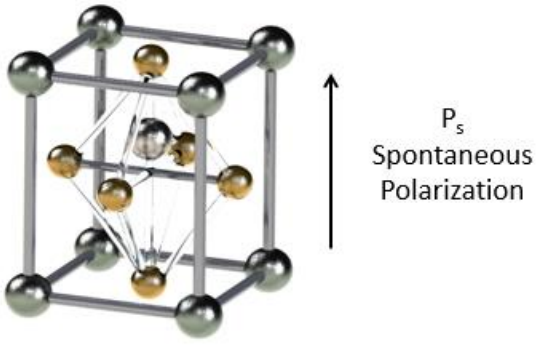

Figure 1.5: The Perovskite crystal structure of PZT, where the middle Titanium or Zirconium atom (silver) is off-center, the Oxygen atoms are on the face (bronze), and the Lead atoms are on the corners (gunmetal). The Titanium or Zirconium atom moves as the temperature changes, generating a changing spontaneous polarization.

1.1.2.2 Structural Health Monitoring

Structural health monitoring SHM is a way to non-destructively observe if there is any damage occurring to a structure or material. For example, without a non-destructive means for checking for cracks in a pipe, the only other method would be to destroy the pipe and look inside to see if there are any cracks. This method is not only non-destructive but can be done remotely with no visuals required.

The way MFCs conduct SHM is through electromechanical impedance monitoring [18]. Impedance measurements are taken by sending frequency sweeps to an MFC bonded to a structure that excites the MFC. A response is sent back via the piezoelectric effect, which can then be converted to the whole structure's impedance. A base impedance is usually taken before any damage might have occurred in the structure and then compared to an impedance measurement taken at a later time. If there is a peak shift in the frequency, then damage might have occurred. Determining if damage has occurred depends on what metric is set for the root mean square deviation (RMSD).

The RMSD is defined as:

$$RMSD = \sum \sqrt{\frac{(Re(Z_{i,1}) - Re(Z_{i,0}))^2}{Re(Z_{i,0})^2}} x100 \tag{1.4}$$

where Z is an array of the real impedance values, i, and the numerical values indicate a post damage impedance and a baseline impedance. The RMSD is usually given as a percentage. If the percentage value is above a predetermined value, then the structure has experienced damage. In this dissertation, taking impedance measurements while collecting energy is explored and is a potential multipurpose application in areas where the temperature might change, such as on a pipe.

1.2 Motivation and Scope

As stated earlier, pyroelectrics have primarily been used as infrared detectors and for thermal imaging because of their sensitivity to temperature changes. MFCs are used in piezoelectric applications such as SHM, vibration damping and suppression, actuation, morphing, energy harvesting through vibrations, etc. Because MFCs contain PZT-5A ferroelectric fibers, they should also exhibit a pyroelectric effect. However, there is very little literature that has explored the pyroelectric effect in MFCs.

In 2010, Xie et al. [19] explored the pyroelectric effect for thin piezoelectric films such as PZT-5A. He characterized the pyroelectric coefficient using thermal cycles to generate a voltage and calculated how much energy and power density it had. In 2012, Zakharov et al [20] explored energy harvesting using an shape memory alloy (SMA) bonded to an MFC. SMAs are alloys that can be deformed and return to its original shape when heat is applied. He used Joule heating

to deform the SMA shape back to the original form, thereby deforming the MFC, which would generate a voltage through the piezoelectric effect. The pyroelectric effect was not considered in this article. A month later in 2012, Suchaneck et al. [21] investigated the validity of using thermal waves as a non-destructive way to determine the polarization of an embedded piezoelectric material (to make sure if it was still operational), such as an MFC, that could be used for structural actuation and sensing. This paper essentially utilized the pyroelectric effect in MFCs for the first time (to the author's knowledge). The pyroelectric current response was both modeled and measured using square-wave modulated semiconductor lasers. The MFC pyroelectric coefficient was assumed to be 120μ C/m^2 K, the same value of the PZT-5A. This coefficient would not be the same value as PZT-5A because the MFC is a composite, so there will be an additional contribution by the secondary effect due to the coefficient of thermal expansion (CTE) mismatch between each layer of the composite [22]. The next serious investigation into pyroelectricity and MFCs was conducted by Zakharov et al. [23] using the same SMA and MFC combination, but now instead of using Joule heating, hot and cold water was used. The MFC itself was investigated to observe if there were any pyroelectric effects, and they found that the MFC exhibited a surprising response of 4 V/ $^\circ$C. They also assumed that the MFC has the same pyroelectric coefficient as PZT-5A.

Though these sources danced around pyroelectricity in MFCs, none of them explored the pyroelectric effect in MFCs to the full extent. The potential applications in waste thermal energy harvesting are extensive. Pyroelectric materials can be used anywhere where there is a temperature change over time. Examples of places include on a CubeSat or Satellite as it orbits Earth due to being exposed and hidden from the sun periodically, in the desert, in airplanes, on hot and cold water pipes, etc. Pyroelectric energy harvesting can even be used as a secondary application where the primary application could be anything that does not require continuous usage of the MFC, such

as SHM. Since MFCs are also piezoelectric and pyroelectric, these two ways of generating energy can be combined to harvest more energy than each one would harvest individually. Vibrations and temperature variations are relatively common in the proximity of a motor.

The pyroelectric effect of MFCs should be well understood in order to use these applications. This dissertation aims to characterize this effect so that it may be used in potential future applications. The pyroelectric coefficient will be investigated thoroughly, the energy generated from a specific temperature profile will be explored, and proof of concepts of harvesting pyroelectric energy while doing impedance measurements and combined piezoelectric and pyroelectric energy will be examined.

1.3 Proposed Concept

The pyroelectric effect requires a temperature difference over time. The faster the temperature difference, the more voltage or current will be generated by the MFC. To characterize the pyroelectric coefficient, an environment where the temperature can be controlled and measured easily is necessary for the MFC. Temperature gradients and external vibrations should be minimized to prevent any false readings from either thermoelectricity, the tertiary pyroelectric effect, or piezoelectricity. There should also be no external electric field or electromagnetic interference (EMI) from any high voltage heating sources that might be near the sample. In addition to experiments, the pyroelectric coefficient was modeled using micromechanics and the rule of mixtures.

For pure pyroelectric energy generation, many of the requirements, as stated above, remain the same. The power and energy can be calculated from the collected voltage. Investigating the combined energy harvested using the pyroelectric and piezoelectric effect requires a vibration source

and a thermal variation with time. Because this is an experiment, the vibration will be artificially introduced, whereas, in the environment, it might come from ambient surroundings. The artificial vibration source will have a standard temperature operating range, which may change the input temperature profile. Combining pyroelectric energy harvesting with SHM involves redirecting the current flow from one application to another. While monitoring structural health, the MFC is sent a frequency sweep by an excitation source and is receiving a response from the structure. Pyroelectric energy harvesting just generates a response. A relay circuit can be used to switch one channel on and off to avoid getting mixed responses. The temperature change will also cause a shift in the impedance peaks for SHM; however, there are literature sources that correct for this peak shift so that damage is not mistakenly identified [24], [25], [26]. As such, this correction will not be implemented in this dissertation.

1.4 Dissertation Outline

This dissertation consists of five chapters. The first chapter provides background on pyroelectricity and MFCs, motivation for pursuing this research, including potential applications, defines the scope, and provides a proposed concept of conducting the research.

Chapter 2 presents the theoretical background and modeling of the pyroelectric coefficient in MFCs. The CTE of both MFCs had to be modeled using a weighted sum of each layer to calculate the pyroelectric coefficient. Because the CTE depends on temperature, a secant method was used to get an average value over the temperature range. The pyroelectric coefficient was modeled using a combination of micromechanics and the rule of mixtures. The total, primary, and secondary contributions were calculated for both the P1 and P2 MFCs.

Chapter 3 discusses experimental work that measures the pyroelectric coefficient of both the P1 and P2 MFCs. These experiments involve using two different methods and chambers to characterize the coefficient. The boundary conditions were also changed to observe how the pyroelectric coefficient was affected. EMI was found to be influencing a set of measurements taken in a specific chamber, which yielded significantly different results.

Chapter 4 analyzes potential applications utilizing the pyroelectric effect in MFCs. These include but are not limited to pyroelectric energy harvesting, combined energy harvesting using the pyroelectric and piezoelectric effects, and SHM while pyroelectric energy harvesting. The pyroelectric energy harvesting is analytically and numerically modeled to find the energy and specific power using the pyroelectric coefficient. This is validated against experiments. The resistance is optimized using the model and compared with experiments with varying resistance. Combined energy harvesting and SHM with pyroelectric energy harvesting are experimental proof of concepts that showcase them as potential applications.

Chapter 5 summarizes the conclusions from all the chapters and the main contributions of this dissertation. The appendices include data from the CTE modeling and experimental pyroelectric coefficient results taken while in a vacuum. A list of references is included.

CHAPTER 2

Modeling the Pyroelectric Coefficient

It is generally challenging to model anything without some empirical constants or a known response to an input. There is a method of predicting the properties of materials from the crystal structure called Density Functional Theory (DFT) [27]. However, this method can be very inaccurate when compared to experimental measurements. In the literature, different methods such as the Asymptotic Expansion approach [28], rule of mixtures and composite connectivity [22], [29], [30], classical lamination theory [31], [32], [33], and finite element analysis [34] have been used to predict the properties of Macro-fiber Composites (MFCs). In this chapter, the pyroelectric coefficient is modeled using micromechanics and the rule of mixtures utilizing empirical material properties of each layer of the composite.

Accurate coefficient of thermal expansions (CTEs) for both MFCs and constituent materials are required to model the secondary effect. The values of the CTE for the P2 MFC do not appear to be available in the literature and are not reported in the manufactures specifications. Therefore, for consistency, equivalent micromechanical models are used to estimate the CTEs for both types of MFCs. The methodology for modeling the properties of the orthotropic layers and CTEs is focused primarily on the rule of mixtures.

2.1 The Pyroelectric Coefficient Vector

Out of the 32 crystallographic point groups, only 10 exhibit pyroelectricity. Of these 10, only the triclinic 1 and monoclinic *m* point groups have multiple pyroelectric coefficients [35]. Because of this, the pyroelectric coefficient is usually treated as a scalar in most literature; however, it is a vector (first-rank tensor) with some materials having multiple coefficients in different directions [36].

A derivation is given below on the vector for the pyroelectric coefficient of Lead Zirconate Titanate (PZT). It is assumed that since PZT is the only predominant dielectric material in the MFC that any significant crystal symmetry impacting pyroelectricity will only matter within the PZT-5A. To start, any crystal structure that has inversion symmetry cannot be pyroelectric. This can be easily shown by performing an inversion operation on the pyroelectric vector as:

$$\begin{bmatrix} p_1' \\ p_2' \\ p_3' \end{bmatrix} = \begin{bmatrix} -1 & 0 & 0 \\ 0 & -1 & 0 \\ 0 & 0 & -1 \end{bmatrix} \begin{bmatrix} p_1 \\ p_2 \\ p_3 \end{bmatrix} = \begin{bmatrix} -p_1 \\ -p_2 \\ -p_3 \end{bmatrix} \tag{2.1}$$

This equates to:

$$\begin{bmatrix} p_1 \\ p_2 \\ p_3 \end{bmatrix} = \begin{bmatrix} -p_1 \\ -p_2 \\ -p_3 \end{bmatrix}$$

by Neumann's Principle, so this can only be satisfied if all the pyroelectric coefficients in this vector are equal to 0.

According to Berlincourt et al. [37], PZT-5A is tetragonal, which either has a point group of 4

or 4*mm*. This point group means it has a four-fold rotational symmetry about the z axis and could have four mirror planes [38]. The rotation symmetry is performed below:

$$\begin{bmatrix} p_1' \\ p_2' \\ p_3' \end{bmatrix} = \begin{bmatrix} cos(90) & sin(90) & 0 \\ -sin(90) & cos(90) & 0 \\ 0 & 0 & 1 \end{bmatrix} \begin{bmatrix} p_1 \\ p_2 \\ p_3 \end{bmatrix} = \begin{bmatrix} p_2 \\ -p_1 \\ p_3 \end{bmatrix} \tag{2.2}$$

By Neumann's Principle, this is only valid when $p_1 = p_2 = 0$. The mirror planes in this crystal structure only reflect across the x or y-axis. So even if there was no rotational symmetry, the symmetry operation would still reduce the vector to p_3 as seen below with two mirror symmetry operations included:

$$\begin{bmatrix} p_1' \\ p_2' \\ p_3' \end{bmatrix} = \begin{bmatrix} -1 & 0 & 0 \\ 0 & -1 & 0 \\ 0 & 0 & 1 \end{bmatrix} \begin{bmatrix} p_1 \\ p_2 \\ p_3 \end{bmatrix} = \begin{bmatrix} -p_1 \\ -p_2 \\ p_3 \end{bmatrix} \tag{2.3}$$

Again, this is only possible when $p_1 = p_2 = 0$. Therefore, the pyroelectric coefficient of PZT-5A can be treated as a scalar with the only remaining coefficient in the vector along the 3 direction (poling direction).

2.2 CTE of MFCs

To model the CTE of MFCs, the material properties of PZT-5A (transversely isotropic), epoxy (isotropic), acrylic adhesive (isotropic), copper electrodes (isotropic), and Kapton (isotropic) are crucial. The values of the properties are presented in Table 2.1 [32], [33], [39], [40]. The temperature-dependent properties are presented with a superscript denoting the temperature. The pyroelectric

coefficient of PZT-5A was experimentally verified against sources [41], [42] with a 2.85 inch by 2.85 inch, 0.0075 inch thick square sample from Piezo Systems Inc. According to Williams et al. [32], there is a glass transition temperature (T_g) for the epoxy within the temperature range of 25 to 100°C, occurring at approximately 62°C. A jump in the CTE and elastic modulus of epoxy is observed at $T = T_g$. In addition to epoxy, the PZT-5A CTEs, and copper CTEs vary with temperature along with their Modulus of Elasticity. The PZT-5A elastic modulus was assumed to be constant over the temperature range for two reasons: 1) The PZT-5A elastic modulus data that varies with temperature from Williams et al. [32] only differs, at most, by 1 GPa at 100°C. 2) The actual temperature variation of the elastic modulus of this form of PZT-5A was not listed by the manufacturer. The temperature dependence of the CTE and Modulus of Elasticity will affect the estimates of the pyroelectric coefficient because the CTE is no longer linear.

Table 2.1: Material Properties of the MFC Layers

Material	**Elastic Modulus (GPa)**	**Poisson Ratio**	**CTE** ($\frac{\mu m}{m^\circ C}$)	**Piezoelectric Constants** ($\frac{pC}{N}$)	**Dielectric Constant**	**Pyroelectric Constant** ($\frac{\mu C}{m^2 K}$)
PZT-5A	$E_1 = 54.05$ $E_3 = 48.31$	$\nu_{12} = 0.35$ $\nu_{23} = 0.38$	$\alpha_1 = 1.20^{25C}$ 1.40^{50C} 1.61^{60C} 1.66^{65C} 1.72^{70C} 2.00^{100C} $\alpha_3 = 4.00^{25C}$ 4.00^{50C} 3.68^{60C} 3.60^{65C} 3.50^{70C} 3.00^{100C}	$d_{15} = 560$ $d_{31} = -185$ $d_{33} = 440$	$\frac{\epsilon_{33}}{\epsilon_0} = 1850$	$p = -205$
Epoxy	$E = 3.38^{25C}$ 3.12^{50C} 2.99^{60C} 2.97^{65C} 2.92^{70C} 2.62^{100C}	$\nu = 0.27$	$\alpha = 73.91^{25C}$ 73.91^{50C} 73.91^{60C} 167.39^{65C} 167.39^{70C} 167.39^{100C}	—	—	—
Acrylic	$E = 3.10^{25C}$ 2.94^{50C} 2.87^{60C} 2.84^{65C} 2.81^{70C} 2.61^{100C}	$\nu = 0.35$	$\alpha = 75.41$	—	—	—
Copper Electrodes	$E = 117.10^{25C}$ 110.94^{50C} 108.47^{60C} 107.24^{65C} 106.01^{70C} 98.61^{100C}	$\nu = 0.31$	$\alpha = 17.02^{25C}$ 17.24^{50C} 17.33^{60C} 17.38^{65C} 17.42^{70C} 17.69^{100C}	—	—	—
Kapton	$E = 2.49^{25C}$ 2.42^{50C} 2.40^{60C} 2.38^{65C} 2.37^{70C} 2.28^{100C}	$\nu = 0.34$	$\alpha = 17.03$	—	—	—

First, the composite properties of the PZT/ epoxy and copper/ epoxy layers are estimated. The

full constituent matrix of orthotropic tetragonal pyroelectric materials is given below:

$$\begin{bmatrix} \varepsilon_1 \\ \varepsilon_2 \\ \varepsilon_3 \\ \varepsilon_4 \\ \varepsilon_5 \\ \varepsilon_6 \\ D_1 \\ D_2 \\ D_3 \end{bmatrix} = \begin{bmatrix} S_{11} & S_{12} & S_{13} & 0 & 0 & 0 & 0 & 0 & d_{31} & \alpha_1 \\ S_{12} & S_{22} & S_{23} & 0 & 0 & 0 & 0 & 0 & d_{32} & \alpha_2 \\ S_{31} & S_{32} & S_{33} & 0 & 0 & 0 & 0 & 0 & d_{33} & \alpha_3 \\ 0 & 0 & 0 & S_{44} & 0 & 0 & 0 & d_{15} & 0 & 0 \\ 0 & 0 & 0 & 0 & S_{55} & 0 & d_{15} & 0 & 0 & 0 \\ 0 & 0 & 0 & 0 & 0 & S_{66} & 0 & 0 & 0 & 0 \\ 0 & 0 & 0 & 0 & d_{15} & 0 & \epsilon_{11}\epsilon_0 & 0 & 0 & 0 \\ 0 & 0 & 0 & d_{15} & 0 & 0 & 0 & \epsilon_{22}\epsilon_0 & 0 & 0 \\ d_{31} & d_{32} & d_{33} & 0 & 0 & 0 & 0 & 0 & \epsilon_{33}\epsilon_0 & p_3 \end{bmatrix} \begin{bmatrix} \sigma_1 \\ \sigma_2 \\ \sigma_3 \\ \sigma_4 \\ \sigma_5 \\ \sigma_6 \\ E_1 \\ E_2 \\ E_3 \\ T \end{bmatrix} \tag{2.4}$$

These set of equations are reformulated where ε is the strain, *D* is the electric displacement, *S* is the compliance matrix, *d* is the piezoelectric coefficient matrix, α is the coefficient of thermal expansion, ϵ is the dielectric constant, *p* is the pyroelectric coefficient, σ is the stress, *E* is the electric field, and *T* is the temperature to take the form:

$$\begin{aligned} \varepsilon &= S\sigma + dE + \alpha T \\ D &= d^T\sigma + \epsilon E + pT \end{aligned} \tag{2.5}$$

At constant stress and constant electric field the total pyroelectric coefficient from Eq 2.5 is

$$p_n = \frac{\partial D_n}{\partial T}^{\sigma,E} \tag{2.6}$$

It was assumed that the layers were perfectly bonded to each other to calculate the effective properties using micromechanics. Moreover, the in-plane strain, electric field, and the temperature were the same for each layer (i.e strain in the *x* and *y* direction if *z* is the thickness). It was also assumed that there are no shear stresses, and the electric field in the 1 and 2 directions is negligible. These assumptions imply that the axial stresses are given by the rule of mixtures:

$$\sigma = \phi^c \sigma^c + \phi^p \sigma^p \tag{2.7}$$

where ϕ^c is the volume fraction of the ceramic (PZT), and ϕ^p is the volume fraction of the polymer in the PZT/ Epoxy layer. Eq. 2.5 is reformulated to apply the rule of mixtures:

$$\begin{aligned} \sigma &= S^{-1}\varepsilon - S^{-1}dE - S^{-1}\alpha T \\ D &= d^T S^{-1}\varepsilon + \left(\epsilon - d^T S^{-1} d\right) E + \left(p - d^T S^{-1}\alpha\right) T \end{aligned} \tag{2.8}$$

Observe that the uniform quantities (ε, *E*, *T*) are placed on the right side of Eq. 2.8. Using Eq. 2.7 and Eq. 2.8, the effective property equations are estimated and presented in Table 2.2.

Table 2.2: Effective in-plane properties of a composite layer using micromechanical modeling.

Rule of Mixture Equations
$S = \left(\phi^c S^{-1,c} + \phi^p S^{-1,p}\right)^{-1}$
$d = S\left(\phi^c S^{-1,c} d^c + \phi^p S^{-1,p} d^p\right)$
$\alpha = S\left(\phi^c S^{-1,c}\alpha^c + \phi^p (S^{-1,p}\alpha^p\right)$
$\epsilon = d^T S^{-1} d + \phi^c\left(\epsilon^c - d^{T,c} S^{-1,c} d^c\right) + \phi^p\left(\epsilon^p - d^{T,p} S^{-1,p} d^p\right)$
$p = d^T S^{-1}\alpha + \phi^c\left(p^c - d^{T,c} S^{-1,c}\alpha^c\right) + \phi^p\left(p^p - d^{T,p} S^{-1,p}\alpha^p\right)$

The estimated effective properties were used for the orthotropic PZT/ epoxy layer and copper/ epoxy layer. Assuming equal in-plane strain in each layer, the net in-plane CTEs are estimated as

the volume average of the effective CTEs of each layer which yields

$$\alpha_i^{MFC} = \frac{\sum_{n=1}^{4} \psi_n N_n^{-1} \alpha_i^n}{\sum_{n=1}^{4} \psi_n N_n^{-1}} \tag{2.9}$$

where the subscript *i* represents the different in-plane CTE directions, the subscript *n* represents the layer, where there are 4 layers since this is a symmetric composite, *N* represents the modified compliance matrix or plane stress stiffness matrix, and ψ is the thickness ratio given in Table 2.3.

However, in the out-of-plane direction, each layer is assumed to expand freely, suggesting the effective out-of-plane CTE is estimated as the weighted sum of the CTEs of the individual layers:

$$\alpha^{MFC} = \sum_{n=1}^{4} \psi_n \alpha_n \tag{2.10}$$

The geometry of the MFC is presented in Williams et al [32] and Smart Materials Inc [43]. The thicknesses and the respective ratios of each layer are presented in Table 2.3. Because CuSn has a small thickness compared to the other layers, it is assumed that it is negligible and will not be considered.

Table 2.3: Thickness of the MFC Respective Layers and Volume Fraction of Copper and PZT

Material	**Thickness (μm)**	**Thickness Ratio**
Kapton	25.40	0.169
Acrylic Adhesive	12.70	0.085
Copper	17.78	0.119
PZT	127.00	0.423
*CuSn (P2 Only)**	1.50	0.010
Epoxy	61.24 58.24 (P2)	0.204 0.194
Total MFC	300.00	—
Copper/Epoxy	—	0.190 (Volume Fraction of Cu in Layer)
PZT/Epoxy	—	0.824 (Volume Fraction of PZT in Layer)

**Provided by Smart Materials Corp*

2.2.1 CTE Results

The variation of the CTE with temperature for MFCs are presented in Figure 2.1. Numerical values at specific temperatures are provided in Table A.1 in the Appendix. The CTE was evaluated at each temperature indicated in Table 2.1 as well as using a secant-based approach to get an approximate estimate. This calculated CTE is different from those found in the literature [32], [33], especially in the transverse direction due to the different assumptions and techniques applied in this dissertation. The mechanical properties vary with temperature, and therefore, using linear elasticity based micromechanics introduces a significant mode of error. For simplicity, the linear elastic framework is kept. However, to better approximate the constitutive relations in this framework, secant-based modeling was applied, as suggested in [44]. To numerically evaluate secant-based coefficients, the trapezoidal rule was utilized to relate α_s (secant-based coefficient), E_s (secant-based elastic modulus) to α (true numerical CTE value at specified temperatures) and E (true

numerical elastic modulus value at specified temperatures) resulting in:

$$\alpha_s = \frac{\sum \frac{1}{2}\alpha \Delta T}{\Delta T} \tag{2.11}$$

$$E_s = \frac{\sum \frac{1}{2} E \alpha \Delta T}{\alpha_s \Delta T} \tag{2.12}$$

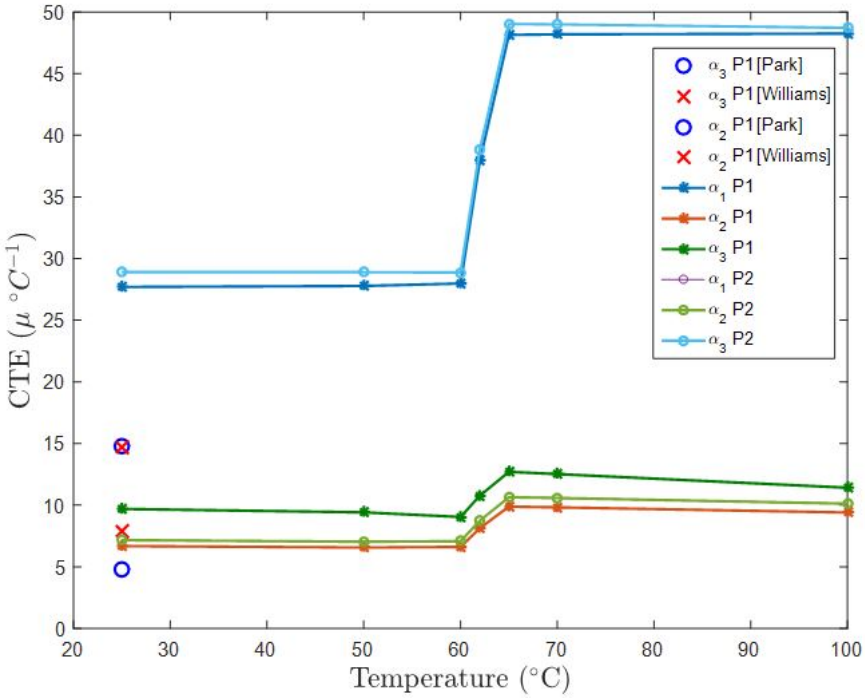

Figure 2.1: The different calculated MFC CTEs as they vary with temperature. The CTE in the thickness direction for both MFCs is much greater than the in-plane CTE.

As presented in Figure 2.1, there is a discontinuity in the CTE in the temperature range of 61 to 63°C. This occurs due to the epoxy properties changing dramatically above its T_g at roughly 62°C. The CTEs of the P1 MFC found in literature are also presented [32], [33].

The electrode configuration (perpendicular to the poling direction) and the CTEs of the MFCs will affect the secondary pyroelectric coefficient. A visual representation is shown in Figure 2.2.

Since the poling directions are different, the d_{33} and d_{31} piezoelectric coefficients are switched. The P1 MFC has a larger CTE in the poling direction than the transverse direction, while the P2 MFC has equal CTEs in both directions due to the out-of-plane poling direction. The differing CTEs will cause different strains to develop within the material. These strains induce different residual piezoelectric effects due to both the switched piezoelectric coefficients and the differing CTEs. This induced piezoelectricity (secondary effect) causes different pyroelectric coefficients to manifest.

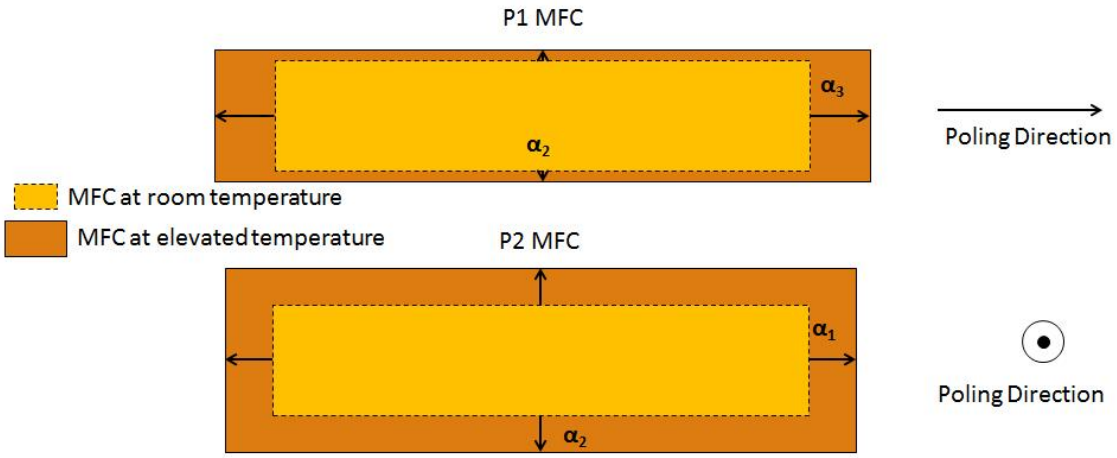

Figure 2.2: A visual representation of both MFCs with the different CTEs as it varies with temperature and poling direction.

The method that was used to manufacture MFCs by NASA [45] was to spread epoxy in between the fibers and the electrodes. Most of the excess epoxy was then removed from the fibers and the top of the copper electrodes. However, the epoxy makes up approximately 81% of the electrode layer, which contacts the epoxy/ PZT layer. In addition, the epoxy from the PZT/ epoxy layer is also in contact with the copper electrodes. Then, the layup was vacuum pressed, so any excess epoxy that was not removed is pushed between the layers creating an extra thickness that is not accounted for in [32]. This extra thickness is stated as the epoxy thickness in Table 2.3.

The lower CTE for the transverse direction of the P1 MFC is caused from the PZT having a lower transverse CTE (1 $\frac{\mu}{^\circ C}$). Also, PZT dominates the volume fraction in the PZT/ epoxy layer and the thickness ratio of the MFC. The CTE of PZT in the poled direction (fiber direction) is $4\frac{\mu}{^\circ C}$. The PZT is transversely isotropic with the plane of isotropy in the 1 and 2 directions. The CTE for the copper/ epoxy layer works out to be isotropic in this instance. The rest of the layers are also treated as isotropic, so the final P2 MFC CTE is transversely isotropic, where the 3 direction is different (in this case the poled direction is the thickness direction).

2.3 Pyroelectric Coefficient of MFCs

Before continuing with the current trajectory of modeling the pyroelectric coefficient using the rule of mixtures, it would be prudent to look over connectivity, how it can be used to predict material properties and how it relates to the rule of mixtures.

2.3.1 Connectivity

Connectivity is a broader term for the rule of mixtures. It is a way to illustrate how materials are connected and how it can potentially change the parameters. Much like a resistor or capacitor, composite materials can be connected in series or parallel, and many other configurations to create the desired parameter. There are about ten different connections briefly covered in [46]. The two main types looked at in this dissertation are series and parallel, as seen in Figure 2.3. Usually, connectivity involves the connection of two materials, which can then be expanded to include other layers. When there is parallel connectivity, this is equivalent to the materials being in uniform strain and would lead to the rule of mixtures for the modulus of elasticity. If the connectivity is in

series, or the transverse direction, this would lead to the inverse rule of mixtures for the modulus of elasticity.

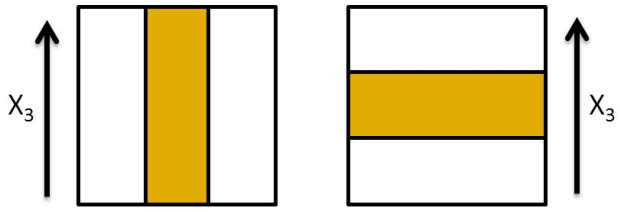

Figure 2.3: (left) Two materials connected in parallel poled along the length of the fiber. (right) Two materials connected in series poled along the thickness of the fiber.

Bhalla and Newnham [22], [47] derived the analytical equivalent pyroelectric coefficient for both series and parallel connections in a diphasic material (that is two phases). These equations are reproduced below assuming both the materials are pyroelectric (MFCs have only one pyroelectric material):

$$p = \phi^c p^c + \phi^p p^p + \frac{\phi^c \phi^p \left(d^c_{33} - d^p_{33}\right)\left(\alpha^p_3 - \alpha^c_3\right)}{\phi^c S^p_{33} + \phi^p S^c_{33}} \tag{2.13}$$

for parallel connectivity and

$$p = \frac{\phi^c p^c \epsilon^p_{33} + \phi^p p^p \epsilon^c_{33}}{\phi^c \epsilon^p_{33} + \phi^p \epsilon^c_{33}} + \frac{2\phi^c \phi^p \left(\epsilon^p_{33} d^c_{31} - \epsilon^c_{33} d^p_{31}\right)\left(\alpha^p_3 - \alpha^c_3\right)}{\left(\phi^c \epsilon^p_{33} + \phi^p \epsilon^c_{33}\right)\left[\phi^c \left(S^p_{11} + S^p_{12}\right) + \phi^p \left(S^c_{11} + S^c_{12}\right)\right]} \tag{2.14}$$

for series connectivity. Again, these equations are for diphasic pyroelectric materials, which is similar to the rule of mixtures for just one pyroelectric and one non-pyroelectric material (i.e., PZT/epoxy) that was derived in the previous section. These equations can be expanded to the whole composite.

2.3.2 Rule of Mixtures

The estimated CTE was employed to compute the pyroelectric coefficient and its constituents. With the assumptions stated previously, Eq. 2.4 is reduced to:

$$\begin{bmatrix} \varepsilon_1 \\ \varepsilon_2 \\ \varepsilon_3 \\ D_3 \end{bmatrix} = \begin{bmatrix} S_{11} & S_{12} & S_{13} & d_{31} & \alpha_1 \\ S_{21} & S_{22} & S_{23} & d_{32} & \alpha_2 \\ S_{31} & S_{32} & S_{33} & d_{33} & \alpha_3 \\ d_{31} & d_{32} & d_{33} & \epsilon_{33}\epsilon_0 & p_3 \end{bmatrix} \begin{bmatrix} \sigma_1 \\ \sigma_2 \\ \sigma_3 \\ E_3 \\ T \end{bmatrix} \tag{2.15}$$

It is assumed that the MFC is in the plane stress condition as the thickness is much smaller than the other dimensions. The choice of coordinate system is determined by the poled direction and, hence, is different for P1 and P2 MFCs. The implication is that the system of equations for the different types of MFCs can be written differently. For P1 and P2, the stresses in the 1 and 3 directions, respectively, are negligible.

It is also assumed that the applied electric fields are negligible. The total strain in the 2 and 3 directions (or 1 and 2 directions for P2) of the PZT/ epoxy layer is the thermal strain experienced by the MFC. With this understanding, Eq. 2.6 and Eq. 2.8 are combined to produce the total pyroelectric coefficient.

$$p = d^{T,PZT/Epoxy} S^{-1,PZT/Epoxy} \left(\alpha^{MFC} - \alpha^{PZT/Epoxy}\right) + p^{PZT/Epoxy} \tag{2.16}$$

At constant strain and electric field, Eq. 2.8 is reduced to the primary pyroelectric coefficient:

$$p = p^{PZT/Epoxy} - d^{T,PZT/Epoxy} S^{-1,PZT/Epoxy} \alpha^{PZT/Epoxy} \tag{2.17}$$

The secondary pyroelectric coefficient is the difference between Eq. 2.16 and Eq. 2.17, written as:

$$p = d^{T,PZT/Epoxy} S^{-1,PZT/Epoxy} \alpha^{MFC} \tag{2.18}$$

2.3.2.1 Pyroelectric Coefficient Results

Even though the pyroelectric coefficient is a material-dependent property, it is also poling direction-dependent. There may be some confusion as to why the pyroelectric coefficient for the P1 and P2 MFCs are not the same. To illustrate this, it would help to analyze the main pyroelectric material, PZT-5A, in two simplified but different cases where each case is the same size, shape, and thickness in the poling direction: 1. Poled along the length of the material with electrodes placed on the shaded face, as seen in Figure 2.4.

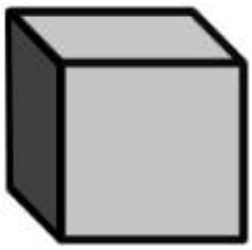

Figure 2.4: A unit of PZT-5A with the electrodes placed along the length of the material denoted by the shaded face. Another set of electrodes are placed along the face parallel to the shaded face.

2. Poled along the thickness of the material with electrodes placed on the shaded face and the face parallel to it as seen in Figure 2.5

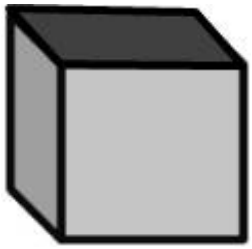

Figure 2.5: A unit of PZT-5A with the electrodes placed along the thickness of the material denoted by the shaded face. Another set of electrodes are placed along the face parallel to the shaded face.

Because this is a monolithic material, theoretically, the pyroelectric coefficient, p_3, is the same magnitude in both of these cases but not in the same direction where the poling direction is different.

However, in the case of the P1 (poled like Figure 2.4) and P2 (poled like Figure 2.5) MFC, since it is a composite, there are material dependencies which affect the pyroelectric coefficient that change with the poling direction. The non-dielectric materials such as epoxy, Kapton, acrylic, and copper electrodes will remain the same between the two MFCs, especially because they are considered isotropic. The PZT-5A material properties are dependent on the poling direction (transversely isotropic), so if there is a coordinate change, the properties are tied to this change. In case 1, the poling direction is along the length of the material, meaning the PZT-5A material properties are referenced so that the axis of crystal symmetry lies along the length of the material. In case 2, the poling direction is along the material's thickness, so the axis of crystal symmetry for PZT-5A is now referenced along the thickness. In addition to this coordinate switching, plane stress was assumed since the MFC is very thin. This plane stress especially makes the calculations different because it essentially disregards the properties in the thickness direction, and for case 2, this is the poling direction and the axis of crystal symmetry. Because of the aforementioned, if the calculations are followed through, the pyroelectric coefficient will be different for each MFC, unlike bulk

PZT-5A.

Using the CTEs calculated earlier, the primary, secondary, and total pyroelectric coefficient are estimated and presented in Figure 2.6 for both MFCs. The T_g of the epoxy is noticeable in the pyroelectric coefficient. The data point between the two extremums is the value calculated using the results from the secant-based method. It is interesting to note that between the MFCs, the total, primary, and secondary coefficient have opposite trends. The primary coefficient is different between the two types of MFCs because the poled direction of the PZT is different, transforming the coordinate system.

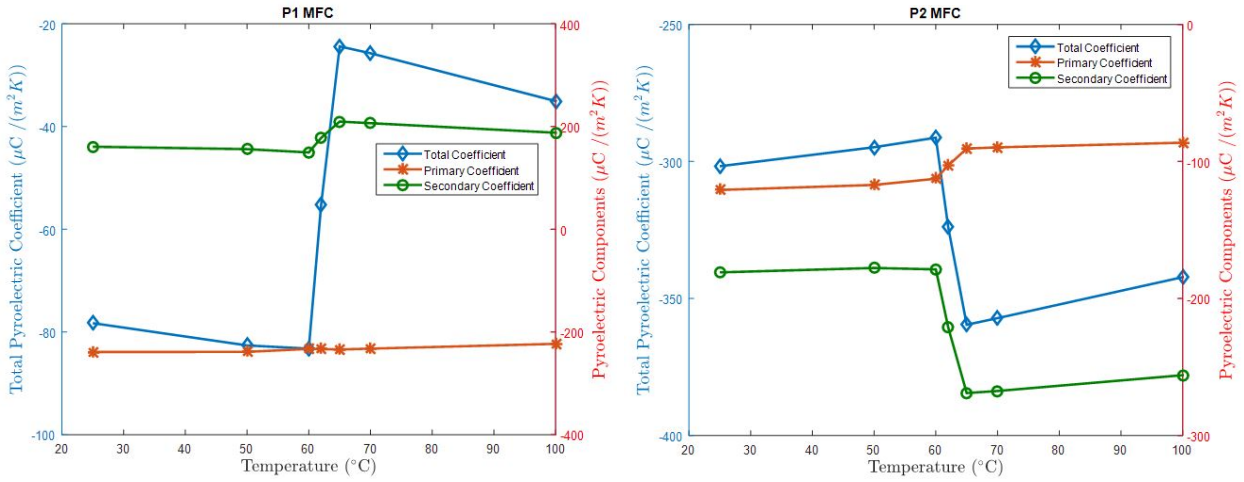

Figure 2.6: (Left) The Pyroelectric Coefficient as it varies with temperature for the P1 MFC with a positive secondary coefficient. (Right) The Pyroelectric Coefficient as it varies with temperature for the P2 MFC with all negative components.

In comparison, the secant method for the total P1 and P2 pyroelectric coefficient was -55 and -324 $\frac{\mu C}{m^2 K}$, respectively. The primary coefficient calculated for the P1 and P2 MFC was -233 and -103 $\frac{\mu C}{m^2 K}$. The secondary coefficient calculated for P1 and P2 was 178 and -221 $\frac{\mu C}{m^2 K}$, respectively. Notice that the secondary coefficient for the P1 MFC is positive, which detracts from the total pyroelectric coefficient, whereas the secondary coefficient for the P2 MFC is the same sign as the

primary coefficient, so it increases the magnitude of the total coefficient. As stated earlier, this difference is due to the different poling directions of the MFC. If the CTEs from [32], and [33] were used instead, then the total pyroelectric coefficients and its constituents at room temperature for the P1 MFC would be -116, -239, and 123 $\frac{\mu C}{m^2 K}$ and -169, -239, and 70 $\frac{\mu C}{m^2 K}$, respectively. Neither source characterized the CTE for the P2 MFC.

2.4 Chapter Summary

The primary coefficient is the change in electric displacement with the change in temperature at constant strain. Thermal effects induce an additional piezoelectric contribution, which results in a secondary pyroelectric effect. These two comprise the total pyroelectric coefficient. Because the MFC is a composite, it will have an additional contribution to the secondary effect due to the CTE mismatch between the different materials and layers. Equivalent micromechanical models were constructed for the P1 and P2 type MFCs to estimate the CTE values. As established in Figure 2.1 and Table A.1, the CTEs for the P1 MFC from Park et al [33] and Williams et al [32] do not agree with the CTE that was calculated in this work. The different assumptions used in this model and the techniques implemented, lead to this disparity. They used a combination of rule of mixtures and classical lamination theory, assuming that the transverse direction for the PZT/ epoxy layer is in constant stress. In this work, it was assumed that each layer of the MFC was perfectly bonded, causing all layers to have a constant in-plane strain. The experimental value of the CTE likely lies between calculated CTE estimated in this work and the calculated CTE provided in Williams et al. [32] and Park et al. [33] since the PZT/ Epoxy layer is probably not in constant stress or constant strain.

Connectivity was briefly mentioned as a broader term for the rule of mixtures. Particularly, series and parallel connections are essential in this dissertation and are analogous to the rule of mixtures and the inverse rule of mixtures.

These CTE values were subsequently applied in the micromechanics based modeling of pyroelectricity. Constitutive equations were estimated assuming uniform in-plane strain and plane stress conditions. Secant-based methods were employed to estimate the CTE and Modulus of Elasticity better as it varied with temperature. The total estimated pyroelectric coefficient, primary coefficient, and secondary coefficient by the secant method were -55, -233, and $178\frac{\mu C}{m^2 K}$ and -323, -103, and $-221\frac{\mu C}{m^2 K}$ for the P1 and P2 MFC, respectively. The secondary coefficient has opposite signs for both MFCs, detracting from and contributing to the total coefficient for the P1 and P2 MFC, respectively.

CHAPTER 3

Experimental Measurement of the Pyroelectric Coefficient

There are a multitude of ways to measure the pyroelectric coefficient experimentally. As reviewed in [8], there are two main techniques of measuring the pyroelectric coefficient: static, where measurements are taken at different constant temperatures, and dynamic, where measurements are taken as the temperature varies over time. The static techniques have been used traditionally, but dynamic methods are being used more frequently in modern times with the advent of new technology capable of measuring time-varying data. There are also multiple ways of heating the sample, such as using a Peltier element, hot plate, thermal chamber, etc. The issue with using a Peltier element or any one-sided heating device is that if the sample is relatively thick, it could cause thermal gradients within the sample, which could falsely skew the data. Ideally, the heating element would increase or decrease the temperature uniformly across the entire sample to mitigate any tertiary pyroelectric effects. Thus, non-contact heating, such as a thermal chamber or a quartz lamp, was chosen as the heating source.

Two dynamic methods were used to find the pyroelectric coefficient in this dissertation. The first is linear temperature ramping, where the chamber was set to a specified temperature rate

and increased linearly. The second is thermal cycling, where the temperature of the chamber was ramped up and down several times at a set temperature rate over several cycles. Two chambers were used, one at the National Aeronautics and Space Administration (NASA) Langley Research Center, and one at the University of Michigan. Having two separate independent setups gives more confidence in the data being the result of pyroelectricity instead of other erroneous sources such as noise or vibration. Both chambers were also used to thermally cycle the Macro-fiber Composites (MFCs), which provided another method of verifying the results.

3.1 Linear Temperature Ramping

Linear temperature ramping is relatively simple to implement. All that is required is a source that can heat or cool the sample at a relatively constant rate, a temperature measuring device, and a device to record all the data. To calculate the pyroelectric coefficient experimentally for a linear ramp in temperature, the Lang and Steckel method [48] was used where the voltage was measured by the data acquisition device (DAQ) with a known shunt resistor, R_{sh} (10 MΩ). Given sufficient time for the temperature to change, and $R_{sh} << R$, the sample resistance, the experimental pyroelectric coefficient is

$$p = \frac{V}{A\frac{dT}{dt}R_{sh}} \tag{3.1}$$

where V is the voltage, A is the active area of the material, and $\frac{dT}{dt}$ is the temperature rate. It is assumed that the difference between the actual area of the electrodes perpendicular to the poled direction and the area of the total Lead Zirconate Titanate (PZT)/ epoxy layer (listed on the Smart Materials website) is negligible going forward. Using Ohm's Law, Eq. 3.1 can be rewritten using

current, I:

$$p = \frac{I}{A\frac{dT}{dt}} \tag{3.2}$$

If the current were measured directly by an ammeter or electrometer, Eq. 3.2 would represent the Byer- Roundy method. Both of these methods assume that the parameter being measured is generated purely from pyroelectricity. These equations relate to the modeling equations in Chapter 2 by using the following:

$$D = \epsilon_0 E + P \tag{3.3}$$

where *P* is the polarization. With constant *E*, the electric displacement equates to the polarization. The polarization collects over the area, which is equivalent to the charge, Q. The charge is also equal to the collection of current with time. Setting these the two relations of charge equal to each other and using Eq. 2.6 yields:

$$\frac{d}{dT}\left(\int_0^t I(t')dt' = PA\right) \tag{3.4}$$

Solving Eq. 3.4 and remembering that the pyroelectric coefficient is defined as the change in polarization over a change in temperature for constant *E*, Eq. 3.2 is derived.

The total current does not necessarily equal the pyroelectric current. A disadvantage of linear temperature ramping is that it is necessary to have cooling data to eliminate any current that is not pyroelectric in origin (i.e., thermally stimulated currents). The thermally stimulated currents (TSC) can cause an added contribution to the total current and are mainly caused by imperfections and defects in the material released upon heating. The total current is defined as the sum of the

pyroelectric current, I_{pyro}, and the TSC, I_{TSC}:

$$I_h = I_{pyro,h} + I_{TSC,h}$$
$$I_c = I_{pyro,c} + I_{TSC,c} \tag{3.5}$$

where the subscripts *h* and *c* represent the heating and cooling of the material and its corresponding temperature rates and currents. Assuming that $I_{TSC,h} = I_{TSC,c}$, Eq. 3.5 can be rewritten to solve for I_{pyro} when heating:

$$I_{pyro,h} = I_h - \frac{\left(I_h \frac{dT}{dt}_c - I_c \frac{dT}{dt}_h\right)}{\frac{dT}{dt}_c - \frac{dT}{dt}_h} \tag{3.6}$$

A similar expression can be derived for $I_{pyro,c}$. Using Eq. 3.6, the linear temperature ramping method is more accurate and valid than without accounting for TSCs, as discussed in the next section.

3.1.1 Linear Ramping Measurements

Experiments were performed at the University of Michigan and NASA Langley Research Center. At the University of Michigan, a 28 x 14 mm active area MFC was hung inside a thermal chamber and connected to a DAQ with a 10 MΩ resistor across the measuring channel to amplify the voltage signal. Unlike piezoelectricity, pyroelectricity requires high resistance to limit leakage current and generate a higher value for voltage. Because the pyroelectric current (especially since the MFCs are small) is in nA, a large resistor, like 10 MΩ, is needed to separate the pyroelectric voltage from the noise produced by the DAQ. The voltage was recorded over time as the chamber ramped from room temperature (25°C) to 70°C with a sampling rate of 10 Hz. Different ramp rates

were used starting at 5°C per min, 7.5°C per min, 10°C per min, and 15°C per min and as fast as possible. A Resistive Temperature Device (RTD) was used to collect data on the temperature. The RTD (Analog Devices TMP36) was calibrated based on the profile curve that was in the datasheet for the RTD [49]. It was then hung inside near the MFC and the internal chamber RTD, with the setup shown in Figure 3.1. Three different trials were conducted with two P1 and two P2 MFCs.

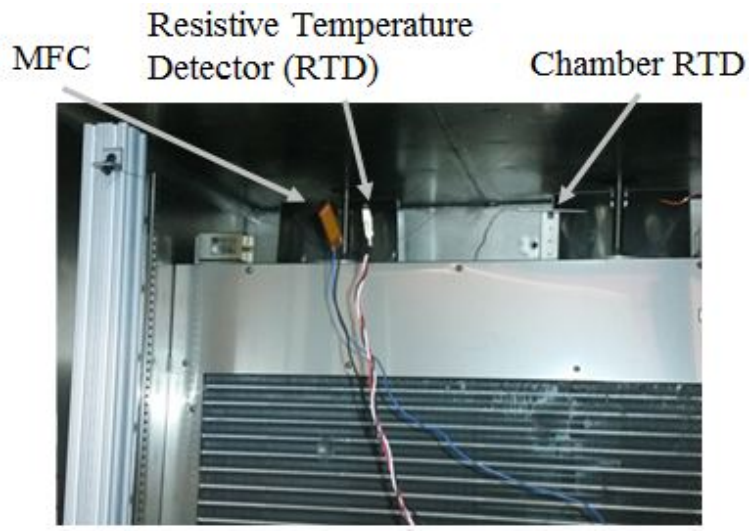

Figure 3.1: The setup in the University of Michigan altitude chamber showing the placement of the MFC and RTD in comparison to the chamber's RTD.

The chamber used at NASA Langley Research Center was a crystal quartz lamp furnace with cooling capabilities. This furnace encircles the sample and has four quartz lamps that are equidistant from each other. It has a gas port and water ports to cool the jacket of the furnace. A chiller that cooled water to 11°C was connected to the jacket. The controller for the lamps was then autotuned to allow finer temperature control with the cooling on continuously. Aluminum foil was placed around the sample and the thermocouple/ RTD to protect against any potential electric interference and normalize the heat absorbed through light as the surfaces had different absorptivities. The

setup is shown in Figure 3.2.

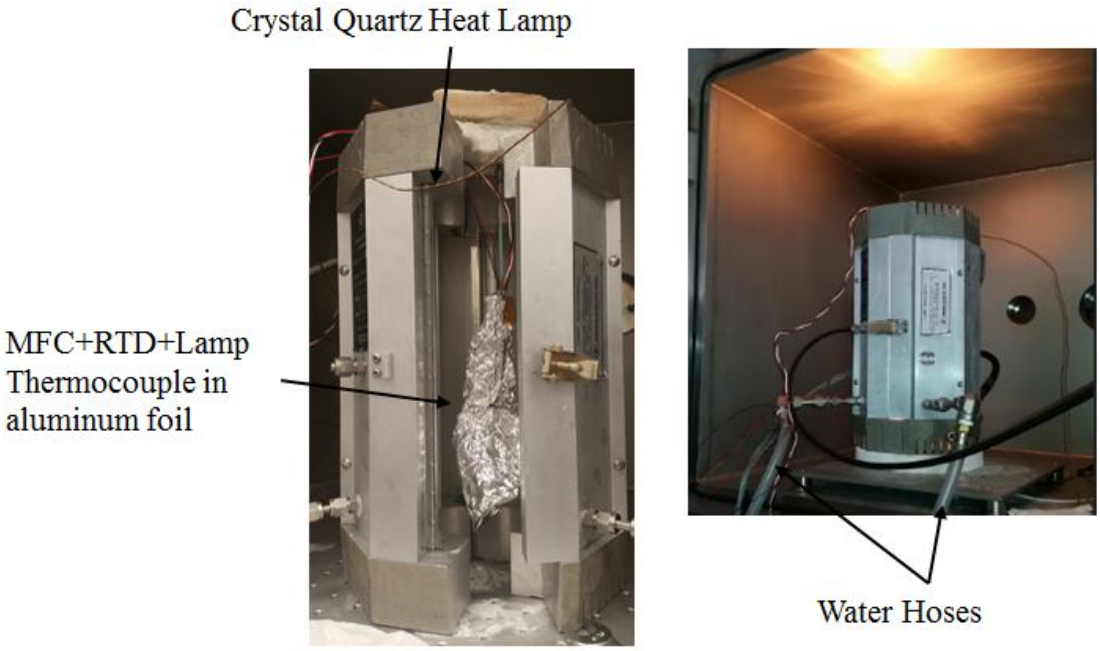

Figure 3.2: The setup at NASA Langley showing the inside and outside of the crystal quartz lamp furnace with the water hoses connected.

Because cooling data was collected, the TSCs could be subtracted out to get just the contribution from the pyroelectric effect. Before any analysis was completed, the current (calculated from the voltage data and the 10 MΩ load resistance) and temperature were filtered using a second-order Butterworth filter until the temperature derivative was smooth for both data sets. In Figure 3.3 below, a series of normalized temperature and current graphs can be seen of a P1 type MFC with a temperature ramp of 7.5°C per minute taken at NASA Langley.

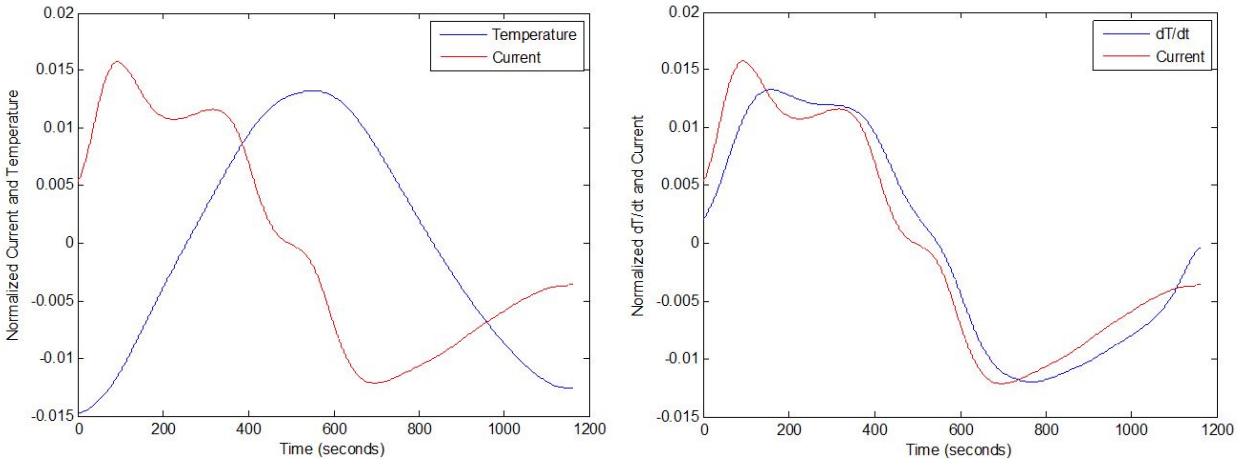

Figure 3.3: To the left is a graph of normalized current and temperature vs. time. To the right is a graph of normalized temperature rate and current vs. time.

The temperature rate and current should be proportional to each other, as indicated by Eq. 3.2. As seen above, the temperature rate and current follow each other closely in shape and amplitude. The pyroelectric coefficient was computed using a linear least-squares regression, which was used on the filtered data to find the most accurate slope between current (converted from voltage using the shunt resistor) and temperature rate (Eq. 3.2). The formula used is

$$p = \frac{[I]\left[\frac{dT}{dt}\right]^T}{\left[\frac{dT}{dt}\right]\left[\frac{dT}{dt}\right]^T A} \tag{3.7}$$

A range of data was chosen where the slope of the temperature data seemed to be the smoothest, excluding startup and end effects where the temperature rate was different. The average of the temperature rate data was calculated and used as the experimental temperature rate. Both the temperature rates and the pyroelectric coefficients were analyzed and are nearly normal distributions. The mean and standard deviation for both MFCs were taken to get an overall pyroelectric coefficient. This statistical data is displayed in Tables 3.1 and 3.2. (Note: The pyroelectric coefficient is gener-

ally reported as negative due to the polarization decreasing as it approaches the Curie Temperature, hence the negative in front of the units in the tables.)

Table 3.1: Pyroelectric Coefficient NASA Langley Chamber Crystal Quartz Lamps

Temperature Rate		**MFC Type**			
Desired (°C/min)	**Experimental (°C/min)**	P1 $\left(\frac{-\mu C}{m^2 K}\right)$		P2 $\left(\frac{-\mu C}{m^2 K}\right)$	
		Before TSC	After TSC	Before TSC	After TSC
5	6.25 ± 0.84	76.32 ± 93.37	96.81± 16.80	220.58 ± 78.21	354.43 ± 18.51
7.5	8.33 ± 1.10	47.54 ± 74.88	98.38 ± 17.67	206.02 ± 13.80	336.88 ± 3.68
10	11.11 ± 1.29	87.42 ± 60.33	89.73 ± 27.87	166.56 ± 44.21	338.93 ± 2.43
15	16.82 ± 1.88	75.49 ± 63.69	90.22 ± 15.73	184.96 ± 70.86	355.22 ± 5.12
	Overall Average	71.04 ± 69.64	93.28 ± 17.39	193.79 ± 55.32	347.04 ± 12.04

Table 3.2: Pyroelectric Coefficient Michigan Chamber

Temperature Rate		**MFC Type**			
Desired (°C/min)	**Experimental (°C/min)**	P1 $\left(\frac{-\mu C}{m^2 K}\right)$		P2 $\left(\frac{-\mu C}{m^2 K}\right)$	
		Mean	Standard Deviation	Mean	Standard Deviation
5	3.91 ± 0.19	222.05	20.73	353.57	5.83
7.5	5.51 ± 0.19	183.64	10.20	341.76	4.89
10	7.23 ± 0.40	154.45	15.35	343.83	5.52
15	10.60 ± 0.41	134.68	8.90	341.53	7.60
Fast as possible	15.30 ± 2.63	110.85	21.80	305.10	56.09
	Overall Average	161.14	42.16	334.39	32.51

As seen in Table 3.1, the standard deviation is higher than some values for the P1 sample, indicating that something is causing a variation other than noise. After the TSCs were removed, the values became more consistent, and the standard deviation dropped to more reasonable levels, providing evidence that TSCs play a significant role in affecting the pyroelectric coefficient measurement.

Data was taken previously at NASA Langley using an induction coil furnace with no cooling capability (results can be seen in the next section). Due to this limited capability, cooling data was not taken for the Michigan chamber to match this previous experiment closely. It was not until later that it was realized that cooling data is needed. However, just from comparing Table 3.1 and 3.2, the pyroelectric coefficient is vastly different and not consistent for the P1 MFC. The P2 MFC has similar values between the results in the Michigan chamber and after the TSCs were removed from the NASA chamber. These different responses may indicate that the P1 MFC is more sensitive to TSCs than the P2 MFC, likely due to the differences between both MFCs (such as the interdigitated electrodes and poling directions).

3.2 Thermal Cycling

A better method of isolating the actual pyroelectric current is by thermally cycling the material. The temperature rate and the current should be in phase with each other, and the current should be 90° out of phase with the temperature. Because there should be a phase difference, any non-pyroelectric current can be corrected for by multiplying it with a sine function.

The pyroelectric coefficient was calculated using a slightly different equation than the temperature ramping in Eq. 3.2. The formula used is [8]

$$p = \frac{I_{amp} sin(\phi)}{A \omega T_{amp}} \tag{3.8}$$

where ω is the angular velocity equal to $2\pi f$ where f is the frequency. The fast fourier transform (FFT) was used to find the amplitude of the current and temperature data, as well as the frequency.

If there were multiple peaks shown in the FFT plot, only the first one was used, as it was primarily the biggest. The angle, ϕ, represents the phase shift between the current and temperature. Ideally, this should be 90° out of phase, so the current is at its largest. Any deviation from 90° indicates that there are other contributions to the current other than pyroelectric sources. The angle between the temperature and current was calculated from

$$\phi = cos^{-1}\left(\frac{\overline{I}\cdot\overline{T}}{|\overline{I}||\overline{T}|}\right) \tag{3.9}$$

This equation takes the arccosine of the dot product between the two vectors divided by the product of the vector magnitudes to find the angle. Typically, this value was between 86° and 95° for the Michigan chamber and 60° and 120° for the NASA chamber.

3.2.1 Thermal Cycling Measurements

The same setup as the linear ramping was utilized. In the Michigan chamber, the temperature was increased to 70°C and held there for 20 minutes so the temperature could reach a steady state. It was then cycled up to 100°C, and back down to 40°C, seven times at the same temperature rates listed previously for the Michigan chamber. A representative temperature profile can be seen in Figure 3.4.

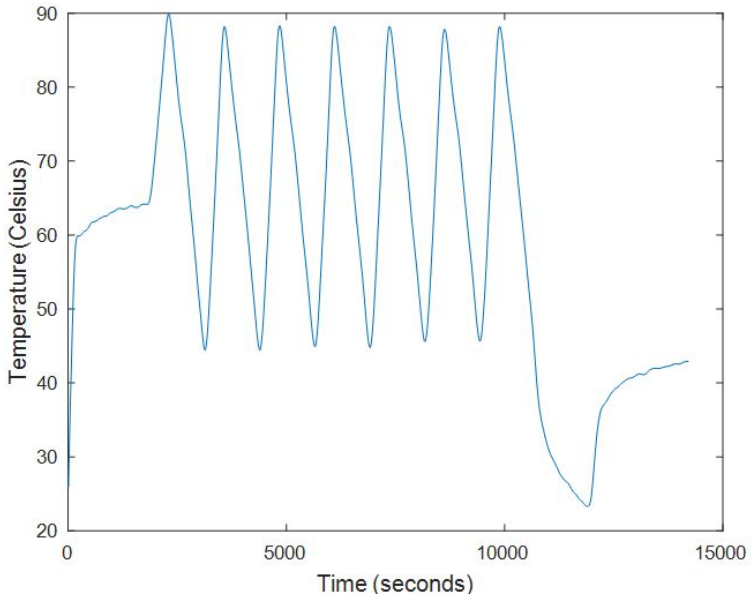

Figure 3.4: Temperature profile of the thermal cycles done at 5°C per minute at the University of Michigan. The minimum and maximum temperature difference became smaller as the temperature rate increased.

The data for the thermal cycles were also filtered using a second-order Butterworth filter. The data range used for the calculations was when the current from the MFCs reached the first local minimum to the last local minimum, as seen in Figure 3.5. The current and temperature rate were also zeroed.

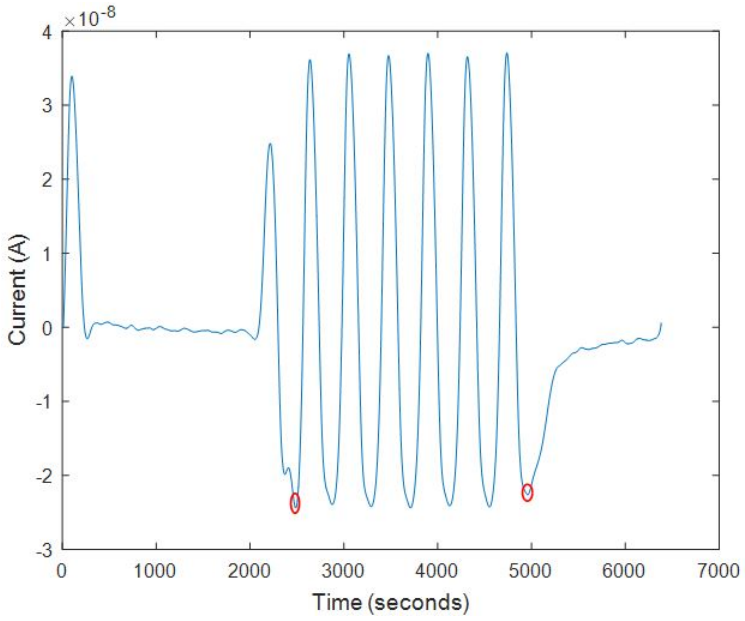

Figure 3.5: A graph of the current generated from the 15°C per minute thermal cycle using a P2 type MFC. The red circles indicate where the data range starts and ends.

As with the temperature ramping, the current and temperature rate are proportional. It can be seen in Figure 3.6, illustrating that the current and temperature rate should follow the same trend even when thermal cycling. There are slight deviations in the profile with minute kinks that contribute to a slight phase difference, reflecting onto the phase difference between the temperature and current.

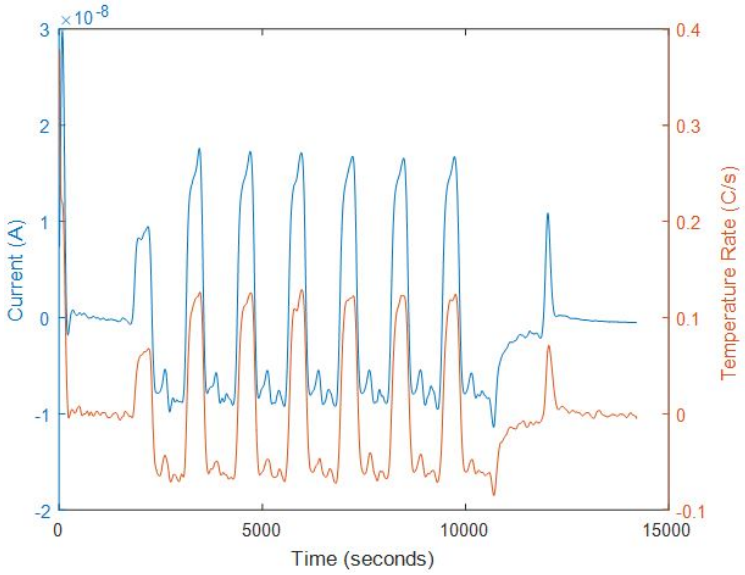

Figure 3.6: This graph compares the current and temperature rate using different axes. The profiles are the same, while the amplitude is different.

Tables 3.3 and 3.4 below shows the pyroelectric coefficient values of the temperature cycles. This data was analyzed the same way as the temperature ramped results above by taking the mean and standard deviation. In the interest of time, for some rates, not all three trials were conducted for the NASA chamber. The N/A indicates that there was only one trial conducted at that temperature rate. A graph of all the pyroelectric coefficient trials can be seen in Figure 3.7.

Table 3.3: Thermally Cycled Pyroelectric Coefficient NASA Langley Chamber

Temperature Rate		**MFC Type**	
Desired (°C/min)	**Experimental (°C/min)**	P1 $\left(\frac{-\mu C}{m^2 K}\right)$	P2 $\left(\frac{-\mu C}{m^2 K}\right)$
5	7.15 ± 0.05	91.11 ± N/A	323.59 ± 12.19
7.5	10.18 ± 0.49	71.35 ± 13.77	314.06 ± 24.51
10	13.16 ± 0.42	86.74 ± 6.43	320.55 ± 8.83
15	17.14 ± 0.41	90.14 ± 8.63	347.40 ± N/A
	Overall Average	82.85 ± 12.00	322.05 ± 17.14

Table 3.4: Thermally Cycled Pyroelectric Coefficient Michigan Chamber

Temperature Rate		**MFC Type**			
Desired (°C/min)	**Experimental (°C/min)**	P1 $\left(\frac{-\mu C}{m^2 K}\right)$		P2 $\left(\frac{-\mu C}{m^2 K}\right)$	
		Mean	Standard deviation	Mean	Standard deviation
5	5.77 ± 0.37	76.02	4.07	327.96	13.17
7.5	7.95 ± 0.11	78.24	4.11	329.14	17.93
10	9.83 ± 0.35	81.10	2.55	343.26	10.27
15	13.04 ± 0.20	84.60	2.54	352.00	6.61
Fast as possible	16.31 ± 0.33	91.02	4.34	361.48	3.65
	Overall Average	82.20	6.32	344.31	14.95

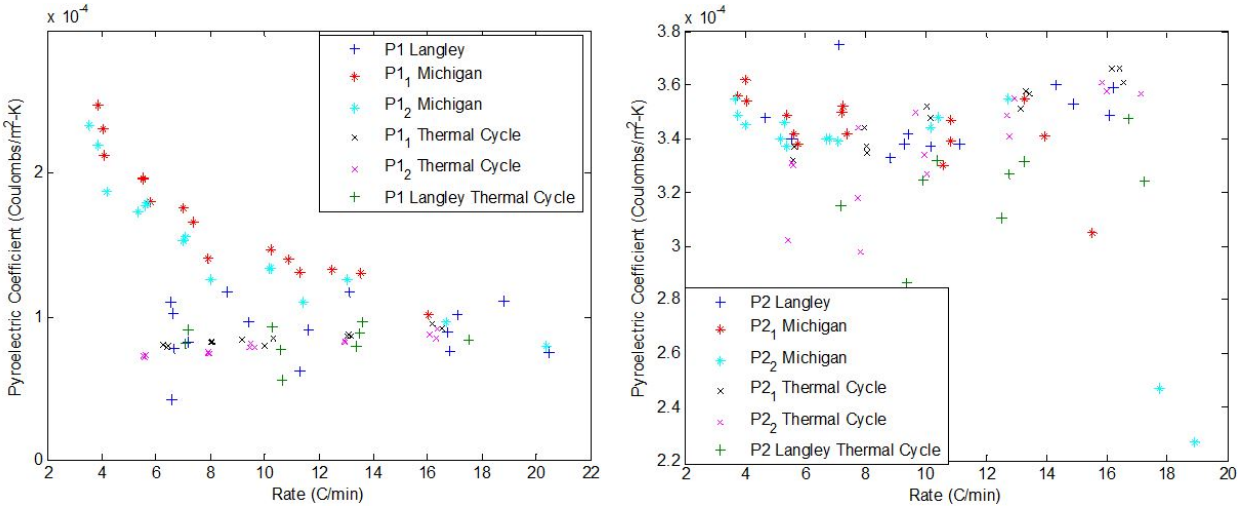

Figure 3.7: (Left) A graph comparing all the P1 MFC trials which show a decreasing trend for the Michigan data. (Right) A graph comparing all the P2 MFC trials showing similar values. These values represent the absolute value and should be negative otherwise.

As seen in Figure 3.7, there is not a lot of variation between the NASA and Michigan results. The Michigan linear ramping for the P1 type and the thermal cycle data have the most variation, but that is due to the TSCs present in the linear ramping data. All the values cluster around 80 to $90 \frac{\mu C}{m^2 K}$ for the P1 pyroelectric coefficient except for the linear ramped Michigan data. This data was taken before it was known to compensate for TSCs. As shown by this result, not subtracting

TSCs does make an impact on the coefficient and will not match with the thermally cycled results.

In contrast, even with the TSCs, the P2 type Michigan data sets match. The P2 coefficient results are clustered between 310 and 360 $\frac{\mu C}{m^2 K}$. The TSCs were also not subtracted for the linearly ramped Michigan results, but there is hardly any noticeable difference (just at the beginning and end of the graph). The similarity in the P2 results suggests that the P1 MFC is more sensitive to TSCs, maybe due to the small current it generates in comparison to the P2 MFC. Again, this difference in current is probably due to the way the MFC types are manufactured, referencing Section 2.3.2.1. The P1 MFC has interdigitated electrodes, which limits the current that can pass through it, whereas the P2 MFC has a parallel plate electrode configuration that allows more current flow, and therefore has a higher pyroelectric coefficient. Due to the tiny current produced by the P1 MFC, other contributions such as TSCs or noise from the DAQ can significantly affect the pyroelectric coefficient. The slower the ramp rate, the smaller the current will be, which makes it more susceptible to other sources. This conjecture is supported by the downward trend rate the linear ramped data has towards the NASA chamber and thermally cycled values as the rate is increased, because the pyroelectric current contribution should increase as the rate increases. Due to the differences in electrode placement on the different types of MFCs (poling directions), the total pyroelectric coefficient for both types is different.

3.3 Electric Field Pyroelectric Enhancement

Electromagnetic interference (EMI) is an environmental influence from electronic sources that can disrupt the performance of nearby electrical objects. It has two effects, electromagnetic induction where current is induced in a loop due to a change in a magnetic field, and electromagnetic

radiation where the electric field is radiated out from an object. CubeSats frequently have to worry about mitigating EMI. The pyroelectric coefficient can actually be enhanced without additional energy in creating an electric field using this unintended EMI. The drawback is that there is no control over the strength of the electric field experienced. An electric field, in conjunction with a change of temperature with time, is utilized extensively throughout literature in harvesting pyroelectric energy using either Carnot, Brayton, or Ericcson (Olsen) cycles [50], [51], [52], [53], [54].

The MFCs (28 x 14 mm) were suspended in a small Thermolyne 47900 furnace with an RTD as close to the MFC as possible at NASA Langley Research Center, as shown in Figure 3.8. A Measurement Computing DAQ was used to collect data and was read by a laptop using the DAQami software. A 10 MΩ resistor was placed in parallel with the MFC to amplify the voltage above the noise of the DAQ.

Figure 3.8: The experimental setup showing the MFC and RTD in the NASA thermal chamber connected to the DAQ.

The thermal chamber was calibrated before using it for the first time through an autotune feature within the Proportional Integral Derivative (PID) controller of the chamber. The temperature is

programmed to a set point, and the chamber calibrates itself by calculating the gain factors needed to control the temperature rate around that specified temperature. The chamber was ramped from room temperature up to 70°C, as shown in Figure 3.9, at varying temperature rates. The actual temperature recorded by the RTD differed from the temperature the chamber thermocouple measured. The door to the chamber was opened to expedite the temperature returning to ambient conditions through air convection. The DAQ was stopped once the temperature reached approximately 50°C as the cooling temperature rate considerably slowed as it approached room temperature.

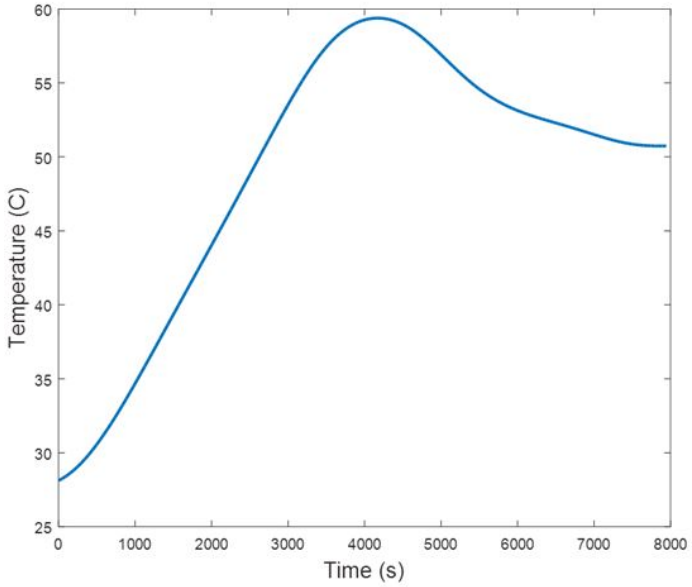

Figure 3.9: A sample temperature profile starting near room temperature and showing the linear ramp of temperature with time as well as the cooling data.

It is theorized that the EMI might be radiating from the open coil electric resistance heaters since the MFC is within a few centimeters of the coils, as seen in Figure 3.10. The coils are likely producing an electric field as high voltage and, consequently, a current is flowing through them to heat the furnace. In addition, there is likely an induced current in the MFC due to a magnetic flux from the coils as stated in Faraday's Laws (a magnetic field might be generated from the current

running through the coils which changes in magnitude due to the PID controller and any loop in the MFC that is being affected by this magnetic flux would generate an induced current). Experiments were also done with a makeshift Faraday's cage using aluminum foil to cover the MFC to shield it from the electric field. These experiments matched the pyroelectric coefficient results in other thermal chambers.

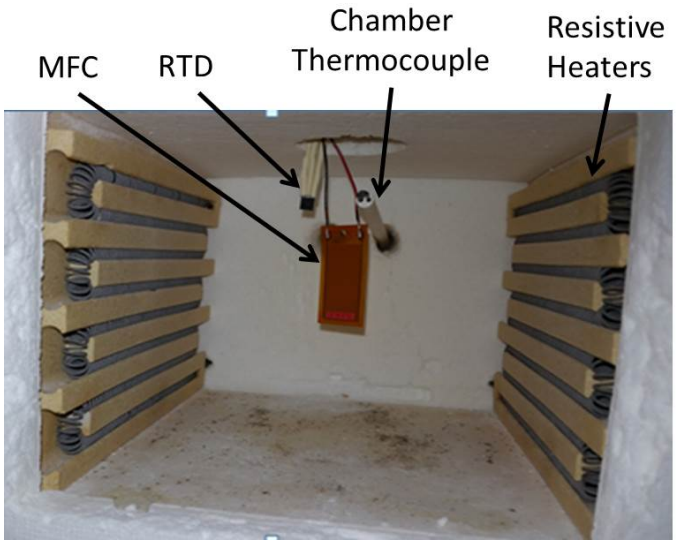

Figure 3.10: A close up of the setup inside the Thermolyne NASA chamber which shows the coiled resistive heaters, the MFC, RTD, and chamber thermocouple.

The pyroelectric coefficient for both P1 and P2 types is illustrated in Figure 3.11 as a function of temperature rate. The actual pyroelectric coefficients averages ($82.2\frac{\mu C}{m^2K}$ for P1 and $344.3\frac{\mu C}{m^2K}$ for P2) taken from the previous sections is depicted as a straight line varying with temperature rate and is called the reference pyroelectric coefficient. The pyroelectric coefficient values with the aluminum foil wrapped around the MFC and RTD were also included. It can be noted that these values very nearly match the reference pyroelectric coefficient.

The average reported value of the pyroelectric coefficient for both MFC types is subtracted from the generalized pyroelectric coefficient to estimate the field-induced pyroelectric coefficient.

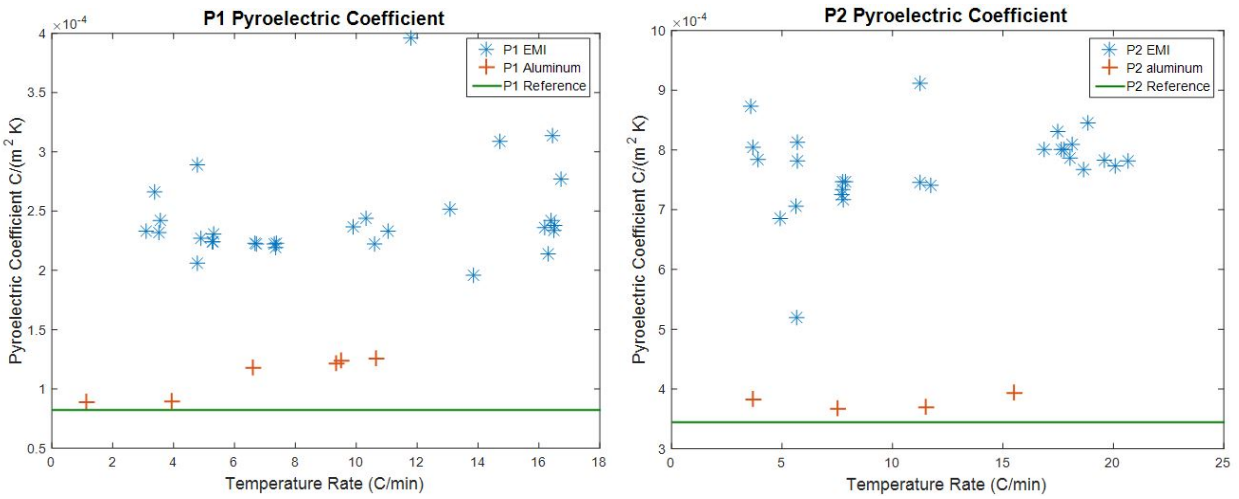

Figure 3.11: Pyroelectric coefficient for the P1 MFC (left) and P2 MFC (right) as a function of temperature rate. The pyroelectric coefficient at constant stress and electric field is also shown as well as the average value reported earlier.

Again, this calculation assumes that the tertiary pyroelectric effects are negligible; therefore, the only difference between these coefficients is the presence of EMI. The average field-induced pyroelectric coefficient is $162\frac{\mu C}{m^2 K}$ and $427\frac{\mu C}{m^2 K}$ for the P1 and P2 MFCs, respectively.

As demonstrated by Figure 3.11, the electric field of the thermal chamber affects the pyroelectric coefficient. There is a noticeable increase in both the P1 and P2 MFC pyroelectric coefficients due to EMI. In Figure 3.11, the measured chamber pyroelectric coefficient is approximately twice as much as the reference pyroelectric coefficient. In fact, the induced field pyroelectric coefficient, found by subtracting the reference coefficient and the measured coefficient, comprises more than half of the contribution to the measured coefficient.

These values can be used to compute the average electric field effect on both MFCs if the rate of dielectric permittivity with respect to temperature is known. It is assumed that this rate for both MFCs is the same as PZT-5A since that is the only dielectric material present in this composite. Using the graph of the percent deviation of the relative permittivity vs. temperature for PZT-5A

from [55] and a webplot digitizer that calibrates the pixels with a graph axis, allowing specific points to be selected, a trendline was generated from the data. For a small temperature range and low temperature, the dielectric constant should vary linearly with temperature. The percent deviation of the relative permittivity was converted to the material dielectric permittivity, ϵ_{33}, and is shown in Figure 3.12. It is assumed that at room temperature, the value of ϵ_{33} for the P1 and P2 MFCs are $1593\epsilon_0$ and $1600\epsilon_0$, respectively [29].

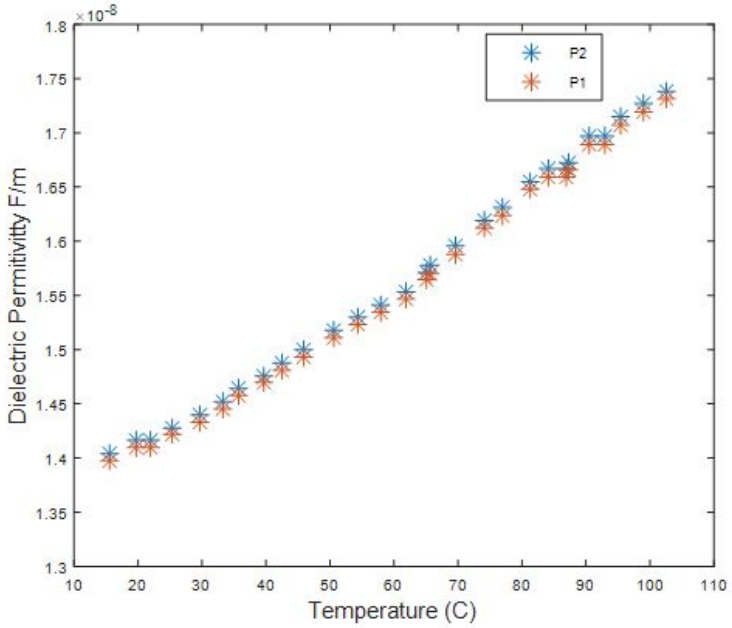

Figure 3.12: The dielectric permittivity as a function of temperature, assuming the rate of dielectric permittivity as a function of temperature is the same as PZT-5A for both MFCs.

A trendline was matched to both datasets in Figure 3.12 to get the y- intercept and the slope (the change in dielectric permittivity with temperature). The slope and y-intercept for the P1 MFC are $4.001 * 10^{-11}\frac{F}{m°C}$ and $1.316 * 10^{-8}\frac{F}{m}$, respectively and $4.019 * 10^{-11}\frac{F}{m°C}$ and $1.322 * 10^{-8}\frac{F}{m}$, respectively, for the P2 MFC. Dividing the average field induced pyroelectric coefficient by this slope will yield the average effective electric field (Eq. 1.3). The effective electric field experienced by the P1 and P2 MFCs are approximately $4.05\frac{MV}{m}$ and $10.6\frac{MV}{m}$.

The effective electric field was calculated from the change in dielectric permittivity with respect to a change in temperature. Again, this is under the assumption that this change in dielectric permittivity with respect to temperature is the same as PZT- 5A for both MFCs and that all the extra contribution to the pyroelectric effect is from the electric field and not tertiary pyroelectric effects. This electric field might seem high, but it is consistent with the value of an electric field used in the Olsen cycle to generate energy from pyroelectricity [54]. Again this is the effective electric field that the MFC experiences, including any induced current from a magnetic flux. When aluminum foil was wrapped around the MFC and RTD, the pyroelectric coefficient decreased back to approximately the same value as the reference pyroelectric coefficient, as depicted in Figure 3.11. These results add validity that either EMI or a temperature gradient contributed to the measured pyroelectric effect. Because the MFC is so thin and small, the temperature gradients within the thermal chamber would have to be enormous to make up for the difference between the generalized and reference pyroelectric coefficient. Therefore, it is likely that the majority, if not all, of the enhancement is coming from the EMI. The effective electric field experienced is an order of magnitude different from each type of MFC. This difference might be due to the P1 and P2 MFCs having different electrode configurations, so the amount of induced current generated from any magnetic flux would vary. In addition, the positioning of the MFCs inside the chamber might slightly vary, which would affect the amount of induced current generated.

There are several Figures of Merit (FOM) that are used for pyroelectric materials such as voltage, current, sensor, and an energy harvesting FOM. The main application for pyroelectricity in

this dissertation is energy harvesting, so the energy harvesting FOM is described as [56]:

$$FOM = \frac{p^2}{\epsilon_{33}} \tag{3.10}$$

This FOM produces an energy density per Kelvin squared. Evidently, the higher the FOM value, the better the material is at energy harvesting, which is the main topic of Chapter 4. These values were graphed in Figure 3.13 with the constant reference pyroelectric coefficient FOM value. The dielectric permittivity used in this equation was the average dielectric permittivity over the temperature interval. This value was $1.483 * 10^{-8} \frac{F}{m}$ and $1.489 * 10^{-8} \frac{F}{m}$ for the P1 and P2 MFC, respectively.

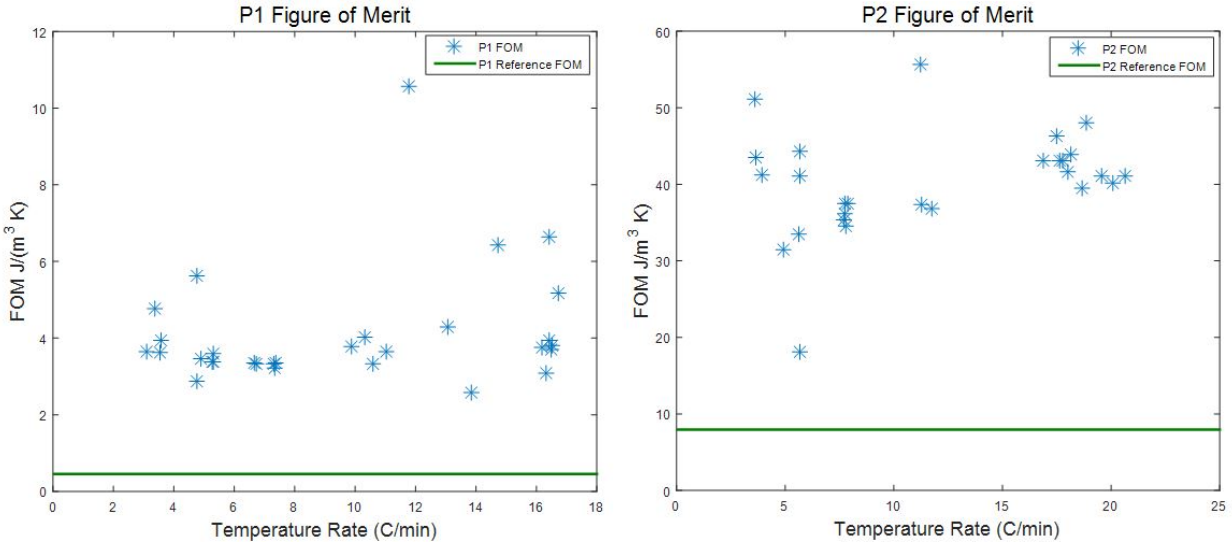

Figure 3.13: The FOM for the P1 MFC (left) and P2 MFC (right) as a function of temperature rate. The reference pyroelectric coefficient at constant stress and electric field is also shown as a constant over various temperature rates.

The FOM shows the MFC energy harvesting capabilities can be enhanced approximately 7 to 11 times greater and 4 to 7 times greater than the reference for the P1 and P2 MFCs, respectively. It is interesting to note that the P1 pyroelectric coefficient was enhanced almost twice as much

as the P2 pyroelectric coefficient. This enhancement could be due to the pyroelectric coefficient of the P1 MFC being so small that there is more opportunity for improvement. Apparently, the higher the pyroelectric coefficient is with respect to its dielectric constant, the better the material performs. Even though the P1 MFC was enhanced almost twice as much as the P2 MFC, the P2 MFC still has a higher FOM value. Therefore, it is still the better candidate for energy harvesting, which will be important for Chapter 4.

3.4 Manipulation of Boundary Conditions

Normally, most pyroelectric materials are classified as ceramic. Because of this, even partially constraining it to limit the amount of thermal expansion experienced by the material can lead to cracks and brittle failure. The MFC is a thin film that can be constrained in the inactive area surrounding the PZT fibers without damage to its functional ability. This has the potential to allow for the boundary conditions of the MFC to be manipulated to observe how that would affect the pyroelectric coefficient. In theory, if the MFC is constrained or in constant strain, only the primary coefficient should generate a pyroelectric effect (ignoring tertiary and electric field effects). It is generally complicated to experimentally verify the primary or secondary coefficient because it is not practical to constrain the specimen completely [2], [57], [58]. However, it may be possible to get a prediction of what the experimental value should be by partially constraining it [59]. Epoxy cannot be used as a means of constraint because it has a CTE higher than the MFC, which should increase the secondary effect. To circumvent this, Kevlar was considered since it has a negative coefficient of thermal expansion [60], and therefore will limit the growth of the MFC.

Two Kevlar sheets were hand sewn with Kevlar string to an M8528-P1 and M8528-P2 MFC

from Smart Materials in the inactive area. This is pictured in Figure 3.14. One sheet was sewn at a time to each face of the MFC, taking great care not to puncture the active area of the MFC or damage the PZT fibers and electrodes. This was accomplished with both P1 and P2 type MFCs.

Figure 3.14: Kevlar sheet sewed with Kevlar string to the MFC.

A different method was also tested where the MFC was epoxied onto a metal shim. In principle, this should increase the expansion experienced by the MFC, undergoing the opposite effect of the Kevlar. The CTE for the epoxy and the metal shim is greater than the CTE for MFCs. The epoxy used was Hysol EA 9394 for decent thermal vacuum properties. After the MFC was epoxied to the metal shim, the sample was placed in a vacuum-sealed bag for at least six hours to remove any air bubbles between the layers. The MFC was allowed to fully cure for the next five days before usage.

Both of the Kevlar sewn samples and the epoxied MFC were mounted in the Michigan thermal chamber with a previously calibrated RTD. Kevlar was wrapped around the RTD to best mimic the thermal environment of the MFCs for about half of the experimental trials. Everything was suspended to be as close to the center of the chamber as possible to avoid thermal gradients through

contact with the metallic surfaces of the chamber. Binder clips were attached to the bottom of the Kevlar sewn MFCs to prevent it from buckling outwards (later data was taken with and without the binder clips, and no difference was seen). The wires were taped down to help prevent vibrations and were attached to a feedthrough. A setup is pictured in Figure 3.15.

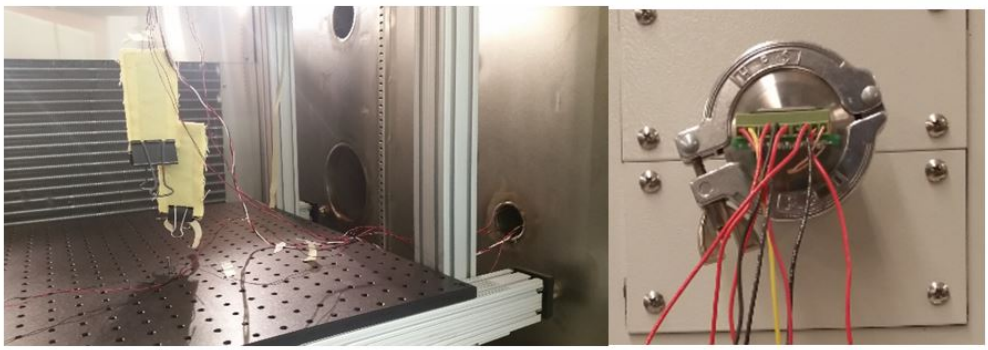

Figure 3.15: (Left) Kevlar sewn MFCs suspended in the chamber with binder clips and an RTD as close as possible to the MFCs. The Epoxied MFC is not shown in this picture. (Right) The wires are attached to a feedthrough in the chamber.

Much of the setup for this experiment mimics the setup for the thermal cycling experiments stated earlier. The thermal cycles were done at a rate of 5 and 10°C per minute. Two temperature rates were chosen to observe if the pyroelectric coefficient would change with temperature rate when the boundary conditions were changed. As previously observed, the pyroelectric coefficient does not vary much with temperature rate for the unaltered MFC.

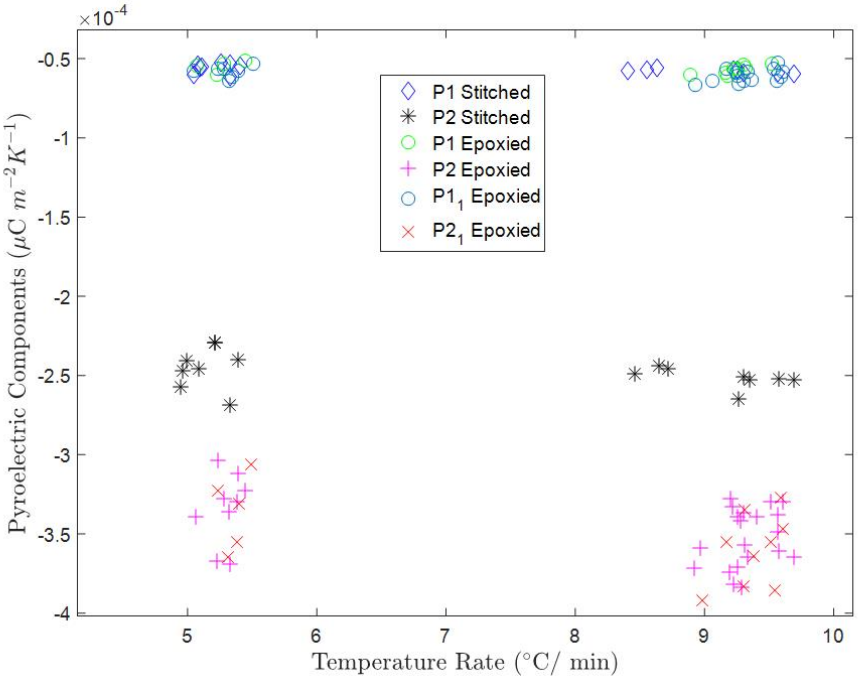

Figure 3.16: The pyroelectric coefficient resulting from the multiple trials conducted on the constrained and epoxied P1 and P2 MFCs.

The results were analyzed using Eq. 3.8. The data from all of the stitched and epoxied trials can be viewed in Figure 3.16. The constrained and epoxied P1 MFCs had similar pyroelectric coefficients where the absolute value of both decreased from the unconstrained MFC pyroelectric coefficient value as noted earlier. The constrained and epoxied P2 MFCs had different results. The constrained P2 MFC absolute pyroelectric coefficient decreased from the unconstrained P2 pyroelectric coefficient by approximately 70 to 100 $\frac{\mu C}{m^2 K}$. The epoxied P2 MFC had interesting results as the absolute pyroelectric coefficient initially increased from the unconstrained P2 pyroelectric coefficient (343 $\frac{\mu C}{m^2 K}$) to almost 400 $\frac{\mu C}{m^2 K}$. As multiple trials were conducted with the same MFC, the absolute pyroelectric coefficient decreased towards and beyond the unconstrained P2 MFC pyroelectric coefficient value. These results were confirmed with another epoxied MFC on the same

material, and the same experiment was completed multiple times. The same trend followed. An average of all the trials is displayed in Table 3.5. (Note: These pyroelectric coefficients are still negative with the negative sign appearing in the units as before.)

Table 3.5: Average Stitched and Epoxied Pyroelectric Coefficient Values and Standard Deviation

Temperature Rate		**Stitched MFC** ($\frac{-\mu C}{m^2 K}$)		**Epoxied MFC** ($\frac{-\mu C}{m^2 K}$)	
Desired (°C/min)	Experimental (°C/min)	P1	P2	P1	P2
5	5.22 ± 0.15	55.81 ± 3.29	244.88 ± 13.64	57.0 ± 3.95	334.63 ± 21.04
10	9.22 ± 0.34	57.71 ± 1.26	251.48 ± 6.45	58.98 ± 3.91	355.19 ± 19.77
	Overall Average	56.76 ± 2.60	248.18 ± 10.86	58.57 ± 4.13	348.18 ± 22.27

For the Kevlar experiment, the results from the experiment should approach the primary coefficient theoretically. The constrained P2 MFC did follow this trend. However, the constrained P1 MFC pyroelectric coefficient is approximately equal to the epoxied P1 MFC coefficient instead of increasing towards the absolute value of the primary coefficient. The epoxied and constrained MFCs should have opposite contributions to the pyroelectric effect. This contrary result indicates that any changes to the boundary of the P1 MFC actually hinders the pyroelectric effect (seems to increase the positive secondary effect). The P1 MFC, in general, does not produce enough current to charge a battery via the piezoelectric effect [61]. A possible explanation for the discrepancy can be due to the primary d_{33} effect of the P1 MFC lying in the plane of restriction, so putting the Kevlar around the P1 MFC especially hindered its current generation and flow.

Epoxy should have the effect of increasing the secondary contribution. Because the modeled secondary effect is positive for the P1, the epoxied P1 MFC supports this conjecture since the pyroelectric coefficient decreased. The constrained P2 absolute pyroelectric coefficient did decrease as anticipated because the secondary coefficient is the same sign as the primary and total coefficient

according to the pyroelectric coefficient modeling discussed earlier. The modeled secant-based secondary effect from Chapter 2 was $-221\frac{\mu C}{m^2 K}$. This is in agreement with the hypothesis that the Kevlar would partially constrain the MFC. The Kevlar CTE is only $-2\frac{\mu}{^\circ C}$, which is not enough to halt the expansion of the MFC completely. The out of plane expansion was also not prevented as it was assumed negligible due to plane stress. The epoxied P2 MFC pyroelectric coefficient did increase at first, illustrating that the pyroelectric coefficient can be enhanced to produce more current through the secondary pyroelectric effect. However, the coefficient seemed to stabilize back to the unaltered P2 pyroelectric coefficient after approximately six cycles, probably due to the thermal relaxation of the internal strains and stresses.

3.5 Vacuum Measurements

Both MFCs were also tested in a vacuum chamber at NASA Langley using linear temperature ramping and thermal cycling. However, due to the challenges presented in accurately measuring the coefficient in vacuum, more testing is recommended before a definitive conclusion can be reached. Preliminary results indicate that the pyroelectric coefficient slightly decreased in vacuum for both MFCs. A more detailed explanation on the test setup and the results is found in Appendix B.

3.6 Chapter Summary

The pyroelectric coefficient of two types of MFCs was explored using thermal chambers at NASA Langley and Michigan from 25°C to 70°C at varying linear temperature rates. Thermal

cycling was also conducted in both chambers between $40°$C and $100°$C, which was cycled seven times. The NASA data with TSCs had more variance with a mean and standard deviation of -71 ± 70 and -194 ± $55\frac{\mu C}{m^2K}$ for the P1 and P2 type respectively. After TSCs were subtracted, the mean and standard deviation were -93 ± 17 and -347 ± $12\frac{\mu C}{m^2K}$ for the P1 and P2 type respectively. The Michigan data for linear temperature ramping was not too different at -161 ± 42 and -334 ± $33\frac{\mu C}{m^2K}$ for the P1 and P2 type respectively where the TSCs were not subtracted out. The thermally cycled data had a better precision with a P1 and P2 pyroelectric coefficient of -82 ± 6 and -343 ± $15\frac{\mu C}{m^2K}$ respectively.

The pyroelectric coefficient is dependent on the type of MFC used due to their respective poling directions, and any electric field experienced. Once any electric field is removed through aluminum shielding, and TSCs are subtracted from the total current, both data sets (linear temperature ramping and thermally cycling) of NASA experiments match the thermally cycled Michigan data. The pyroelectric coefficient is consistent between two different chambers and methods indicating that the value measured is the actual value for this test setup.

The pyroelectric coefficients of the P1 and P2 MFCs were measured with an EMI coming from the thermal chamber, and were compared to the reference pyroelectric coefficients at constant electric field and constant stress. The measured pyroelectric coefficient was almost two times greater than the reference coefficient. The FOM shows that the P1 and P2 MFC pyroelectric coefficients were enhanced between 7 to 11 times and 4 to 7 times, respectively. Even though the P1 MFC pyroelectric coefficient was enhanced more, the value of the FOM was higher for the P2 MFC, indicating that the P2 MFC would still make a better energy harvester which will be validated in Chapter 4. This considerable enhancement shows that the energy harvested from the MFC can be significantly increased with any EMI. This is advantageous because, in most applications, EMI is

unwanted, and measures are taken to shield the product from this phenomenon. If pyroelectric energy harvesting was the only application, the pyroelectric material does not necessarily need to be shielded and gets an added boost to energy output without having to expend any extra energy creating an electric field. The use of EMI has the disadvantage of not being able to control the amount of electric field experienced by the material, so if the material has a low dielectric breakdown, this EMI might damage it.

To observe whether the primary coefficient could be isolated experimentally, Kevlar (which has a negative CTE) was sewn with Kevlar string to both sides of the MFC in the inactive area. These constrained MFCs were then thermally cycled, and the resulting pyroelectric coefficient was measured. The constrained P1 and P2 MFC had a coefficient of $-57\frac{\mu C}{m^2K}$ and $-248\frac{\mu C}{m^2K}$ respectively. These values do not agree with the modeled value for the P1 primary coefficient (as this absolute value should be greater than the total P1 coefficient because the secondary coefficient was estimated as a positive value which reduces the overall negative coefficient); however, this is a reasonable estimate for the P2 primary coefficient. The Kevlar may be hindering the generation of current in the P1 MFC due to its geometry. The Kevlar in the P2 MFC would only have partially isolated the primary coefficient. Although the CTE of Kevlar is negative, it is not enough to negate the expansion of the MFC. Additionally, although the Kevlar was stitched together as close as possible without losing the Kapton's structural integrity, there were still noticeable gaps between the stitches. These small gaps would not be constrained.

A metal shim was epoxied on another set of P1 and P2 MFCs. It was anticipated that the epoxy and metal shim would increase the secondary effect because they have a higher CTE than the MFCs. This result may have occurred with the epoxied P1 MFC, but the pyroelectric coefficient was a similar value to the constrained P1 MFC producing inconclusive results. The epoxied

P2 pyroelectric coefficient did increase in value to approximately -390 $\frac{\mu C}{m^2 K}$ at first. After about six trials of thermal cycling, the value decreased back to the standard unaltered P2 pyroelectric coefficient likely due to thermal relaxation of the internal strain and stresses.

In this chapter, the pyroelectric coefficient was experimentally determined and explored through multiple methods. Linear temperature ramping and thermal cycling were used to verify the pyroelectric coefficient against the results in Chapter 2. The pyroelectric coefficient was also enhanced using an unexpected EMI from one of the chambers used at NASA, and a FOM was established for energy harvesting which shows that the P2 MFC should be better for this application (explored in Chapter 4). The pyroelectric coefficient was also investigated under different boundary conditions, where Kevlar was sewn to the edges of the MFCs to restrict the in-plane movement, and the MFCs were epoxied to an aluminum shim to encourage in-plane movement. This was done in the hopes of verifying the pyroelectric coefficient components (i.e., primary and secondary coefficients). Vacuum data on the pyroelectric coefficient was also measured in MFCs but due to the many issues present, more testing is recommended before any concrete conclusion can be inferred.

This research improves the understanding of the pyroelectric effect in MFCs and provides a means of experimentally obtaining a lower bound for thin films for the primary and secondary pyroelectric coefficient if the total coefficient is known.

CHAPTER 4

Potential Pyroelectric Applications

Traditional applications for pyroelectric materials have included pyroelectric infrared detectors or temperature sensors. In this dissertation, the focus of the pyroelectric application will be using it for energy harvesting. Waste energy harvesting is becoming more popular for low power devices because of the ability to harvest energy from sources such as vibrations, temperature changes, or temperature gradients that might be present in various ambient environments. Because the energy sources can be detected by small devices, the size and cost are much less than the devices and structures needed to harvest energy from other sources such as wind or hydroelectric energy.

There are three applications involving energy harvesting that this chapter will cover. The first is pure pyroelectric energy harvesting, which is modeled, verified experimentally, and optimized for the maximum energy by changing the resistance. The next two applications are ways that pyroelectric energy harvesting can be incorporated into existing schemes and are mainly as a proof of concept. These applications are combined piezoelectric and pyroelectric energy harvesting, and pyroelectric energy harvesting combined with structural health monitoring (SHM).

4.1 Pyroelectric Energy Harvesting

Now that the pyroelectric coefficient has extensively been investigated, it can be used to predict the amount of energy generated through the pyroelectric effect. The energy modeled can then be compared to an experiment and used to determine if even a simplified model would successfully predict the experimental energy harvested. This model can then be used in real-life applications to determine the size and temperature change necessary to harvest a specific amount of energy to help contribute power to a system.

4.1.1 Modeling the Energy Harvested

The pyroelectric energy harvested was modeled using several methods to estimate the desired temperature profile. These include a numerical method in which the experimental temperature profile was supplied, an analytical sum of sines curve fit, and a generic sine wave. A representation of the circuit used for energy harvesting is shown in Figure 4.1.

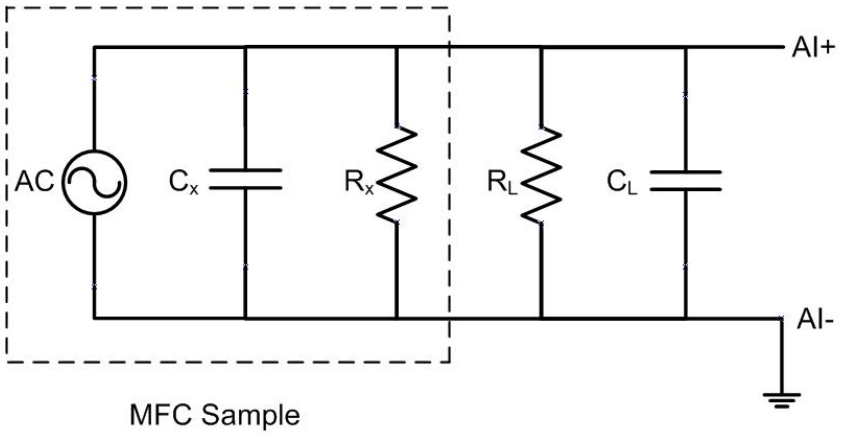

Figure 4.1: The pyroelectric energy harvesting circuit with the Macro-fiber Composite (MFC) shown in parallel with an external load resistance and capacitor.

Figure 4.1 shows the pyroelectric material in parallel with an external capacitor, C_L and external resistor, R_L. The pyroelectric material can be represented as a current source, I_p, internal resistor, R_x, and internal capacitor, C_x ([6]). This makes the total resistance equal to

$$R = \frac{R_x R_L}{R_x + R_L} \tag{4.1}$$

since the resistances are in parallel with each other. If $R_L << R_x$, then the total resistance is estimated to be the load resistance. The total capacitance is the sum of the internal and external capacitors since they are also parallel to each other:

$$C = C_x + C_L \tag{4.2}$$

The current source of the pyroelectric element can be described by Eq. 3.2 in Chapter 3. The currents can be added in the circuit, so a relationship between voltage and temperature can be found. Using Kirchhoff's Current Law with nodal analysis of the circuit, the sum of the currents is:

$$pA\frac{dT}{dt} = \frac{V}{R} + C\frac{dV}{dt} \tag{4.3}$$

where the pyroelectric element current is taken from Eq. 3.2, and R and C are taken from Eq. 4.1 and Eq. 4.2 respectively. Note that the current going through the resistor and capacitor is negative, but the pyroelectric coefficient is negative, so this becomes a double negative, or positive value. To solve for the transfer function, Eq. 4.3 must be converted from the time domain to the Laplace domain. It then becomes:

$$pAs\,(T - T_0) = \frac{V}{R} + Cs\,(V - V_0) \tag{4.4}$$

The initial temperature is a non-zero value, whereas the initial voltage is assumed zero. The initial temperature is subtracted from the temperature array and is denoted Δ. After rearranging Eq. 4.4, the transfer function that relates voltage to temperature is:

$$\frac{V}{\Delta} = \frac{pAs}{\frac{1}{R} + Cs} \tag{4.5}$$

Because most temperature profiles are in the time domain, the temperature also needs to be converted to the Laplace domain. Two temperature profiles were chosen, one at 5°C per minute, and the other at 10°C per minute, which is shown in Figure 4.2. This numerical data was used to estimate the voltage.

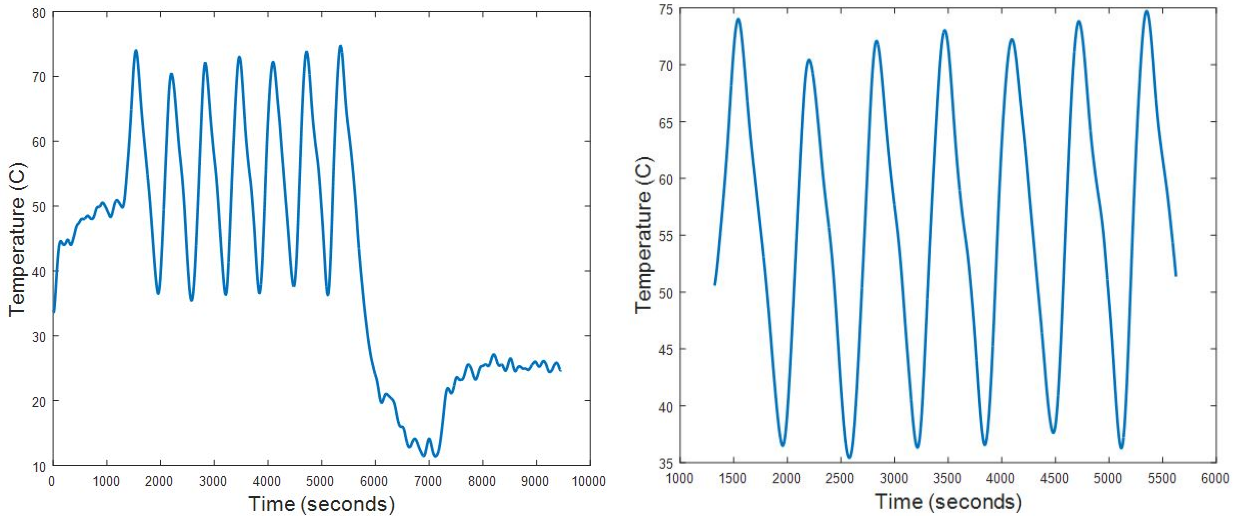

Figure 4.2: The complete experimental temperature profile (left) with the actual temperature profile used for modeling shown on the right. The beginning and end were trimmed from the data set to mimic a sinusoidal wave better.

The second modeling method was analytically estimating the experimental data with a sum of

sines in the time domain, *t*, where *i* is an index from 1 to 6:

$$T(t) = \sum_{i=1}^{6} a_i sin(b_i t + c_i) \tag{4.6}$$

The values of *a*, *b*, and *c* are given in Table 4.1.

Table 4.1: Values for the higher order sine approximation.

Temperature Rate (°C/min)	**Parameter**	**Index Values**					
		1	**2**	**3**	**4**	**5**	**6**
5	a	3.286	376.5	16	183.1	4.433	24.93
	b	5.28e-3	1.152e-4	4.922e-3	3.24e-4	9.949e-3	6.621e-4
	c	6.694e-3	2.371	-3.806	4.134	4.377	5.038
10	a	2.277	239.3	152.5	14.5	22.5	3.625
	b	1.068e-2	3.066e-4	6.721e-4	9.861e-3	1.314e-3	1.991e-2
	c	-4.655	1.953	3.723	-1.46	4.427	2.82

The same curve fit was performed for a generic sine function that matches closely with the $5°$C per minute and $10°$C per minute temperature profiles as described respectively:

$$\begin{aligned} T(t) =& 21 sin(0.00475t - 2.59) \\ T(t) =& 18 sin(0.00989t - 1) \end{aligned} \tag{4.7}$$

A comparison of all the resulting temperature profiles is shown in Figure 4.3.

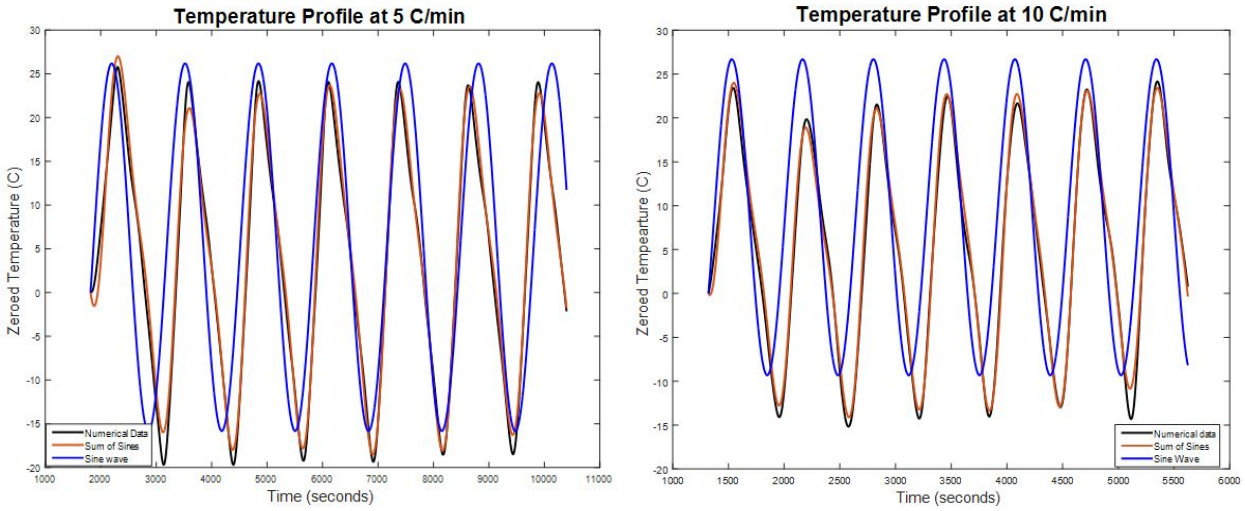

Figure 4.3: The three different temperature profiles at $5°$C per minute and $10°$C per minute are based on experimental data where the black line represents the numerical profile, the red line represents the sum of sines, and the blue line represents the sine wave model. The temperature was zeroed so that the initial temperature starts at $0°$C.

The numerical temperature profile was taken from an experimental temperature profile at the specified temperature rate. The sum of sines match closely with the numerical temperature profile as expected since it is of a higher order analytical function. The sine wave has the most deviation from the numerical temperature profile as the peaks are slightly shifted and have greater magnitude.

4.1.2 Experimental Energy Harvesting

The experimental data is taken from all the previous experiments that have been conducted in estimating the pyroelectric coefficient in Chapter 3. Therefore, the experimental setup is the same where either a 28 x 14 mm or an 85 x 28 mm active area P1 or P2 Macro-fiber Composite (MFC), acquired from Smart Material Inc., was suspended inside a thermal chamber with a resistive temperature device (RTD) and connected to a data acquisition device (DAQ). There was a 10 MΩ resistor connected in parallel with the MFC. Later, the resistance was varied to compare with

this model. There was no external capacitance connected to the circuit. Some of the experiments included have the MFC connected to a relay circuit that switches between taking voltage measurements and taking impedance measurements for SHM, which is described in detail in Section 4.2.2.

The DAQ collected the voltage generated by the MFC as a function of time. After filtering the data, this voltage was converted to power where the shunt resistor is the total resistance since the resistance of the MFC ($R_x > \text{G}\Omega$) is much greater than the shunt resistor used (Eq. 4.1). This power was transformed into energy using numerical integration (trapezoidal rule).

4.1.3 Results and Discussion

To calculate the voltage response of the transfer function using the different temperature profiles, the average capacitance of the MFCs is needed and measured with a capacitance meter. The capacitance values are given in Table 4.2.

Table 4.2: Average Capacitance of the MFCs

	P1 28 x 14 mm	P1 85 x 28 mm	P2 28 x 14 mm	P2 85 x 28 mm
Capacitance (nF)	1.01	6.55	30.30	180.95

Using the resistance and area values discussed earlier, as well as the capacitance and pyroelectric coefficient of 82.2 and $343\frac{\mu C}{m^2 K}$ for the P1 and P2 MFCs respectively (positive due to the double negative with the transfer function), the voltage response can be analyzed. The numerical temperature profile and the transfer function were analyzed in MATLAB using a simulated time response function. The sum of sines (Eq. 4.6) and the sine wave (Eq.4.7) temperature profiles were converted to the Laplace domain by hand and then multiplied with the transfer function as seen in

Eq. 4.8 where the sum of sines is just an expansion on this equation.

$$V = \frac{pAsa}{\frac{1}{R} + Cs}\left(\frac{ssin(c) + bcos(c)}{s^2 + b^2}\right) \tag{4.8}$$

This equation represents the voltage response in the Laplace domain. Variables a, b, and c represent the amplitude, period, and phase shift of the sine wave. The sum of sines would just be a summation of this equation for each of the different indices listed in Table 4.1. Eq. 4.8 was then converted back to the time domain, as seen below:

$$\begin{aligned} V = \frac{pAa}{C(1 + R^2b^2C^2)}\Big[&sin(c)\left(e^{\frac{-t}{RC}} + b^2C^2R^2cos(bt) - bCRsin(bt)\right) \\ &+bcos(c)RC\left(-e^{\frac{-t}{RC}} + cos(bt) + bCRsin(bt)\right)\Big] \end{aligned} \tag{4.9}$$

Again, the sum of sines would just be a summation of Eq. 4.9 over the different indices. A comparison of the voltage response as a function of time for the different temperature profiles is depicted in Figure 4.4. The general shape of the voltage response was the same for both types of MFC for the same temperature rate. The values for the voltage were the only differences observed; hence a representative graph was chosen for each temperature rate.

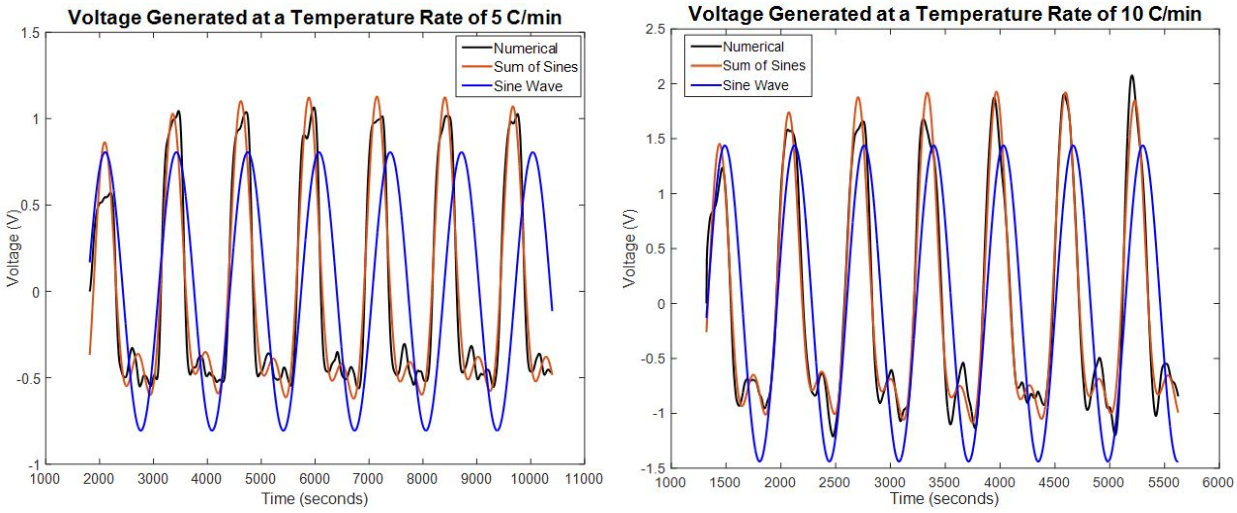

Figure 4.4: The voltage generated as a function of time for the different temperature profiles at $5°$ C per minute and $10°$ C per minute for the P2 85 x 28 mm MFC.

As with the temperature profiles in Figure 4.3, the numerical and the sum of sines profiles in Figure 4.4 match closely with each other. There is a slight increase in the sum of sines peak compared to the numerical profile, and there is a peak shift in the trough of the wave. The generic sine wave is shifted lower, making the extrema have a lower value. As time progresses, the sine wave also becomes out of phase with the other two profiles, which is less noticeable at a temperature rate of $10°$ C per minute.

An average energy and standard deviation were calculated for each temperature rate and MFC. Alongside an average, the modeled energies are also displayed in Table 4.3 for the $5°$C per minute temperature rate and Table 4.4 for the $10°$C per minute temperature rate. The percent deviation from the experimental value is also given in parenthesis.

Table 4.3: Energy Generated and Percent Deviation at 5° C per minute

MFC Active Area	Method at 5° C/min	P1 MFC Energy (μJ)	P2 MFC Energy (μJ)
28 x 14 mm	Experimental	0.46 ± 0.033	7.85 ± 0.333
	Numerical	0.47 (1.77%)	8.22 (4.81%)
	Sum of Sines	0.45 (3.86%)	7.77 (0.99%)
	Sine Wave	0.44 (5.27%)	7.65 (2.44%)
85 x 28 mm	Experimental	17.6 ± 0.633	330 ± 8.25
	Numerical	17.4 (0.98%)	303 (8.15%)
	Sum of Sines	16.4 (6.46%)	286 (13.2%)
	Sine Wave	16.2 (7.83%)	282 (14.5%)

Table 4.4: Energy Generated and Percent Deviation at 10° C per minute

MFC Active Area	Method at 10°C/min	P1 MFC Energy (μJ)	P2 MFC Energy (μJ)
28 x 14 mm	Experimental	0.73 ± 0.036	11.9 ± 0.537
	Numerical	0.68 (6.81%)	11.8 (0.74%)
	Sum of Sines	0.66 (9.31%)	11.5 (3.41%)
	Sine Wave	0.70 (3.57%)	12.2 (2.69%)
85 x 28 mm	Experimental	23.6 ± 0.374	459 ± 17.0
	Numerical	25.0 (5.64%)	434 (5.47%)
	Sum of Sines	24.3 (2.79%)	423 (7.99%)
	Sine Wave	25.8 (9.30%)	449 (2.21%)

As shown in the tables, the amount of energy harvested was in the μJ range. The energy harvested increased with the size of the active area. The amount of energy produced by the 28 x 14 mm P2 MFC was slightly less than the energy produced by the 85 x 28 mm P1 MFC even though the P1 MFC had a bigger area. This reinforces the idea that the P1 MFC does not generate energy as well as the P2 MFC, especially when comparing the same size MFCs with each other. Between the two temperature rates, more energy was generated with the faster temperature rate. The amount of energy increased between 34% to 59% from doubling the temperature rate. This increase was expected since the current generated is proportional to the temperature rate, where the pyroelectric coefficient is the proportionality constant between the current and temperature rate normalized by

the area.

Overall, the numerical method had the least percent deviation, considering all the cases (the percent deviation did not exceed 8.15%), as expected since the numerical temperature profile was taken from an experimental data set. The sum of sines method performed better than the sine wave method in Table 4.3, but for most of the cases in Table 4.4, the sine wave method performed better. This is probably due to the sine wave temperature profile matching the average experimental data better than the one experimental data chosen of which the sum of sines temperature profile was fitted to. Overall, however, the percent deviations in Table 4.3 and Table 4.4 are less than 15% and 10%, respectively from the average experimental value. These results illustrate that if the experimental temperature profile is not quite oscillating harmonically, the energy harvested is still able to be approximated with relative accuracy with a fitted sine wave. For slightly more accuracy in most cases, a sum of sines approximation can be utilized. However, the advantages over the sine wave are only marginal as it requires more time to approximate.

The maximum specific power (or surface power density) was also investigated by finding the maximum power within the data range specified and then normalizing it by the active area of the MFC. The graphs of the specific power utilizing the different methods with a temperature rate of $5°$C per minute and $10°$C per minute are depicted in Figure 4.5 and Figure 4.6, respectively.

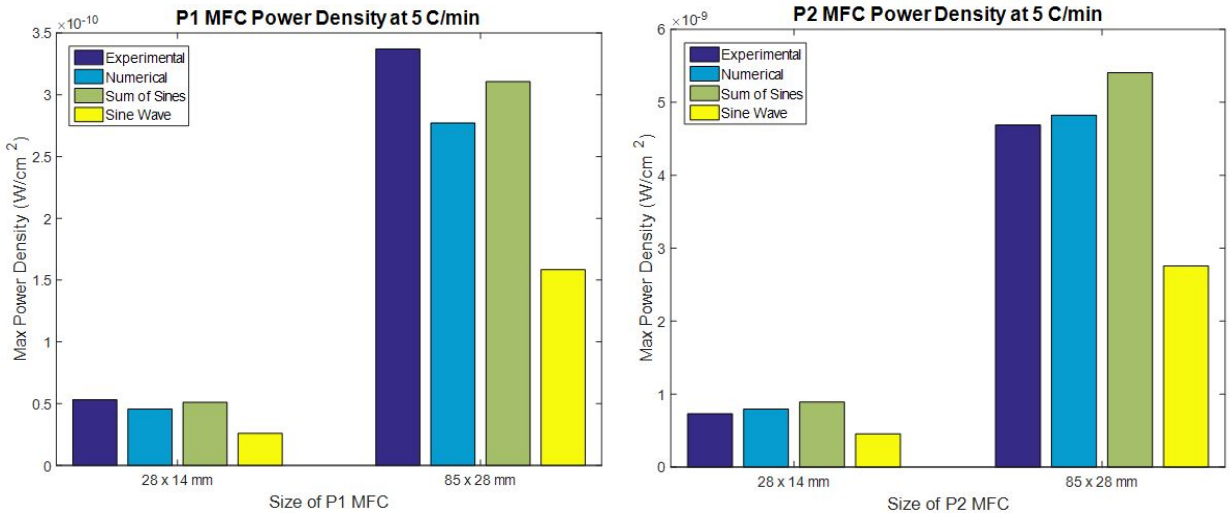

Figure 4.5: The maximum specific power of the MFCs at a temperature rate of $5°$C per minute for the different experimental and modeled data.

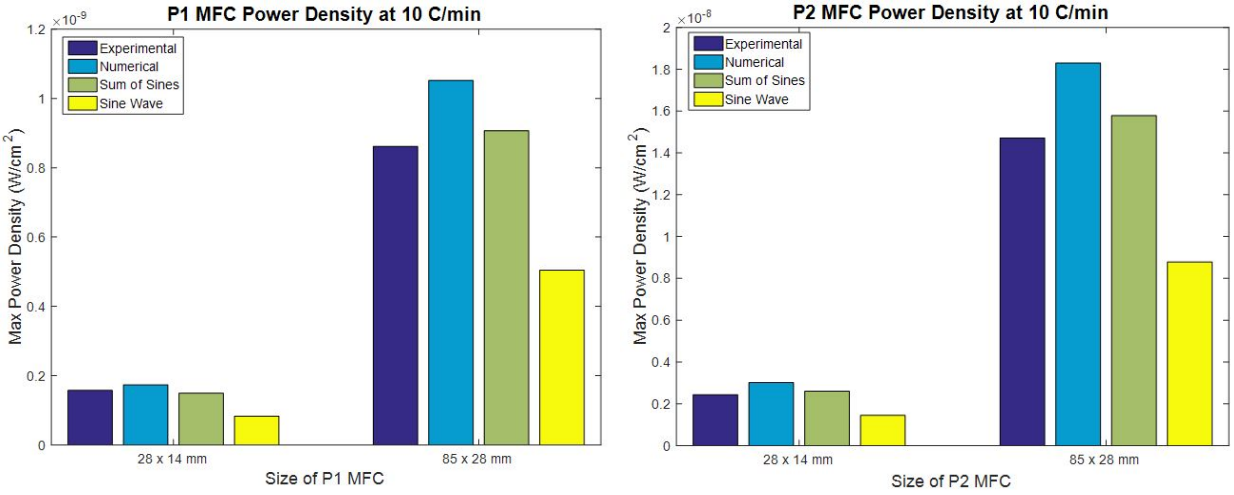

Figure 4.6: The maximum specific power of the MFCs at a temperature rate of $10°$C per minute for the different experimental and modeled data.

As with the energy generated, the maximum specific power is greater with a bigger MFC, and when the P2 MFC is utilized. There is an order of magnitude difference for the maximum specific power between the different sizes of the same type of MFC and another order of magnitude difference between the same size P1 and P2 MFCs.

A point of interest is that the bar graph's general shape is the same for a type of MFC at a specific temperature rate, probably due to using the same temperature profile for both MFC sizes. Expanding on this, the general distribution of the bars in Figure 4.6 is almost identical, with the P2 MFC having slightly more variations between the different methods. However, in Figure 4.5, the numerical and the sum of sines methods for the P2 MFC over predict the experimental value. This over prediction is most likely caused by the average experimental data being lower than predicted instead of the temperature profile not fitting the average experimental temperature profile, as was stated earlier for the energy harvesting. If the temperature profiles were the dominant cause for the discrepancy between the experimental and modeling results, it would be reasonable that both graphs would also have the same distribution as in Figure 4.6.

Except for the P2 MFC in Figure 4.5, the sum of sines method is closest to the experimental value, unlike the energy harvesting results. This discrepancy might be due to the voltage response for the sum of sines having a slightly larger value and more consistent voltage peak values, in general, than the numerical voltage response. Unlike the energy harvesting results, the sine wave was consistently the worst predictor of specific power. The sine wave temperature profile has a lower amplitude that causes the voltage response also to have a lower value, which would affect the maximum power generated through this model. Therefore, it is recommended that if the maximum power parameter is modeled to use a higher order function for the temperature profile.

4.1.4 Energy Harvested as a Function of Resistance

Once the models were established, and it was determined that the numerical model was generally the best predictor of the energy harvested, a resistance sweep was conducted to find the

optimum resistance without an external capacitor that would generate the most energy. Resistor values from 1000 Ω to 10 TΩ were given as inputs into the numerical model, and the energy was stored and displayed in Figure 4.7 for both temperature rates.

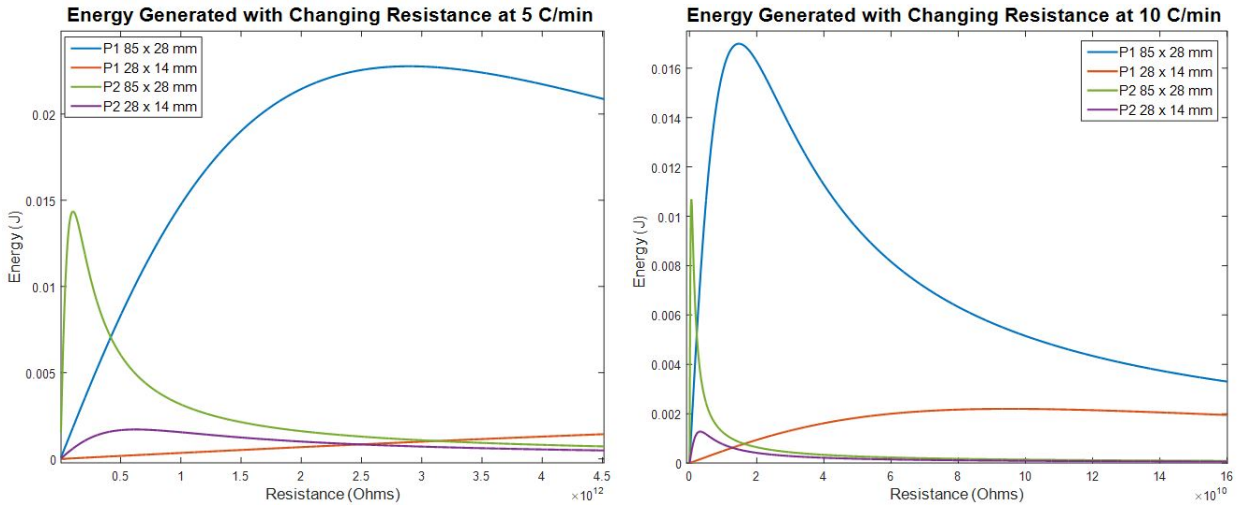

Figure 4.7: The energy generated over multiple resistances for the different sized MFCs at a temperature rate of 5°C per minute and 10°C per minute.

The energy generated by changing the resistance increased to the mJ range instead of the μJ range as it was earlier with a 10 MΩ resistor. Unfortunately, the resistor required for this energy is unreasonably large, in the GΩ to TΩ range. The resistor required to achieve the peak energy does decrease with increasing temperature rate. It may be possible for fast temperature changes where the degrees change in seconds instead of on the order of minutes, such as in a car or running hot water through a cold pipe, to have a reasonable resistor value. Another difference between the two temperature rates is that the higher temperature rate can harvest slightly less energy at its optimum resistance than the lower temperature rate. Consequently, there is a trade-off between maximum energy harvesting, time, and resistor value. The resistor that would achieve the maximum power density would likely be much lower, in the high MΩ to GΩ range as it should match the impedance

of the MFC at a given frequency (in the case for these temperature profiles 0.001 Hz). Matching the external impedance (or resistor) to the internal impedance of the system allows the maximum amount of current to flow which should generate the maximum power. To give an example, the P2 85 x 28 mm active area MFC has a capacitance of 180.95 nF from Table 4.2. The frequency, *f*, of the temperature cycles was approximately 0.0008 Hz at 5°C per minute and 0.0016 Hz at 10°C per minute. To calculate the value of the resistor that would yield the maximum power, the impedance should be matched to the resistance as shown [62]:

$$Z_{total} = R_L \cong \frac{1}{2\pi f C} \tag{4.10}$$

According to Eq. 4.10, the resistance that will yield the most power is 1.1 GΩ at 5°C per minute and 550 MΩ at 10°C per minute. These values are verified by doing a resistance sweep for the maximum power as shown in Figure 4.8.

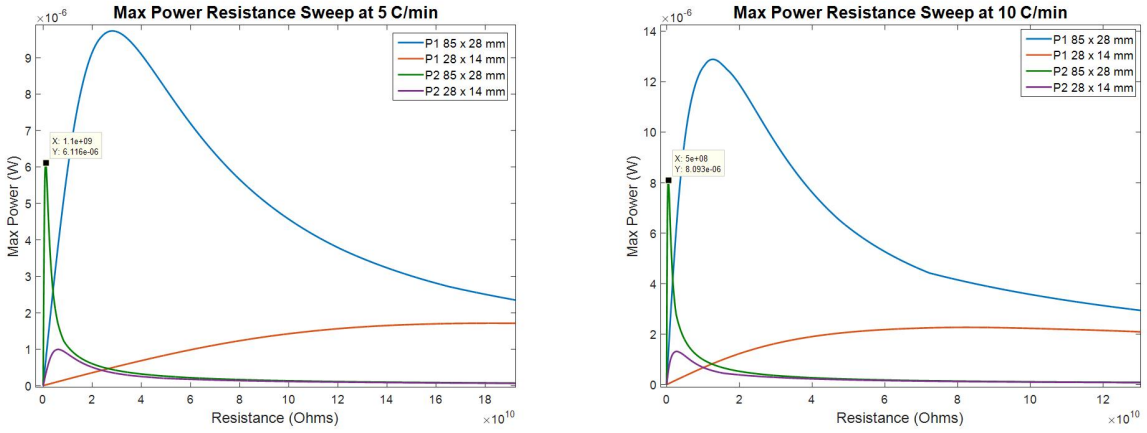

Figure 4.8: The maximum power over multiple resistances at 5°C per minute and 10°C per minute with a data point showing the resistance needed for the maximum power generated by the P2 85 x 28 mm active area MFC.

The values predicted by Eq. 4.10 match well with Figure 4.8. The resistances required for

the maximum power were lower than for the maximum energy. Because the energy is the area of the power with time, the maximum energy harvested will be at a different resistance than the maximum power.

The energy values predicted at different resistances were validated with experiments using the same setup except with different resistors. A breadboard was used to accommodate the number of resistors put in series. The resistance range tested was between 2200 Ω and 98 MΩ. The number of resistors needed and the current laboratory resources limited the maximum resistance value tested. In addition, the DAQ could only read up to 10 V. Larger resistances would increase the voltage generated, sometimes saturating the channel, which was especially true on the P2 85 x 28 mm MFC and therefore the maximum resistance tested for that MFC was 20 MΩ. The results of the experiments are compared with the model and are depicted in Figure 4.9. The two cases with the most variance in resistance and the most experimental trials conducted were chosen to validate the model.

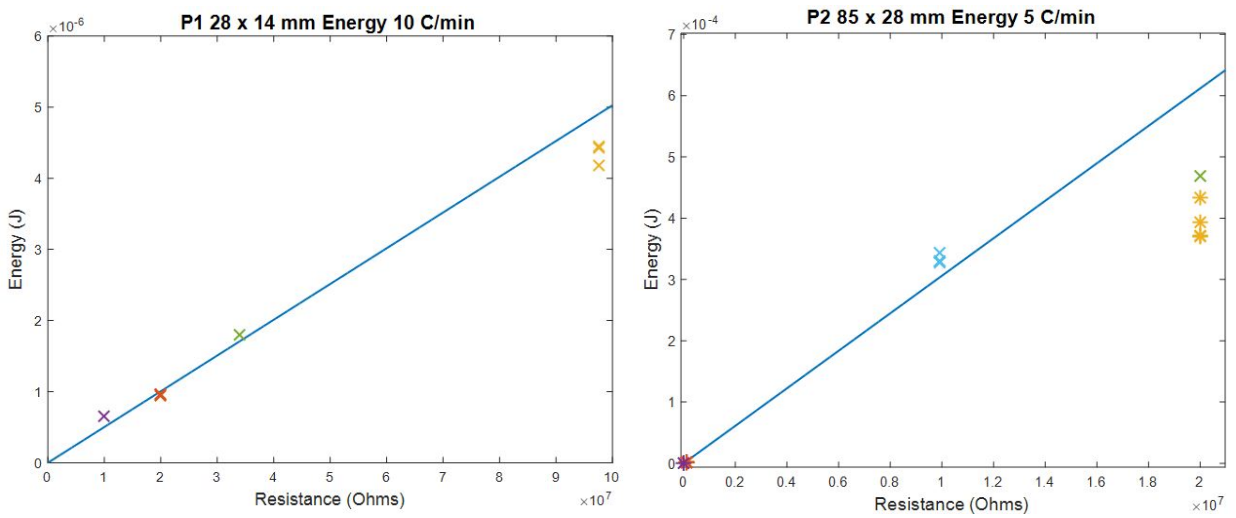

Figure 4.9: The energy generated through experiments and modeling over multiple resistances for the P1 28 x 14 mm MFC and P2 85 x 28 mm MFC at a temperature rate 10°C per minute and 5°C per minute, respectively.

The range of resistance values in Figure 4.9 was decreased to reflect the maximum resistance tested experimentally (98 MΩ for the P1 and 20 MΩ for the P2). The experimental energy values fit the model except for the experiments denoted by the stars at 20 MΩ for the P2. These experiments were conducted after the thermal chamber underwent repairs for a coolant leak. Even though everything in the experiment and programming remained the same, the temperature profile changed after the repairs and became slower. A new temperature profile was analyzed and used to model the energy numerically, as shown in Figure 4.10, along with the old numerical model. Figure 4.10 is composed of two graphs, where the one on the right is a close up of the area denoted by a black box near the origin of the left graph.

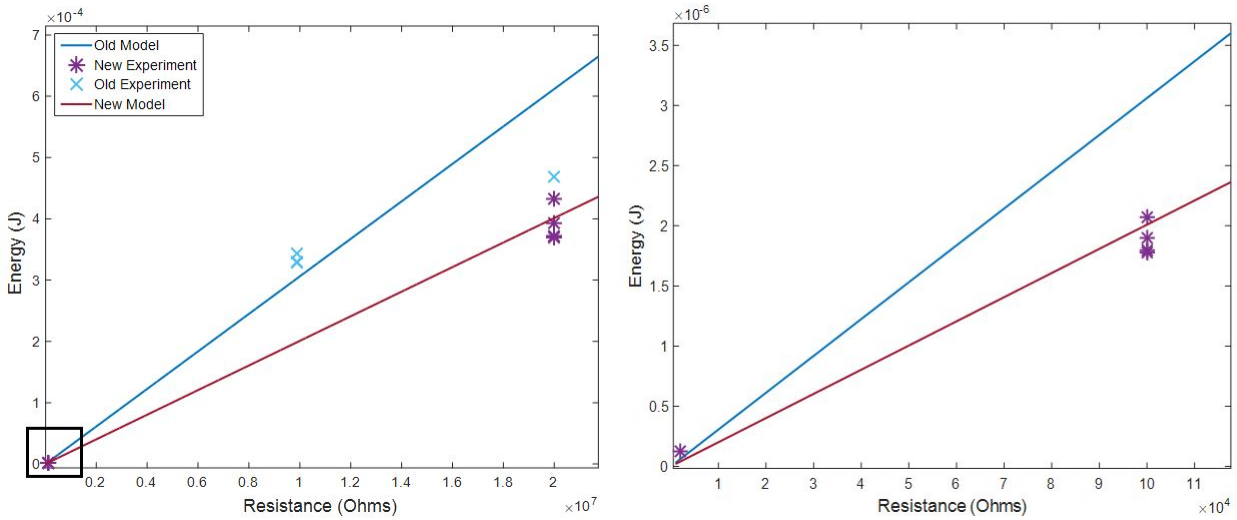

Figure 4.10: The energy generated through experiments and modeling over multiple resistances for the P2 85 x 28 mm MFC at a temperature rate of 5°C per minute with the new numerical model using the updated temperature profile. The black box near the origin on the left plot represents the area that is depicted in the graph on the right.

The new model with the updated temperature profile corresponds well to the new experiments, even over a vast resistance range (2200 Ω to 20 MΩ, 10 MΩ to 98 MΩ). These results illustrate that as long as the real world temperature profile and circuit are known, a model can be developed

to predict the energy harvested, and predict the optimal resistor that will allow for the most energy generation.

4.2 Proof of Concept Applications

This section will detail a few proofs of concept ideas that were not optimized or explored further than just validating the idea either due to time constraints due to Covid-19 or the details of perfecting the experiment were out of the scope of this dissertation. The first application combines the piezoelectric and pyroelectric effect for energy harvesting, which will generate more energy from a single MFC. The second application is using SHM to monitor for damage and also using the pyroelectric effect for energy harvesting during the downtime. If there are vibrations present, this can also combine the piezoelectric and pyroelectric effects for more energy when not SHM. These applications can be used anywhere that either has a combination of vibrations and thermal fluctuations such as in an aircraft, or requires damage monitoring where there are also thermal variations and maybe vibrations such as in concrete or pipes.

4.2.1 Combined Piezoelectric and Pyroelectric Energy Harvesting

Zakharov et al. [23] showed that combined piezoelectric and pyroelectric energy harvesting is possible by bonding an MFC to a shape memory alloy (SMA) and applying a temperature change. To further explore the possibility of simultaneously harvesting both thermal fluctuations and ambient vibration, an experiment was conducted to combine harvesting vibration through the piezoelectric effect with harvesting thermal energy with the pyroelectric effect. The objective is to provide a proof of concept that simultaneous harvesting is possible using just MFCs (no SMA as in the case

provided in [23]).

4.2.1.1 Experimental Setup

In order to prove this concept, both a vibration source and a varying thermal source is required. Thus, some sort of mechanical excitation was needed that would fit into the thermal chamber. A P2 28 x 14 mm active area MFC was bonded to a 19 x 139.7 x 2.43 mm aluminum beam and was then placed in a clamp, which was tightened using screws. The clamp was placed on 8020 to secure it to the optical work surface. For the vibrations, a cell phone vibration motor was de-soldered from a used phone, as seen in Figure 4.11, using a heat gun.

Figure 4.11: A close up of the cell phone motor still soldered to the Motorola phone.

Wires were attached to the motor, and the motor was supplied power to test if it was operational. After verifying it still performed as intended, the motor was bonded to the same aluminum beam via epoxy. A clip was used to secure the motor in place while the epoxy cured, as seen in Figure 4.12.

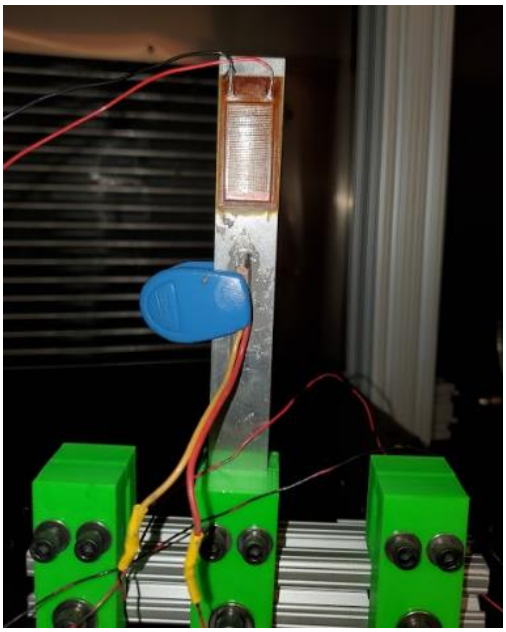

Figure 4.12: A photo of the motor epoxied onto the aluminum beam with a clip (blue) holding it in place while the epoxy is allowed to cure.

This setup, as seen in Figure 4.13, was placed inside the thermal chamber where all the experiments were conducted to prevent any environmental bias. The motor and MFC were facing the back of the chamber in order to minimize the temperature lag between the air and the MFC. The clamp was bolted down to the optic table within the thermal chamber to secure it. An RTD was placed as close to the MFC as possible to measure the temperature the MFC is experiencing. It was not bonded to the beam or MFC to prevent any resulting vibration damping that might occur.

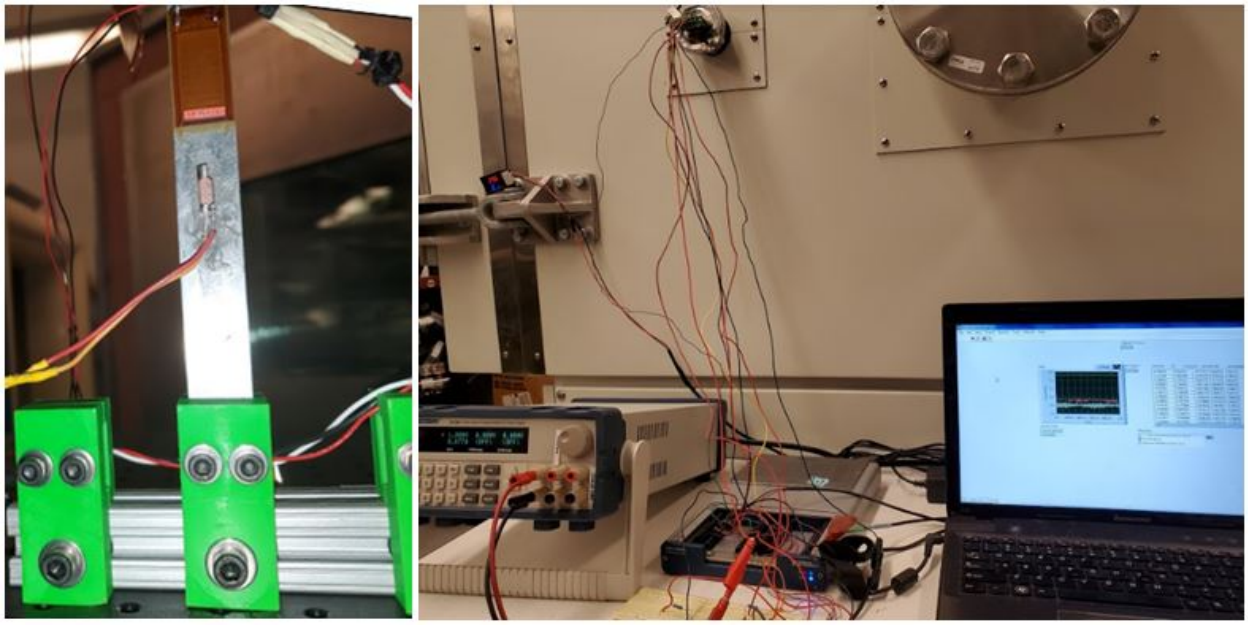

Figure 4.13: (left) A photo of the setup with the motor epoxied onto the aluminum beam, the beam clamped with screws, and the clamp screwed into the optics table to secure it. (right) The outside of the chamber showing the power supply, DAQ, and laptop collecting the data.

Three experiments were conducted, one with just vibrations, one with just a thermal load, and one with both to observe the differences in the energy generated in each case. In all cases the sampling rate was limited to 100 Hz to prevent overloading the DAQ memory as it would have to store approximately 1.75 hours of data.

1. Vibration Harvesting

The motor was supplied 1 V from a power supply. The amount of rotations per minute (RPM) scales with the voltage; however, if a higher voltage was applied, the temperature of the motor increased. Because the motor would already experience a temperature load, the voltage was kept to a minimum to prevent the motor from overheating. The chamber was closed, and the LabView VI was run for the same amount of time as the other tests to simulate the same testing conditions. A 100 kΩ resistor connected in parallel with the MFC was used in all tests.

2. Thermal Harvesting

The power supply to the motor was turned off. The chamber was programmed to run at $10°C$ per minute for seven cycles between $30°C$ and $70°C$ (the recommended maximum temperature for the motor). At the beginning of the temperature ramp, the temperature was held at $30°C$ for 10 minutes, and at the end of the test, it was held at $20°C$ for 10 minutes to delineate when the cycles started and stopped. The actual temperature profile recorded by the RTD is shown in Figure 4.14. The actual temperature where the RTD and MFC were located only reached just under $50°C$.

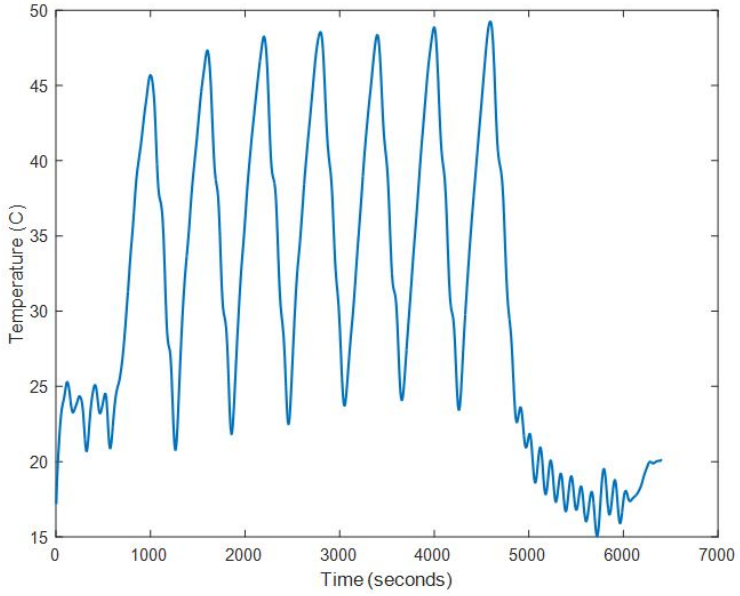

Figure 4.14: The RTD temperature profile vs time going from room temperature to approximately $47°C$.

3. Simultaneous Vibration and Thermal Harvesting

To validate the concept of simultaneous vibration and thermal harvesting, both the power supply and the chamber were turned on using the same parameters described in the previous sections. The power supply was turned on first, and then the LabVIEW program was initiated to observe the voltage response, indicating that the structure was vibrating. The thermal chamber program

was then started to change the temperature. The LabVIEW program was allowed to run until the chamber completed the set temperature profile. After everything was turned off, the chamber was opened to allow ambient air back into the chamber for approximately 10 minutes before running another test.

4.2.1.2 Results and Discussion

The voltage was collected in each case, which was converted to power and then integrated over time to get energy. Three trials were conducted for each type of experiment. The energy amounts for each case are shown in Figure 4.15.

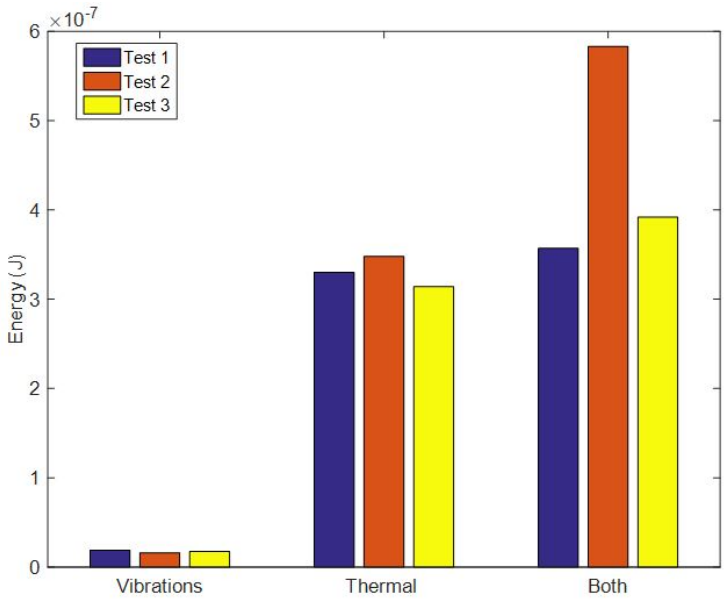

Figure 4.15: The energy generated by the vibration, thermal, and both experiments.

Except for test 2 for both experiments, if the energy from the vibration and the thermal experiments are added, the total nearly equals the energy of both experiments together. In all cases, the energy for both is greater than either standalone case, showing that this is a viable form of energy harvesting and will generate more energy, especially if everything is optimized correctly.

It is interesting to note that the thermal case's energy is greater than the vibration-based harvesting because no attempt was made to optimize the vibration harvester. In particular, the motor frequency, resistance, and positioning on the beam were not optimized, as suggested in the literature (see, for instance, [63]). Lastly, the RTD might be tapping the MFC due to convection in the running chamber, contributing to the energy via piezoelectricity. This tapping is evidenced by the pyroelectric coefficient being almost double the previously recorded value, as seen in Table 4.5.

Table 4.5: The Pyroelectric Coefficient of each thermal test

	Previously Recorded Value	Test 1	Test 2	Test 3
P2 Pyroelectric Coefficient ($\frac{\mu C}{m^2 K}$)	-343	-557	-602	-557

The pyroelectric coefficient was calculated using the same method as before for thermal cycling. Eq. 3.8 can filter out non-pyroelectric signals due to material defects, but any large signal like those generated by piezoelectricity would inevitably remain. The only difference is that this MFC is bonded, whereas the other MFC was free. However, compared to previous bonded tests on an aluminum shim when trying to understand how boundary conditions affected the pyroelectric coefficient (Section 3.4), these test results are much higher. The pyroelectric coefficient then was at a maximum of $-400\frac{\mu C}{m^2 K}$, which then decayed back to the free value after several cycles. This high pyroelectric coefficient probably has something else affecting it, and the piezoelectric voltage being generated by the RTD hitting the MFC would explain this and why the thermal test outperformed the vibration test.

To further analyze the thermal experiment's energy, the same numerical model used before to predict the energy for just the pyroelectric effect was used for this temperature profile and this resistance. According to the model, the energy was estimated as 65.6 nJ, whereas for these thermal

experiments, it is an average of 330 nJ, a whole order of magnitude difference. Some of that difference might be due to the different boundary conditions; however as stated earlier, the change in boundary condition alone cannot make up the difference in the energy gain.

4.2.2 Structural Health Monitoring with Energy Harvesting

Non-destructive SHM has become a popular way of evaluating whether a structure has been damaged without invasive testing. This non-destructive evaluation uses the piezoelectric effect by bonding a piezoelectric material to the structure and coupling the mechanical impedance of the structure with the electrical impedance of the piezoelectric material. This measured impedance is compared with a baseline impedance measured when the structure was healthy. If the impedance deviates significantly from the baseline, then damage has occurred since something has changed within the system.

It is well known that impedance changes with temperature. There are multiple methods of correcting the impedance for temperature via cross-correlation [64] or frequency shift damage metric [25]. However, this is for a static temperature change. It was previously shown in [65] that MFCs exhibit a thermal memory when undergoing thermal cycles resulting in a different impedance than the baseline even though no damage occurred in the structure and the impedance was taken at the same temperature. The impedance eventually stabilized with the same thermal cycle profile. Because temperature correction has already been studied in the literature, it is not implemented in this experiment.

4.2.2.1 Experimental Setup

The MFC and RTD were setup in the same way as most of the Michigan experiments in Chapter 3. Usually, for SHM, the P2 MFC is used because it is better for sensing applications, and in this case, it is also better at energy harvesting. The temperature profile was also kept the same with varying ramp rates. To help prevent clutter, a normally open (NO)) / normally closed (NC) dual channel relay, LBA110, was used to switch between taking voltage measurements being generated from the pyroelectric effect and the impedance measurements. A schematic for the wiring can be seen in Figure 4.16.

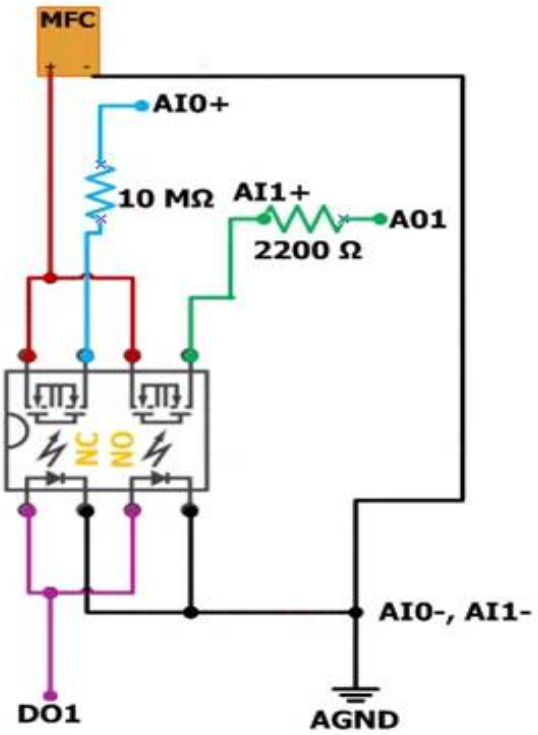

Figure 4.16: A wiring schematic of the experiment. A dual channel relay was used to operate both experiments automatically.

The relay was connected to the same digital port (digital out) on the DAQ so that when one channel is opened, the other channel closed. The pyroelectric experiment was connected to the

NC part of the relay so that it would run continuously for most of the thermal cycle duration. The impedance experiment was connected to the NO part of the relay so it can be measured at different times throughout the experiment. The DAQ sends out a frequency sweep through the analog out (AO), and the MFC responds with its own signal through the analog input (AI). A 2.2 kΩ resistor was connected across the AI and AO channels to filter out the response signal. The exact resistance had to be found through trial and error and will change if the structure differs in any significant way.

A LabVIEW VI was created to collect data for the pyroelectric voltage and to run the impedance experiment while saving data. The sampling rate for the pyroelectric experiment was 10 Hz, and 400 kHz for the impedance experiment. The frequency range sent by the chirp was between 100 Hz and 30 kHz. The data were averaged over ten frequency sweeps every six minutes while the program was running and saved to separate files. This timing created more data files for some experiments than for others as the thermal chamber had varying ramp rates.

4.2.2.2 Results and Discussion

The voltage, and the resulting current for a representative case can be seen in Figure 4.17.

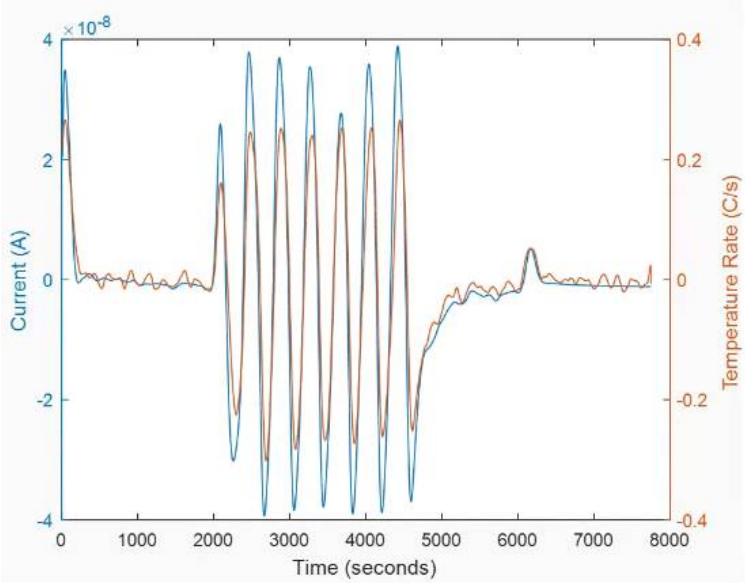

Figure 4.17: A graph of the current compared with the temperature rate showing that it is still generating an electric potential even with the interruptions from the impedance measurements.

These results show that energy can still be harvested using the pyroelectric effect even though the same MFC is being used for two different tasks. The current is still appears smooth and continuous even though there were interruptions for the SHM. The impedance experiments were relatively short in comparison to the time length of the pyroelectric experiment, so overall the current still follows the same trend as the temperature rate. The current was converted to energy to compare with the energy produced without taking impedance measurements and is depicted in Figure 4.18.

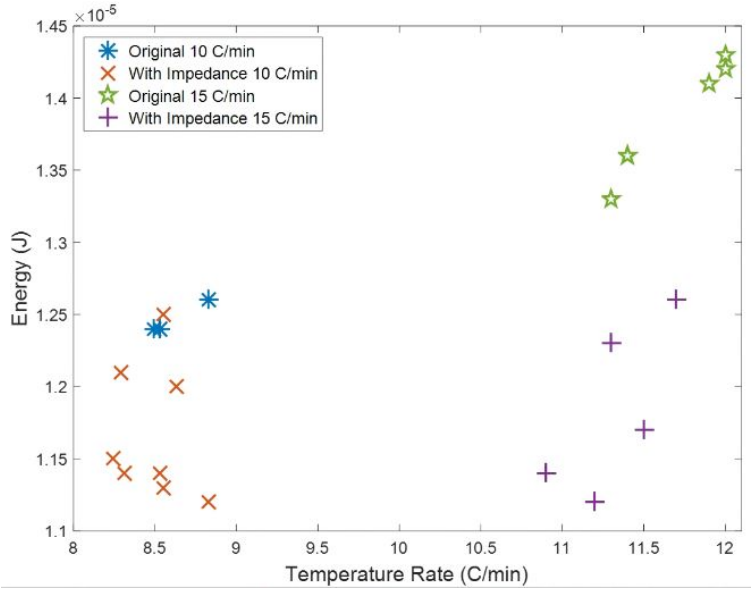

Figure 4.18: The energy from a P2 28 x 14 mm MFC from trials taken with and without impedance measurements at two different set temperature rates, $10°$C per minute and $15°$C per minute.

The energy produced by the experiments with impedance measurements is slightly less than the energy produced without any impedance, which is likely due to not being able to collect current data while running the impedance measurements. The amount of energy harvested is still a majority of the original energy produced and is still a viable means of getting free energy while monitoring for damage.

To show that the impedance was also measured and can be used for SHM, a graph of the real impedance as a function of frequency can be seen in Figure 4.19 during different points in the temperature profile. The impedance was measured every six to seven minutes while the chamber was running. The impedance changes with temperature, which is why the profiles vary and have a peak shift at different measurements. This variation with temperature shows that it can detect damage since the impedance is changing.

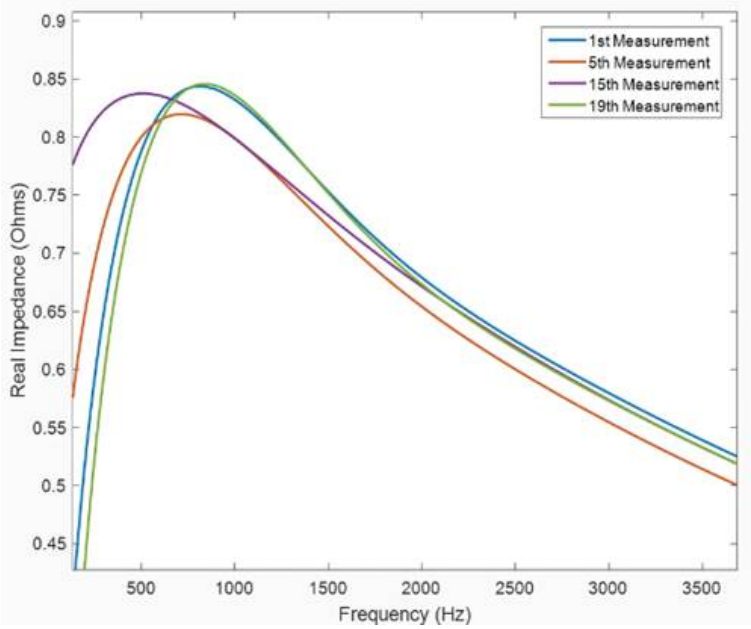

Figure 4.19: A sample experimental trial with several impedance measurements shown with varying profiles due to the temperature changing.

4.3 Chapter Summary

In this chapter, pyroelectric energy harvesting using an MFC was explored. Two different sized MFCs, 28 x 14 mm and 85 x 28 mm, as well as both different types of MFCs, P1 and P2, were used to model the energy harvested using an oscillating temperature profile at a rate of 5°C per minute and 10°C per minute. Three different models were established, one that was numerical, and two which were analytical. The numerical model used a temperature profile created by experimental data, which was also used to curve fit a sum of sines function and a sine wave utilized in the analytic models. The transfer function of the circuit was calculated and transformed from the Laplace domain to the time domain, and the voltage response was evaluated. The maximum power was estimated and normalized by the active area of the MFC to measure the maximum specific

power. These results were compared to experimental results using the same temperature profiles. The energy harvested was in the μJ range, and all the models had less than a 15% deviation from the average experimental value. All the models gave reasonably close results to the experimental energy harvested, but the sine wave model is not recommended to estimate the maximum specific power. The P2 MFC harvested the most energy and had a higher maximum specific power than the P1 MFC. As the temperature rate doubled, the amount of energy harvested approximately increased by 50%.

A resistance sweep was conducted on the numerical model to investigate the resistance value, which generated the most energy. The optimal resistor needed to harvest the most energy (in the mJ range) for this temperature application was in the GΩ to TΩ range. It was observed that as the temperature rate and size of the MFC increased, the optimal resistor value decreased. The maximum energy harvested also decreased slightly when the temperature rate increased, highlighting a slight trade-off when designing an energy harvesting circuit. The resistance sweep model was validated with experiments that were performed with varying resistances. The model was still accurate even when the temperature profile changed slightly.

This research provides an estimate on the energy harvesting capabilities of the MFC using the pyroelectric effect both experimentally and through modeling. It shows that the energy harvested depends significantly on the temperature profile, external resistor and capacitor used, and the size of the active material. Therefore, when designing a circuit, the design parameters and limitations must be well established. As long as the parameters used are accurate, a basic harmonic temperature profile to describe an oscillating temperature gives reasonably accurate results in predicting the energy generated.

Two proof of concept applications were also considered. The first was combining the piezo-

electric and pyroelectric effects for energy harvesting. Three different experiments were conducted to determine if combining the piezoelectric and pyroelectric effects would generate more energy. The energy for the three different experiments, vibration, thermal, and both combined, was computed from the collected data. The energy for the thermal tests was much greater than the energy measured using vibrations, but this was probably due to several reasons, the main ones being that the vibration experiment was not optimized and the RTD was most likely tapping the MFC which generated some piezoelectric voltage whenever the thermal chamber was running. This piezoelectric voltage is supported due to the pyroelectric coefficient being so large compared to the previously recorded average coefficient for thermal cycling and the predicted energy from the numerical model being an order of magnitude lower than the result in these experiments. In all cases, the energy for both the piezoelectric and pyroelectric effect was greater than each effect individually. This result shows that this is a viable energy harvesting solution from waste thermal energy as well as environmental vibrations. Due to Covid-19, this could not be optimized for maximum energy harvesting.

The second proof of concept idea was to combine SHM with pyroelectric energy harvesting. The current generated through the pyroelectric effect, and the impedance was measured as the MFC experienced thermal cycles. The energy was calculated and compared to experiments that were not interrupted with impedance measurements. The energy gathered was slightly less than the energy produced without the impedance measurements, which is likely due to the interruptions experienced from taking the impedance measurement. However, it still harvested most of the energy and is still a viable application worth pursuing when SHM. Energy harvesting will be beneficial in SHM scenarios where thermal cycles are unavoidable (i.e., space, or the desert). The number of interruptions and energy harvested depends on how often the operators want to check

for damage in a specific structure and the environment. If the environment has any vibrations and thermal variations, then piezoelectric and pyroelectric energy harvesting can be conducted when the impedance measurements are not running.

CHAPTER 5

Conclusion

This dissertation explores the pyroelectric effects in Macro-fiber Composites (MFCs) and characterizes them so that they may be used for pyroelectric applications such as energy harvesting. This chapter will summarize each chapter and highlight the main contributions of this dissertation. Recommendations for future work, as well as a current list of publications, are also included.

5.1 Dissertation Summary

The pyroelectric coefficient for two types of MFCs, P1 and P2, were modeled and validated with experiments. Several different applications were investigated and described in detail. The following sections provide a detailed summary of each chapter in this dissertation.

5.1.1 Chapter 2

The fundamental motivation behind this chapter was to model the pyroelectric coefficient in both MFCs. The pyroelectric coefficient is made up of the primary, secondary, tertiary, and electric field effects. The primary effect occurs when the material is in constant strain and is due to the change in spontaneous polarization over time. The secondary effect is when the material is

allowed to expand and therefore has an induced piezoelectric strain from the coefficient of thermal expansion (CTE). There is an additional contribution to the secondary effect in MFCs because of the CTE mismatch between layers in the composite. The tertiary effect (also called the false effect) occurs when there is a temperature gradient within the material (similar to the thermoelectric effect)) and is generally hard to measure because it involves knowing the stresses within the material as a function of position and thickness. The electric field effects occur when the electric field is not zero, and the dielectric permittivity varies with temperature. It was assumed that the tertiary and electric field effects were negligible when modeling the total pyroelectric coefficient.

The CTEs of both types of MFCs are required to model the pyroelectric coefficient in MFCs. In the literature, only the CTE for the P1 MFC has been reported. For consistency, both the P1 and P2 CTEs were estimated using equivalent micromechanical models. The CTEs found in this work does not agree with the CTEs for the P1 MFC from Park et al. [33] and Williams et al. [32] due to the different assumptions and techniques used in this model. It was assumed that each layer of the MFC was perfectly bonded, causing all layers to have a constant in-plane strain; so the in-plane CTEs were estimated using a volume average of the effective CTE of each layer. The effective CTE of a layer was calculated based on the rule of mixtures. The out of plane CTE was estimated as the weighted sum of the CTEs of the individual layers. A secant-based approximation was used to get an average value for the CTE over the specified temperature range since the CTE changes with temperature. Realistically, the MFC is probably not in constant stress or strain, so the actual value of the CTE is likely between the CTE estimated in this work and the CTE provided in Williams et al. [32] and Park et al. [33].

A brief discussion on two types of connectivity was given where parallel and series connections were specified as important and analogous to the rule of mixtures and inverse rule of mixtures. The

literature on these connections for diphasic pyroelectric materials was included and was similar to the rule of mixture equations derived for just one pyroelectric material in this dissertation.

The modeled CTE values were applied in micromechanics based modeling of pyroelectricity to estimate the pyroelectric coefficient and its constituents. The constitutive equations, along with the rule of mixtures, were used to estimate each layer's properties, assuming uniform in-plane strain and plane stress conditions. The secant method was used to approximate an average pyroelectric coefficient over the specified temperature range and was -55, -233, and 178 $\frac{\mu C}{m^2 K}$ and -323, -103, and -221 $\frac{\mu C}{m^2 K}$ for P1 and P2 total pyroelectric coefficient, primary coefficient, and secondary coefficient, respectively. Because the overall pyroelectric coefficient is negative, the secondary coefficient for the P1 MFC detracts from the total coefficient but contributes to the total coefficient for the P2 MFC. If the boundary conditions are manipulated, the secondary coefficient will change, further changing the total coefficient. This difference in the coefficient for both MFCs is due to the poling direction and the electrode placement for each MFC.

5.1.2 Chapter 3

This chapter seeks to experimentally measure the pyroelectric coefficient through various methods, equipment, and parameters. Two different methods were used, linear temperature ramping and thermal cycling. Linear temperature ramping has the disadvantage of being affected by thermally stimulated currents (TSCs), which can be caused by material defects. Therefore, it is more efficient to use thermal cycling so that these TSCs can be corrected easily via a phase shift, where the phase difference between the current and the temperature should be $90°$.

Different thermal chambers were utilized for linear temperature ramping and the thermal cy-

cling methods at NASA Langley Research Center and at the University of Michigan. The thermal chambers were set to linearly ramp from $25°C$ to $70°C$ at varying temperature rates. For thermal cycling, the temperature profile was cycled between $40°C$ and $100°C$. The data taken using the Michigan chamber while using the linear ramping method was not corrected for TSCs, which caused a significant discrepancy with the rest of the results. Linear ramping data in the NASA chamber after TSCs were subtracted resulted in a mean and standard deviation of -93 ± 17 and $-347 \pm 12 \frac{\mu C}{m^2 K}$ for the P1 and P2 type, respectively. Better precision was seen in the thermally cycled data with a mean and standard deviation of -82 ± 6 and $-343 \pm 15 \frac{\mu C}{m^2 K}$ for the P1 and P2 type, respectively. These total pyroelectric coefficient values are in reasonable agreement with the modeled pyroelectric coefficient values presented in Chapter 2.

The pyroelectric coefficient was enhanced using electromagnetic interference (EMI) for a different chamber at NASA Langley. The EMI could have occurred due to the small chamber and the proximity of the MFC to the open coil electric resistance heaters. The resistance heaters would produce an electric field that might affect the MFC and, with it, a changing magnetic field, which might induce a current in the MFC due to Faraday's Laws. The resulting pyroelectric coefficient was almost two times greater than the pyroelectric coefficient from the thermal cycling experiments (also called the reference pyroelectric coefficient). An energy harvesting figure of merit (FOM) was calculated for both MFCs and compared to the reference FOM, showing the pyroelectric effect was enhanced 7 to 11 times and 4 to 7 times for the P1 and P2 MFCs, respectively. This illustrates that the energy harvested from the MFC can significantly increase with any EMI which is advantageous where usually EMI is unwanted, and measures are taken to mitigate the EMI. However, there is little to no control over the amount of EMI the sample experiences which might be damaging to the material.

Because the pyroelectric coefficient is made up of the primary and secondary effects, the boundary conditions were changed on the MFC to observe how this changed the pyroelectric coefficient and if this value follows the same trend as the modeled pyroelectric constituents. Kevlar was sewn to the boundary of the MFC in the inactive area to observe if the pyroelectric coefficient would be closer to the primary coefficient modeled in Chapter 2. The constrained P1 pyroelectric coefficient was $-57\frac{\mu C}{m^2K}$, which did not agree with the modeled value of $-233\frac{\mu C}{m^2K}$ probably due to the Kevlar hindering the generation of current since the poling direction is in the plane of restriction. The constrained P2 pyroelectric coefficient was $-248\frac{\mu C}{m^2K}$, which decreased towards the modeled value of $-103\frac{\mu C}{m^2K}$. Likely, the Kevlar could not completely negate the expansion of the MFC.

Another way to change the boundary condition was to epoxy the MFC to a metal shim, which should increase the secondary effect because the epoxy and shim would have a higher CTE than the MFC. The pyroelectric coefficient for the epoxied P1 MFC was very similar to the constrained P1 pyroelectric coefficient. The pyroelectric coefficient for the epoxied P2 MFC actually increased to $-390\frac{\mu C}{m^2K}$ at first and eventually thermally relaxed back to the reference pyroelectric coefficient.

Overall, this chapter sought to experimentally characterize the pyroelectric coefficient through linear temperature ramping and thermal cycling in different chambers at NASA Langley and the University of Michigan. The pyroelectric coefficient was enhanced with EMI, and a FOM was calculated, showing the amount of enhancement produced from the EMI compared to the reference pyroelectric effect. The boundary conditions were also manipulated by trying to constrain the MFC and expand the MFC to yield different pyroelectric coefficients. This manipulation explores experimentally obtaining a lower bound for thin films (that have an inactive area), not just MFCs, for the primary and secondary effect once the total pyroelectric coefficient is known. Additionally,

vacuum effects in MFCs utilizing the pyroelectric effect was investigated (details in the Appendix), and preliminary results indicate a slight decrease in the pyroelectric coefficient. With this understanding of the pyroelectric coefficient, the MFC can be implemented in applications utilizing this effect.

5.1.3 Chapter 4

In this chapter, several applications are explored utilizing pyroelectric energy harvesting. The first application is just pyroelectric energy harvesting. The amount of energy harvested for two different sized MFCs of both types was modeled using an oscillating temperature profile based on experiments with a rate of $5°$C per minute and $10°$C per minute. The transfer function was derived using a representative circuit and then used in three different models: numerical, a sum of sines analytical model, and a generic sine wave model, to calculate the voltage response. This voltage was used to calculate the specific power by finding the maximum power and normalizing it by the active area of the MFC. This specific power, as well as the energy harvested, were compared with experimental results. All the models estimated the energy harvested within 15% of the average experimental value. As predicted by the FOM in Chapter 3, the P2 MFC harvested the most energy and had a higher maximum specific power. The amount of energy harvested for both MFCs increased by approximately 50% when the temperature rate doubled.

The pyroelectric energy harvested was optimized for this temperature profile by doing a resistance sweep using the numerical model. The most energy harvested went from the μJ range when the resistance was not optimized to the mJ range after optimization. However, the resistance required was extremely large, in the GΩ to TΩ range. As the size of the MFC and the temper-

ature rate increased, the optimal resistor value decreased, but there was also a slight decrease in the maximum energy harvested at the higher temperature rate. Experiments conducted at different resistances were used to validate the model. This research shows that the amount of energy harvested greatly depends on multiple parameters such as the size of the MFC, temperature profile, and resistor values and illustrates that significant energy can be generated through the pyroelectric effect which can be used to operate low power devices.

With this understanding of pyroelectric energy harvesting, two proof of concept applications using pyroelectric energy harvesting were investigated. First, combined energy harvesting was explored using the piezoelectric and pyroelectric effects. Three different experiments, vibration only, thermal only, and both combined, were conducted to determine if there was any benefit to combining the effects. Usually, piezoelectricity will generate more energy than pyroelectricity; however, the thermal experiment produced more energy than the vibration experiment. This occurred because of multiple reasons, the major reasons being the vibration experiment was not optimized, and the resistive temperature device (RTD) was most likely hitting the MFC, generating extra voltage through the piezoelectric effect whenever the thermal chamber was running. The pyroelectric coefficient and the energy were calculated for this experiment and were much greater and an order of magnitude higher than the reference coefficient and predicted energy, respectively, which supports the aforementioned conjecture. The energy generated from both combined was greater in all cases than each effect individually. Combined piezoelectric and pyroelectric energy harvesting is more beneficial and is a viable energy harvesting solution for waste energy from thermal and vibration sources. Due to Covid-19, this could not be optimized for maximum energy harvesting.

The second proof of concept idea was combining structural health monitoring (SHM) with pyroelectric energy harvesting. A circuit was assembled using a normally open (NO)/ normally

closed (NC) relay, which allowed the data acquisition device (DAQ) to collect data from the pyroelectric experiment and then switch to the SHM experiment after a specified time had passed, and then switch back to the pyroelectric experiment. The switching was done as the MFC experienced thermal cycles. The energy generated from the pyroelectric effect was calculated and was slightly less than experiments that were not interrupted from SHM. The decrease in energy is marginal, with a majority of the energy still being harvested and is therefore still beneficial to pursue in environments where thermal variations are present. The amount of energy harvested, in addition to the parameters mentioned for pyroelectric energy harvesting, depends on the number of interruptions experienced due to SHM, which is determined by the operator. This proof of concept idea can be combined with piezoelectricity as well to harvest even more energy.

5.2 Main Research Contributions

The following list summarizes the significant contributions of this dissertation in the field of pyroelectricity and MFCs.

- This work was the first to characterize the pyroelectric coefficient under free conditions in both the P1 and P2 type MFCs. The rule of mixtures and the constitutive equations were combined in a micromechanical model to predict the total, primary, and secondary pyroelectric coefficient. This modeled coefficient matched well with various experiments using two different methods and two different chambers to validate the coefficient.

- The CTEs for both MFC types were estimated using the rule of mixtures and assuming constant in-plane strain for each layer of the composite. This is the first time the P2 MFC CTE has been reported in the literature.

- The pyroelectric coefficient was enhanced significantly by a suspected EMI. This serendipitous discovery suggests that EMI could potentially be beneficial in terms of pyroelectric applications when steps are usually taken to mitigate any EMI.

- The boundary conditions of the MFCs were changed to analyze the effect it has on the pyroelectric coefficient, which can also provide enhancement through the secondary pyroelectric coefficient. This also provides a novel experimental method of trying to partially isolate the primary pyroelectric effect by sewing Kevlar to the inactive area of a thin film.

- This dissertation is the first to explore the potential effects that a high vacuum has on the pyroelectric coefficient in MFCs. Although only preliminary results were presented in Appendix B, it draws attention to the issue that vacuum might have adverse effects in the performance of the MFC used in pyroelectric applications.

- The energy generated by both MFCs through the pyroelectric effect was explored for the first time. The voltage response, energy, and max power density were modeled using a transfer function of the circuit and a numerical, sum of sines, and a sine wave approximation of the temperature profile. These models were validated with experimental data and optimized using a resistor sweep with maximum energy in the mJ range. This illustrates that the major parameters that need to be considered when designing for pyroelectric energy harvesting are the external resistor and capacitor value, the size of the material, and the temperature profile and rate.

- The energy generated using both the piezoelectric effect with an external motor for vibration, and the pyroelectric effect was investigated in MFCs for the first time. A novel experiment

was developed using a cell phone motor as the vibration source, which was epoxied onto an aluminum beam with a P2 MFC already epoxied to it, which was put inside a thermal chamber. The amount of energy generated from the combined effects was greater than each individual effect. It validates that it is more beneficial to do combined energy harvesting when possible, as well as that MFCs are viable materials for harvesting energy from both effects in a real-world environment.

- Showed a potential dual application, SHM and pyroelectric energy harvesting, was viable and can be used to harvest waste energy when SHM is on standby. A circuit was soldered using a NO and NC relay, which allowed the same MFC to take impedance measurements and harvest energy. This application can easily be implemented in the real-world environment and collect free energy from the environment while ensuring the structure the MFC is attached to is not damaged.

5.3 Recommendations for Future Work

While this dissertation has made great strides in understanding the pyroelectric effect in MFCs, some aspects can be improved upon and researched further. Upon doing tests with the same MFCs for years, there was suddenly a noticeable reduction in the pyroelectric coefficient (around 20 to $50\frac{\mu C}{m^2K}$). This reduction may be caused by an unknown variable affecting the MFC suddenly (such as transportation, static shock, etc.) or a change in the equipment being used to measure the pyroelectric coefficient. The capacitance seemed unchanged, and one trial taken with a new MFC measured a pyroelectric coefficient closer to the reference value. However, the material could also be degrading over time. More testing is recommended to observe if the duty cycle for the

pyroelectric effect is different than the duty cycle for the piezoelectric effect.

Piezoelectric and pyroelectric energy harvesting was investigated as a potential application. It would be useful to try to optimize both the piezoelectric and pyroelectric energy harvested and compare that with an optimized pyroelectric and optimized piezoelectric experiment. Pyroelectricity usually requires high resistances to achieve the optimal energy harvested, whereas piezoelectricity usually requires significantly lower resistances. Both effects will need some compromise on the resistor choice. Assuming the experiment conducted in this dissertation is comparable to an optimized combined energy harvesting experiment versus the same parameters as the optimized combined effects for each of the individual experiments, then the optimized combined experiment will probably produce more energy than the individual effects. It would be interesting to know if the optimized combined energy harvesting produces more energy than either of the optimized effects individually.

Additionally, in the Appendices vacuum effects on the pyroelectric coefficient in MFCs are explored. Only a limited number of trials are shown due to several challenges experienced while conducting the experiments. This was challenging because a heat source and cooling source that doesn't rely on convection needs to be installed in a high vacuum chamber. It is harder to control the temperature rates in vacuum because of the lack of convection. Preliminary results indicate that vacuum has a slight affect on the pyroelectric coefficient, decreasing the value for both MFCs on average. More tests should be conducted before a definitive conclusion can be drawn. This is especially important because some of the main applications where pyroelectric energy harvesting could work really well is in space either on CubeSats or on the International Space Station where there may not be atmosphere.

Finally, it would be interesting to look into the electrocaloric effect (or the inverse pyroelectric

effect) and electrocaloric coefficient of MFCs. The specific heat would also need to be measured to calculate this coefficient. Usually, the electrocaloric effect requires high electric fields which cause the material to either heat up or cool down. This is a way to achieve refrigeration; however, the high electric fields might damage the MFC in the long term or end up depoling the MFC. In addition, the equipment needed would have to be precise in measuring a temperature change, and the experiment would have to be designed in a way where the temperature change of the material is due to the electrocaloric effect and not from another phenomenon such as Joule heating. The P1 MFC can withstand higher electric fields according to the manufacturer, but the P2 MFC performed better using the pyroelectric effect, so there might be an interesting trade-off here which could be worth investigating.

5.4 Publications

Below is a list of publications that are separated by journal publications and conference proceedings. Within each section are categories in which all the papers that contributed to that topic are included.

5.4.1 Journal Publications

Model and experimentally characterize the pyroelectric coefficient:

- Acosta, K. L., Wilkie, W. K., and Inman, D. J, "Pyroelectric Coefficient of Macro-fiber Composites Under Vacuum," Letter, In Review

- Acosta, K. L., Srivastava, S., Wilkie, W. K., and Inman, D. J., "Primary and secondary pyro-

electric effects in macro-fiber composites," *Composites Part B: Engineering*, Vol. 177, 2019, pp. 107275.

- Acosta, K. L., Wilkie, W. K., and Inman, D. J, "Characterizing the Pyroelectric Coefficient for Macro-Fiber Composites," *Smart Materials and Structures*, Vol. 27, No.11, 2018, pp. 115001.

Pyroelectric Energy Harvesting:

- Acosta, K. L., Wilkie, W. K., and Inman, D. J., "Energy Harvesting using the Pyroelectric Effect in Macro-fiber Composites," *Journal of Intelligent Materials Systems and Structures*, September 2020. doi:10.1177/1045389X20957094

5.4.2 Conference Proceedings

Experimentally characterizing the pyroelectric coefficient

- Acosta, K. L., Wilkie, W. K., and Inman, D. J., "Pyroelectric Coefficient Enhancement of Macro-fiber Composites using Electric Fields," *AIAA Scitech 2020 Forum*, 2020, p. 0151.

Impedance and Pyroelectric Effect:

- Acosta, K. L., Wilkie, W. K., and Inman, D. J., "Analysis of Impedance on Macro-fiber Composites undergoing Thermal Cycles," *ICAST Digital Library*, 30 Sept - 4 Oct 2018.

Space Application:

- Acosta, K. L., Hobeck, J. D., Owen, R. B., and Inman, D. J., "Macro-Fiber Composites Under Thermal Cycles For Space Applications", *Sensors and Smart Structures Technologies*

for Civil, Mechanical, and Aerospace Systems 2017, Vol. 10168, International Society for Optics andPhotonics, 2017, p. 101683E.

APPENDIX A

Table of CTE Values for MFCs

Table A.1: Coefficient of Thermal Expansion for MFCs at Different Temperatures

Temperature (°C)	**P1 CTE (μm/m °C)**	**P2 CTE (μm/m °C)**
25	$\alpha_1 = 27.70$ $\alpha_2 = 6.68$ $\alpha_3 = 9.69$	$\alpha_1 = 7.16$ $\alpha_2 = 7.16$ $\alpha_3 = 28.90$
50	$\alpha_1 = 27.78$ $\alpha_2 = 6.56$ $\alpha_3 = 9.41$	$\alpha_1 = 7.03$ $\alpha_2 = 7.03$ $\alpha_3 = 28.90$
60	$\alpha_1 = 27.98$ $\alpha_2 = 6.61$ $\alpha_3 = 9.04$	$\alpha_1 = 7.07$ $\alpha_2 = 7.07$ $\alpha_3 = 28.87$
65	$\alpha_1 = 48.15$ $\alpha_2 = 9.88$ $\alpha_3 = 12.7$	$\alpha_1 = 10.64$ $\alpha_2 = 10.64$ $\alpha_3 = 49.03$
70	$\alpha_1 = 48.19$ $\alpha_2 = 9.82$ $\alpha_3 = 12.52$	$\alpha_1 = 10.58$ $\alpha_2 = 10.58$ $\alpha_3 = 49.00$
100	$\alpha_1 = 48.25$ $\alpha_2 = 9.40$ $\alpha_3 = 11.41$	$\alpha_1 = 10.12$ $\alpha_2 = 10.12$ $\alpha_3 = 48.72$
TR	$\alpha_1 = 37.97$ $\alpha_2 = 8.13$ $\alpha_3 = 10.77$	$\alpha_1 = 8.74$ $\alpha_2 = 8.74$ $\alpha_3 = 38.87$
B. Williams [32] (25°C)	$\alpha_1 = - - -$ $\alpha_2 = 14.69$ $\alpha_3 = 7.89$	—
J. S. Park [33] (25°C)	$\alpha_1 = - - -$ $\alpha_2 = 14.76$ $\alpha_3 = 4.81$	—

APPENDIX B

Pyroelectric Effects of MFCs under Vacuum

Some potential applications for utilizing the pyroelectric effect in MFCs are in space. The environment in space is very unforgiving. There is a vacuum that encourages the development of tin whiskers that cause electrical shorts. There is also outgassing of most materials that can degrade the material and coat optical equipment, charged particles, radiation, micrometeoroids, electrostatic discharge, and extreme temperatures depending on the distance from the sun. If the spacecraft is in orbit around Earth, then there is also atomic oxygen, a significant concern for eroding specific materials such as plastics. In particular, Kapton is vulnerable to atomic oxygen and will erode on the MFC, exposing the electrodes in just a few months.

These problems can be mitigated; however, the extent to which the pyroelectric effect in MFCs is affected by vacuum is unknown. In theory, the performance should not change drastically since the MFC does not outgas much and was tested in space before [66]. For this reason, a high vacuum chamber at NASA Langley was procured, and the crystal quartz lamp described in Chapter 3 was used to heat and cool the sample. The whole setup can be seen in Figure B.1. On the jacket of the lamp furnace, there are connection ports for gas and liquid coolant; however, a metal coil was used instead as it had closer contact with the sample. Because the light intensity of the crystal quartz lamps are high and the metal coil would not fit inside the furnace when it was shut, the furnace

was kept open with the four lamps positioned as equidistant from the material as possible. The temperature is hard to control in a vacuum, so if the coolant was running through the jacket, there would be a significant delay in the temperature decreasing, whereas since the coils are closer to the sample, it can cool it directly through conduction. The controller for the lamps was calibrated via an autotune feature where the temperature was set to 70°C with the coolant flowing continuously to control the temperature rate. The MFC, thermocouple, and RTD were covered with aluminum foil to mitigate EMI and any heat absorption issues between the different materials.

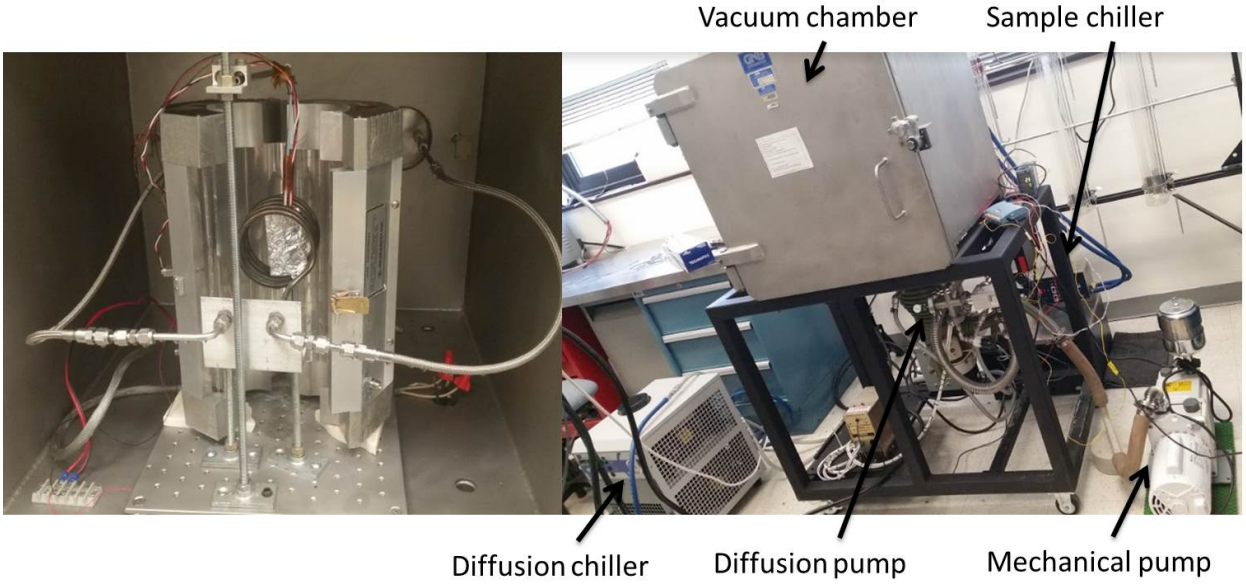

Figure B.1: (left) The setup of the crystal quartz lamps with vacuum grade hoses and a coil encircling the sample to further help with cooling. (right) The whole vacuum chamber with a mechanical pump to drive the vacuum down to mTorr and then a diffusion pump to get the vacuum down to the μTorr range. A diffusion chiller is necessary to cool the diffusion pump, and a separate chiller is needed to cool the sample.

Both linear temperature ramping and thermal cycling were attempted at a high vacuum. The wires from the MFC, RTD, and temperature control thermocouple were fed through the chamber by a high vacuum connector. From there, the thermocouple was connected to the temperature control

device, and the MFC and RTD were connected to the DAQ. A 10 MΩ resistor was connected in parallel with the MFC like in Chapter 3. After everything inside was prepared, the chamber was closed, and the mechanical pump was turned on until the chamber was reading less than 100 mTorr. The diffusion pump was turned on to heat up along with the diffusion chiller to prevent it from overheating. Once the diffusion pump was hot, the valve to the diffusion pump was opened, and the air was pumped down into the μTorr range. The sample chiller was turned on, which had used ethanol to get as cold as possible (max was approximately -28°C). After the chamber had a vacuum and the sample chiller was cold, the experiment was performed by programming the temperature profile into the temperature controller and recording the data. Because of time constraints, the MFC was only cycled five times instead of seven as in Chapter 3.

Because the temperature rate is hard to control since there is no convection, at higher temperature rates, the controller would struggle, initially, to match the set temperature and would overcompensate until the set temperature caught up, especially in the thermal cycles. This overcompensation would cause a spike in the current, as seen in Figure B.2. Additionally, the temperature difference for the first cycle was the greatest where subsequent cycles only varied between 75 and 90°C even though it was set to cycle between room temperature and 100°C. For this reason, the first cycle was not included in most of the pyroelectric coefficient calculations.

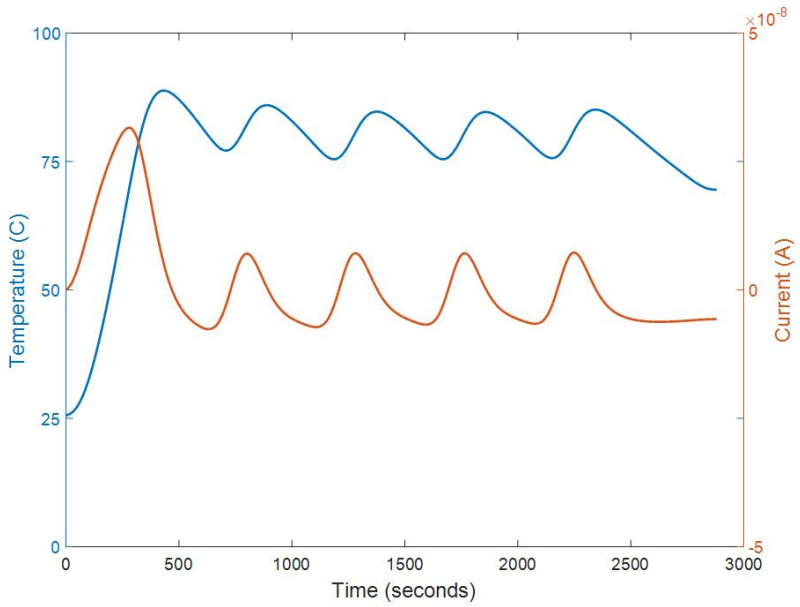

Figure B.2: The temperature profile from the RTD and current generated from the MFC.

The pyroelectric coefficient was calculated as presented in Chapter 3 for both methods, including subtracting the TSCs for the linear temperature ramping. The linear temperature ramping results are shown in Figure B.3. Vacuum data was not recorded during these experiments. If compared with the results from Chapter 3, the coefficient value has slightly decreased. The P1 MFC has more spread than the P2 MFC; however, the amount of trials for the P1 MFC is also more.

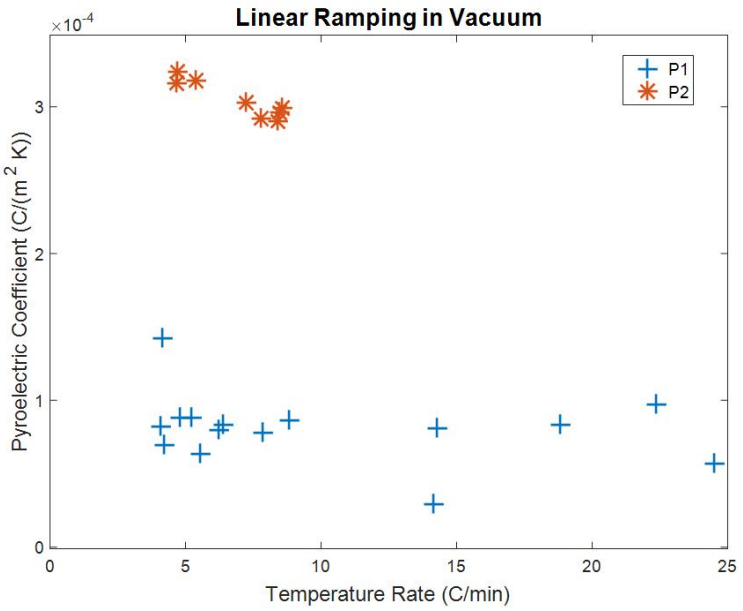

Figure B.3: All of the pyroelectric coefficient results for both MFCs using linear temperature ramping in a vacuum.

The thermal cycled data can be seen in Figure B.4 along with vacuum data on the right y-axis. This figure also shows a slightly lower coefficient than the results in Chapter 3, however, some results are inside the data range presented in Chapter 3 and within the standard deviation of the average. Due to time constraints, the same amount of P1 MFC trials could not be completed as the amount of P2 MFC trials.

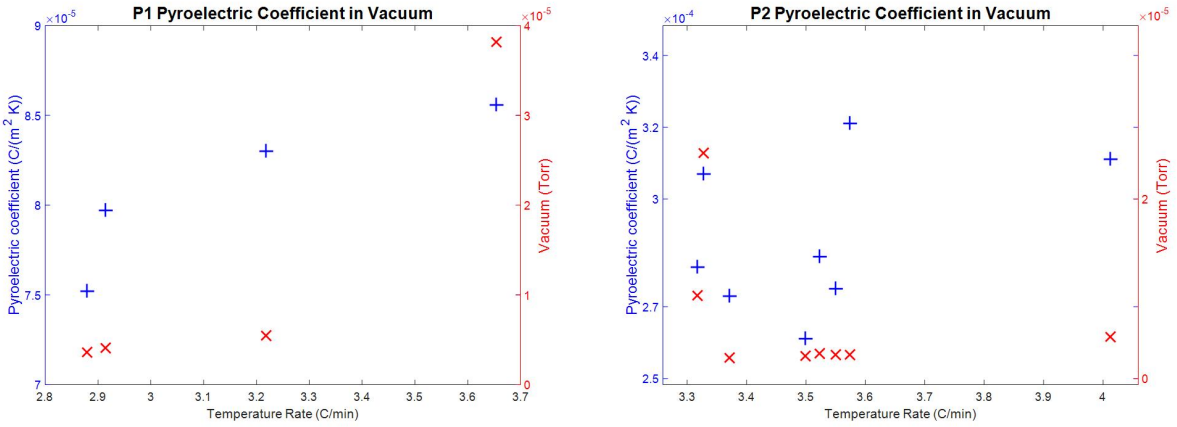

Figure B.4: The P1 and P2 pyroelectric coefficient (blue plus) from thermal cycles along with the average vacuum pulled during the test (red x).

A limited number of trials are presented here. In addition to time constraints, several issues became apparent as testing went forward. Even with ethanol as the cooling fluid, the sample chiller was not cold enough or flowing fast enough to sufficiently lower the temperature with the same heating rate, which is why the thermal cycles have such a narrow temperature range. There was also additional EMI due to the coil surrounding the sample, so thicker aluminum foil had to be used to mitigate the effects to measure the vacuum induced effects on the pyroelectric coefficient accurately. Furthermore, occasionally throughout testing, the high vacuum cold cathode gauge would disconnect, so there is missing vacuum data. Also, the black grounding wire for the RTD became exposed and started to short due to wire melting and outgassing because more light was absorbed. The RTD was fixed temporarily with electrical tape. Due to all of these issues, a significant amount of experiments needed to be scrapped.

Table B.1 compares the average taken from Chapter 3 in the same NASA chamber taken at atmospheric conditions to the coefficient taken in a vacuum. The P1 coefficient is marginally lower than the coefficient taken in the atmosphere; however, the P2 coefficient has noticeably decreased.

The P2 pyroelectric coefficient value is larger than the P1 MFC so it may be more sensitive to changes that might affect the pyroelectric coefficient since it can generate more current. Note, this is different from the TSCs influencing the pyroelectric current since those are non-pyroelectric in nature and generally affect the P1 MFC more.

Table B.1: The average pyroelectric coefficient in a vacuum with the standard deviation for linear ramping and thermal cycling compared with previous results conducted in the atmosphere using the same chamber at NASA.

p ($\frac{-\mu C}{m^2 K}$)	Linear Ramp Atmosphere	Thermal Cycling Atmosphere	Linear Ramping	Thermal Cycling
P1	93.28 ± 17.39	82.8 ± 12.0	79.7 ± 10.8	80.9 ± 4.48
P2	347.04 ± 12.04	322 ± 17.1	305 ± 13.0	289 ± 21.2

These tests were performed over two summers at NASA Langley Research Center where the first summer focused primarily on linear temperature ramping, and the second summer focused on thermal cycling. Because the pyroelectric coefficient decreased using both measuring methods (linear ramping and thermal cycling), it lends credence that there could be a phenomenon occurring that could adversely affect the pyroelectric effect in vacuum. Preliminary results shown indicate that the pyroelectric coefficient decreases marginally in the P1 and slightly more in the P2 MFC. A possible explanation could be that the MFC might be so sensitive (the current being measured is in nA so it is likely that small changes will affect it) that if it is at zero stress in atmosphere, that putting it in vacuum (or negative pressure) changes the stress state of the MFC which would affect the pyroelectric coefficient. This might be more relevant in a composite like the MFC than a bulk material like PZT-5A because there could be interlaminar stress or strain from the different materials relaxing differently in vacuum. However, more testing is recommended before any conclusion is reached.

BIBLIOGRAPHY

[1] Zhao, J. and You, Z., "A shoe-embedded piezoelectric energy harvester for wearable sensors," *Sensors*, Vol. 14, No. 7, 2014, pp. 12497–12510.

[2] Lang, S. B., "The history of pyroelectricity: from ancient Greece to space missions," *Ferroelectrics*, Vol. 230, No. 1, 1999, pp. 99–108.

[3] Chew, K.-H., Shin, F. G., Ploss, B., Chan, H. L., and Choy, C., "Primary and secondary pyroelectric effects of ferroelectric 0-3 composites," *Journal of applied physics*, Vol. 94, No. 2, 2003, pp. 1134–1145.

[4] Bowen, C. R., Taylor, J., LeBoulbar, E., Zabek, D., Chauhan, A., and Vaish, R., "Pyroelectric materials and devices for energy harvesting applications," *Energy & Environmental Science*, Vol. 7, No. 12, 2014, pp. 3836–3856.

[5] Athenstaedt, H., Claussen, H., and Schaper, D., "Epidermis of human skin: pyroelectric and piezoelectric sensor layer," *Science*, Vol. 216, No. 4549, 1982, pp. 1018–1020.

[6] Huey, L. B. K. T. L., Zhang, H. H. F. B. T., and Li, S., "Waste Energy Harvesting-Mechanical And Thermal Energies (2014). pdf," .

[7] Xusheng, W., "A study of tertiary pyroelectric effect," *Ferroelectrics Letters Section*, Vol. 12, No. 5, 1991, pp. 115–121.

[8] Jachalke, S., Mehner, E., Stöcker, H., Hanzig, J., Sonntag, M., Weigel, T., Leisegang, T., and Meyer, D., "How to measure the pyroelectric coefficient?" *Applied Physics Reviews*, Vol. 4, No. 2, 2017, pp. 021303.

[9] Hagood, N. W., Kindel, R., Ghandi, K., and Gaudenzi, P., "Improving transverse actuation of piezoceramics using interdigitated surface electrodes," *Smart Structures and Materials 1993: Smart Structures and Intelligent Systems*, Vol. 1917, International Society for Optics and Photonics, 1993, pp. 341–352.

[10] Hagood, N. and Bent, A., "Development of piezoelectric fiber composites for structural actuation," *34th Structures, Structural Dynamics and Materials Conference*, 1993, p. 1717.

[11] Bent, A. A. and Hagood, N. W., "Piezoelectric fiber composites with interdigitated electrodes," *Journal of intelligent material systems and structures*, Vol. 8, No. 11, 1997, pp. 903–919.

[12] Wilkie, W. K., Bryant, R. G., High, J. W., Fox, R. L., Hellbaum, R. F., Jalink Jr, A., Little, B. D., and Mirick, P. H., "Low-cost piezocomposite actuator for structural control applications," *Smart structures and materials 2000: industrial and commercial applications of smart structures technologies*, Vol. 3991, International Society for Optics and Photonics, 2000, pp. 323–334.

[13] "NASA ICB 2006 Awards, Invention of the Year Award for 2006, https://icb.nasa.gov/archive/2006, 2006, National Air and Space Agency," .

[14] Williams, R. B., Grimsley, B. W., Inman, D. J., and Wilkie, W. K., "Manufacturing and mechanics-based characterization of macro fiber composite actuators," *ASME 2002 international mechanical engineering congress and exposition*, American Society of Mechanical Engineers Digital Collection, 2002, pp. 79–89.

[15] Harb, A., "Energy harvesting: State-of-the-art," *Renewable Energy*, Vol. 36, No. 10, 2011, pp. 2641–2654.

[16] Boisseau, S., Despesse, G., and Seddik, B. A., "Electrostatic Conversion for Vibration Energy Harvesting, Small-Scale Energy Harvesting, Dr. Mickaël Lallart (Ed.), ISBN: 978-953-51-0826-9, InTech, DOI: 10.5772/51360," 2012.

[17] Catacuzzeno, L., Orfei, F., Di Michele, A., Sforna, L., Franciolini, F., and Gammaitoni, L., "Energy harvesting from a bio cell," *Nano energy*, Vol. 56, 2019, pp. 823–827.

[18] Park, S., Grisso, B. L., Inman, D. J., and Yun, C.-B., "MFC-based structural health monitoring using a miniaturized impedance measuring chip for corrosion detection," *Research in Nondestructive Evaluation*, Vol. 18, No. 2, 2007, pp. 139–150.

[19] Xie, J., Mane, X., Green, C., Mossi, K., and Leang, K. K., "Performance of thin piezoelectric materials for pyroelectric energy harvesting," *Journal of Intelligent Material Systems and Structures*, Vol. 21, No. 3, 2010, pp. 243–249.

[20] Zakharov, D., Lebedev, G., Cugat, O., Delamare, J., Viala, B., Lafont, T., Gimeno, L., and Shelyakov, A., "Thermal energy conversion by coupled shape memory and piezoelectric effects," *Journal of Micromechanics and Microengineering*, Vol. 22, No. 9, 2012, pp. 094005.

[21] Suchaneck, G., Eydam, A., Hu, W., Kranz, B., Drossel, W.-g., and Gerlach, G., "Evaluation of polarization of embedded piezoelectrics by the thermal wave method," *IEEE transactions on ultrasonics, ferroelectrics, and frequency control*, Vol. 59, No. 9, 2012, pp. 1950–1954.

[22] Newnham, R., Skinner, D., and Cross, L., "Connectivity and piezoelectric-pyroelectric composites," *Materials Research Bulletin*, Vol. 13, No. 5, 1978, pp. 525–536.

[23] Zakharov, D., Gusarov, B., Gusarova, E., Viala, B., Cugat, O., Delamare, J., and Gimeno, L., "Combined pyroelectric, piezoelectric and shape memory effects for thermal energy harvesting," *Journal of Physics: Conference Series*, Vol. 476, IOP Publishing, 2013, p. 012021.

[24] Grisso, B. L. and Inman, D. J., "Temperature corrected sensor diagnostics for impedance-based SHM," *Journal of Sound and Vibration*, Vol. 329, No. 12, 2010, pp. 2323–2336.

[25] Park, G., Kabeya, K., Cudney, H. H., and Inman, D. J., "Impedance-based structural health monitoring for temperature varying applications," *JSME International Journal Series A Solid Mechanics and Material Engineering*, Vol. 42, No. 2, 1999, pp. 249–258.

[26] Salmanpour, M., Sharif Khodaei, Z., and Aliabadi, M., "Guided wave temperature correction methods in structural health monitoring," *Journal of Intelligent Material Systems and Structures*, Vol. 28, No. 5, 2017, pp. 604–618.

[27] Parr, R. G., "Density functional theory of atoms and molecules," *Horizons of Quantum Chemistry*, Springer, 1980, pp. 5–15.

[28] Biscani, F., Nasser, H., Belouettar, S., and Carrera, E., "Equivalent electro-elastic properties of Macro Fiber Composite (MFC) transducers using asymptotic expansion approach," *Composites Part B: Engineering*, Vol. 42, No. 3, 2011, pp. 444–455.

[29] Deraemaeker, A., Nasser, H., Benjeddou, A., and Preumont, A., "Mixing rules for the piezoelectric properties of macro fiber composites," *Journal of intelligent material systems and structures*, Vol. 20, No. 12, 2009, pp. 1475–1482.

[30] Venkatragavaraj, E., Satish, B., Vinod, P., and Vijaya, M., "Piezoelectric properties of ferroelectric PZT-polymer composites," *Journal of Physics D: Applied Physics*, Vol. 34, No. 4, 2001, pp. 487.

[31] Bert, C. W., "Classical Lamination Theory," *Manual on Experimental Methods for Mechanical Testing of Composites*, Springer, 1989, pp. 11–16.

[32] Williams, R. B., Inman, D. J., and Wilkie, W. K., "Temperature-dependent thermoelastic properties for macro fiber composite actuators," *Journal of Thermal Stresses*, Vol. 27, No. 10, 2004, pp. 903–915.

[33] Park, J.-S. and Kim, J.-H., "Coefficients of thermal expansion for single crystal piezoelectric fiber composites," *Composites Part B: Engineering*, Vol. 38, No. 7-8, 2007, pp. 795–799.

[34] Steiger, K. and Mokrỳ, P., "Finite element analysis of the macro fiber composite actuator: macroscopic elastic and piezoelectric properties and active control thereof by means of negative capacitance shunt circuit," *Smart Materials and Structures*, Vol. 24, No. 2, 2015, pp. 025026.

[35] Newnham, R. E., *Properties of materials: anisotropy, symmetry, structure*, Oxford University Press on Demand, 2005.

[36] Ackermann, M., Andersen, L., Becker, P., and Bohatỳ, L., "Pyroelectric properties of the monoclinic rare earth nitrates A2Ln (NO3) 5· 4H2O (A= NH4, Rb; Ln= La, Ce)," *Zeitschrift für Kristallographie-Crystalline Materials*, Vol. 230, No. 11, 2015, pp. 633–638.

[37] Berlincourt, D., "Variation of electroelastic constants of polycrystalline lead titanate zirconate with thoroughness of poling," *The Journal of the Acoustical Society of America*, Vol. 36, No. 3, 1964, pp. 515–520.

[38] Fjellvåg, H., "Symmetry-operations, point groups, space groups and crystal structure," *KJ/MV*, Vol. 210, 1994.

[39] Berlincourt, D., Krueger, H., and Near, C., "Properties of Morgan electro ceramic ceramics," *Technical Publication TP-226, Morgan Electro Ceramics*, 2000.

[40] "Smart Materials Corp., "5A1, 5H2 Typical Material Properties," PZT Fibers Material Available: https://www.smart-material.com/PZTFiber-product-material.html." .

[41] Bhalla, A. and Cross, L., "Primary and secondary pyroelectricity in proper and improper ferroelec," *Ferroelectrics*, Vol. 38, No. 1, 1981, pp. 935–938.

[42] Cook Jr, W., Berlincourt, D., and Scholz, F., "Thermal expansion and pyroelectricity in lead titanate zirconate and barium titanate," *Journal of Applied Physics*, Vol. 34, No. 5, 1963, pp. 1392–1398.

[43] Smart-Material, "MFC, [Online]. Available: http://www.smart-material.com/mfc-product-main.html. [Accessed: 08-Jul-2016]." .

[44] Pepi, J. W., "Linear analysis using secants for materials with temperature dependent nonlinear elastic modulus and thermal expansion properties," *Optomechanical Engineering 2017*, Vol. 10371, International Society for Optics and Photonics, 2017, p. 1037108.

[45] High, J. W., *Method of fabricating NASA-standard macro-fiber composite piezoelectric actuators*, National Aeronautics and Space Administration, Langley Research Center, 2003.

[46] Newnham, R. E., Bowen, L., Klicker, K., and Cross, L., "Composite piezoelectric transducers," *Materials & Design*, Vol. 2, No. 2, 1980, pp. 93–106.

[47] Bhalla, A., Newnham, R., Cross, L., Schulze, W., Dougherty, J., and Smith, W., "Pyroelectric PZT-polymer composites," *Ferroelectrics*, Vol. 33, No. 1, 1981, pp. 139–146.

[48] Lang, S. B. and Steckel, F., "Method for the measurement of the pyroelectric coefficient, dc dielectric constant, and volume resistivity of a polar material," *Review of Scientific Instruments*, Vol. 36, No. 7, 1965, pp. 929–932.

[49] "Analog Devices, "Low Voltage Temperature Sensors," TMP35/TMP36/TMP37 datasheet, Revision H," .

[50] Pandya, S., Velarde, G., Zhang, L., Wilbur, J. D., Smith, A., Hanrahan, B., Dames, C., and Martin, L. W., "New approach to waste-heat energy harvesting: pyroelectric energy conversion," *NPG Asia Materials*, Vol. 11, No. 1, 2019, pp. 1–5.

[51] Sebald, G., Lefeuvre, E., and Guyomar, D., "Ultrasonics, Ferroelectrics, and Frequency Control," *IEEE Transactions on*, Vol. 55, No. 3, 2008, pp. 538–551.

[52] Hanrahan, B. M., Sze, F., Smith, A. N., and Jankowski, N. R., "Thermodynamic cycle optimization for pyroelectric energy conversion in the thin film regime," *International Journal of Energy Research*, Vol. 41, No. 13, 2017, pp. 1880–1890.

[53] McKinley, I. M., Kandilian, R., and Pilon, L., "Waste heat energy harvesting using the Olsen cycle on 0.945 Pb (Zn1/3Nb2/3) O3–0.055 PbTiO3 single crystals," *Smart Materials and Structures*, Vol. 21, No. 3, 2012, pp. 035015.

[54] Siao, A.-S., McKinley, I. M., Chao, C.-K., Hsiao, C.-C., and Pilon, L., "Pyroelectric waste heat energy harvesting using the Olsen cycle on Pb (Zr, Ti) O3-Pb (Ni, Nb) O3 ceramics," *Journal of Applied Physics*, Vol. 124, No. 17, 2018, pp. 174104.

[55] "Thermal Dependency of Material Properties, Piezo. [Online]. Available: https://support.piezo.com/article/62-material-properties . [Accessed: 28-October-2019]," .

[56] Sebald, G., Seveyrat, L., Guyomar, D., Lebrun, L., Guiffard, B., and Pruvost, S., "Electrocaloric and pyroelectric properties of 0.75 Pb (Mg 1/ 3 Nb 2/ 3) O 3–0.25 Pb Ti O 3 single crystals," *Journal of applied physics*, Vol. 100, No. 12, 2006, pp. 124112.

[57] Lingam, D., Parikh, A. R., Huang, J., Jain, A., and Minary-Jolandan, M., "Nano/microscale pyroelectric energy harvesting: challenges and opportunities," *International Journal of Smart and Nano Materials*, Vol. 4, No. 4, 2013, pp. 229–245.

[58] Munn, R., "Theory of piezoelectricity, electrostriction, and pyroelectricity in molecular crystals," *The Journal of chemical physics*, Vol. 132, No. 10, 2010, pp. 104512.

[59] Schein, L. B., Cressman, P. J., and Cross, L. E., "Electrostatic measurements of unusually large secondary pyroelectricity in partially clamped LiNbO3," *Ferroelectrics*, Vol. 22, No. 1, 1978, pp. 937–943.

[60] "DuPont, "Kevlar Aramid Fiber Technical Guide," Available: http://www.dupont.com/content/dam/dupont/products-and-services/fabrics-fibers-and-nonwovens/fibers/documents/Kevlar_Technical_Guide.pdf," .

[61] Sodano, H. A., Inman, D. J., and Park, G., "Comparison of piezoelectric energy harvesting devices for recharging batteries," *Journal of intelligent material systems and structures*, Vol. 16, No. 10, 2005, pp. 799–807.

[62] Tungpimolrut, K., Hatti, N., Phontip, J., Komoljindakul, K., Pechrach, K., and Manooonpong, P., "Design of energy harvester circuit for a MFC piezoelectric based on electrical circuit modeling," *2011 International Symposium on Applications of Ferroelectrics (ISAF/PFM) and 2011 International Symposium on Piezoresponse Force Microscopy and Nanoscale Phenomena in Polar Materials*, IEEE, 2011, pp. 1–4.

[63] Erturk, A. and Inman, D. J., *Piezoelectric energy harvesting*, John Wiley & Sons, 2011.

[64] Koo, K.-Y., Park, S., Lee, J.-J., and Yun, C.-B., "Automated impedance-based structural health monitoring incorporating effective frequency shift for compensating temperature effects," *Journal of intelligent material systems and structures*, Vol. 20, No. 4, 2009, pp. 367–377.

[65] Hobeck, J., Owen, R., and Inman, D., "Residual thermal effects in macro fiber composite actuators exposed to persistent temperature cycling," *Applied Physics Letters*, Vol. 108, No. 11, 2016, pp. 111901.

[66] Black, J. T., Cobb, R. G., Swenson, E. D., and Cooper, B. J., "Rigidizable inflatable get-away-special experiment space flight data analysis," *Journal of Spacecraft and Rockets*, Vol. 48, No. 3, 2011, pp. 477–487.